KU LEUVEN

ARENBERG DOCTORAL SCHOOL
Faculty of Engineering Science

Multi-scale modeling of roping of Al alloys

Effect of meso-scale texture on surface roughening

Ling Qin

Supervisor:
Prof. Dr. Ir. Paul Van Houtte
Prof. Dr. -Ing. Marc Seefeldt, co-supervisor

Dissertation presented in partial
fulfillment of the requirements for the
degree of Doctor in Engineering
Science

June 2015

Multi-scale modeling of roping of Al alloys

Effect of meso-scale texture on surface roughening

Ling QIN

Examination committee:
Prof. Dr. Ir. Joos Vandewalle, chair
Prof. Dr. Ir. Paul Van Houtte, supervisor
Prof. Dr. -Ing. Marc Seefeldt, co-supervisor
Prof. Dr. Ir. Bert Verlinden
Prof. Dr. Ir. Jef Vleugels
Prof. Dr. Jin Won Seo
Prof. Dr. -Ing. Olaf Engler
(RWTH Aachen)
Prof. Dr. Ir. Leo Kestens
(Dept. MSE, UGent)

Dissertation presented in partial
fulfillment of the requirements for
the degree of Doctor
in Engineering Science

June 2015

Uitgegeven in eigen beheer, Ling Qin, Kasteelpark Arenberg 44 bus 2450, B-3001 Heverlee (Belgium)

ISBN XXX-XX-XXXX-XXX-X

D/XXXX/XXXX/XX

Preface

"Appreciation is a wonderful thing: It makes what is excellent in others belong to us as well."
Voltaire

I would like to express my deepest appreciation and gratitude to my supervisor Professor Dr. Ir. Paul Van Houtte, who has been both an inspiration and a tremendous mentor to me during this endeavour. I would like to thank him for encouraging me in my work and for helping me to grow as a research scientist. His advice on my research, as well as on my career, has been invaluable.

I would like to express my particular appreciation to my co-supervisor Professor Dr.-Ing. Marc Seefeldt, who has displayed the attitudes and the substance of a genius: he has continually and persuasively conveyed a spirit of adventure in regard to research and scholarship. Without his supervision and constant help this dissertation would not have been possible.

I would also like to thank Professor Dr. Ir. Joos Vandewalle for chairing my defense, Professor Dr. Ir. Bert Verlinden, Professor Dr. Ir. Jef Vleugels, Professor Dr. Ir. Jin Won Seo for serving as my jury members even at hardship. Special thanks go to my external jury members, Professor Dr. -Ing. Olaf Engler from RWTH Aachen University and Professor Dr. Ir. Leo Kestens from Universiteit Gent. I want to thank them all for helping my defense be an enjoyable moment, and for their brilliant comments and suggestions.

I would especially like to thank the technical staff of MTM: all of them have been there to support me over the years as I prepared samples and collected data for my Ph.D. thesis. Special thanks go to Tom Van der Donck for his assistance in EBSD measurements and to Louis Depré for his support in XRD texture and stress analyses. I am deeply grateful to Professor Christoph Genzel and Manuela Klaus from BESSY (HZB, Berlin, Germany) for their great help in synchrotron measurements. I am also grateful to O. Varela Pedreira and

Prof. I. De Wolf at IMEC for performing the Wyko surface measurements.

My gratitude goes to the financial support of the Interuniversity Attraction Poles Program (P7/21) from the Federal Government of Belgium and the M2i institute in the Netherlands. I also gratefully recognise the generosity of the aluminum production company Aleris for their provision of two AA6016 variants with different roping characteristics for my experimental study.

The Astro-group members are also much appreciated for their critical comments, valuable feedback and kind help. I am very grateful to Liang Zhu, Enze Chen, Martin Kriska, Stijn Kusters and Steven Dilien for their immense help in initiating my work and life in MTM. Xiebin Wang, Xiaodong Guo and Bolu Liu as my Chinese officemates and soccer teammates are also acknowleged for being supportive, unsophisticated and companionable. My special appreciation goes to Professor Albert Van Bael and Professor Rafael Schouwenaars for their valuable advice and discussions. My gratitude extends to Philip Eyckens, Koen Decroos and Jeroen Tacq for their professional and humorous scientific advice. My officemate Diarmuid Shore must be acknowledged for setting me on the road to Python. My sincere thanks also go to Qingge Xie, Yueqi Wang, Xing Gong, Anand Krishna Kanjarla and Gokula Krishna Muralidharan for their kind help.

All the friends within MTM are kindly acknowledged for their valuable advice and generous support. I thank Liugang Chen for helping me with the EPMA analysis. I also thank Bin Wu for his aid in the electrochemical analysis. Besides, I thank all other Chinese colleauges and friends in MTM: Jian Xu, Zhi Sun, Xiaolin Guo, Xuan Wang, Jing Zhang, Bin Zhou, Xue Wang, Pengcheng Yan, Xiaojun Yan, Li Zhang, Huayue Shi, Mianxian Wu, Fei Zhang, Gong Chen, Yuanyuan Guan, Ji Zou, Jingjing Liu, Hao Wu, Rui Zhong, Yujie Guo, Lichun Zheng, Jiemei Gu, Chen Li, Chunwei Liu, Zhuangzhuang Liu, Xuan Zhang, Huang Zhang, Luman Zhang and others for their enjoyable and thought provoking discussions and for sharing their inspirational stories.

Meanwhile, all the friends outside MTM are gratefully acknowledged for their thoughtful suggestion and kind help. I thank Yanxiang Huang at IMEC for his patient explanation on Fourier transformation. I also thank all the soccer teammates in Leuven for all the games played together. Moreover, I thank all other friends for all the fun and cheerful parties.

I would like to give the most special thanks to my Parents. Words cannot express how grateful I am for all the sacrifices that you have made on my behalf. Your prayer for me was what sustained me spiritually thus far. At the end I would like express appreciation to my beloved wife Lu Wang for her continued support, understanding and encouragement.

Abstract

Surface imperfections may develop as a result of the inherent inhomogeneity of plastic deformation over a range of different spatial scales in sheet forming processes. One type of such imperfections is called ‘roping’ or ‘ridging’, which has been observed in ferritic stainless steels, copper alloys and aluminum alloys. This strain heterogeneity is usually attributed to a certain clustering of grains with similar crystal orientations.

Surface investigations by means of electron backscatter diffraction (EBSD) made it possible to visualize the crystal orientations but have evidenced a gap between the length scale of the individual grains (smaller) and that of the roping or ridging pattern (larger). A new roping or ridging model is proposed to bridge this gap. It makes use of volume elements at an intermediate length scale (meso-scale) between the macro-scale and the grain scale. These volume elements are called ‘moving windows’ (MW). This model has been used to numerically analyze the roping propensity in an AA6016 aluminum metal sheet under uni-axial tensile testing. An EBSD measurement of the surface of the sheet material must be done first. Its data are directly incorporated into the meso-scale roping model. A mesoscopic window is then put on the surface (i.e. a MW which does not move yet). The Full Constraints Taylor model for polycrystal plasticity is then used to simulate a virtual tensile test on the material in this window. This makes it possible to calculate the thickness change of the polycrystal in the window. This procedure is repeated a number of times, each time shifting the position of the MW over a short distance along the tensile direction of the virtual tensile test. A ‘roping or ridging profile’ can then be estimated from these results (after an appropriate analysis). It was found that this analysis indeed produced a roping or ridging pattern with a larger wavelength than 2× the average grain size. According to our analysis, this means that the material is subdivided in mesoscopic polycrystalline volumes with contrasting textures. The wavelength which was found matched well with that of experimentally observed surface profiles.

The moving window method is also applied to a potential industrial application. In order to guide the upstream thermomechanical processing, a ‘contribution factor’ is proposed to assess the ‘sensitivity’ of the roping tendency to the strength of a particular texture component. For the material family at hand, the texture components CG-$\{021\}\langle 100\rangle$, Goss-$\{011\}\langle 100\rangle$, CH-$\{001\}\langle 120\rangle$ and Q-$\{013\}\langle 231\rangle$ were found to contribute most to the roping profile according to this method.

Beknopte samenvatting

De plastische vervorming tijdens een plaatvormgevingproces vertoont een inherente heterogeniteit en dit op meerdere lengteschalen. Ze kan aanleiding geven tot het ontstaan van diverse soorten onvolmaaktheden aan het oppervlak. Eén van deze soorten wordt in het Engels ‘roping or ridging’ (rimpelvorming) genoemd. Ze wordt zowel waargenomen bij ferrietisch roestvrij staal als bij koper- en aluminiumlegeringen. Het ontstaan van deze vervormingheterogeniteit wordt meestal toegeschreven aan een zekere clustering van korrels met gelijkaardige kristaloriëntaties.

Onderzoek met behulp van de ‘electron backscatter diffractie (EBSD)’ techniek liet toe de kristaloriëntaties aan het oppervlak zichtbaar te maken en heeft echter een hiaat aangetoond tussen de lengteschaal van de individuele korrels (kleiner) en die van de rimpelvorming (groter). Om dit hiaat te overbruggen wordt een nieuw model voorgesteld voor rimpelvorming. Het model maakt gebruikt van volume-elementen op een tussenliggende lengteschaal (meso-schaal) die ‘Bewegende Vensters’ (Moving Windows, MW) genoemd worden. Het werd gebruikt om de neiging tot rimpelvorming van metaalplaten vervaardigd uit een AA6016 legering te analyseren bij éénassige trekproeven. Eerst moet een EBSD-patroon van het plaatoppervlak opgemeten worden. Dan wordt op het oppervlak van de plaat een mesoscopisch venster gelegd (i.e. een voorlopig stilstaand MW). De kristaloriëntatie-gegevens van de korrels die door dat venster te zien zijn worden dan ingevoerd. Het FC-Taylor model voor de plastische vervorming van polykristalline materialen wordt dan gebruikt om virtuele trekproeven te simuleren op het materiaal het venster. Dit laat toe de dikteverandering van het ‘polykristal’ in het venster te berekenen. Dit wordt herhaald voor een reeks nieuwe berekeningen, waarin telkens de positie van het venster over een kleine afstand te verschuiven langs de trekas van de virtuele trekproeven. Het bleek dat deze dikteveranderingen (na een gepaste analyse) dan een rimpelprofiel opleverden met een golflengte die groter is dan 2x de korrelgrootte, wat niet evident is en volgens onze analyse betekent dat het materiaal opgedeeld is in mesoscopische polykrisallijne volumes met contrasterende texturen. De aldus

bekomen golflengte van het virtuele rimpelprofiel is inderdaad groter dan de korrelgrootte en blijkt na een uitgebreide studie vrij goed overeen te komen met de golflengte van het rimpelpatroon van het oppervlak van het plaatmateriaal.

De MW methode werd ook gebruikt voor een mogelijke toepassing in de industrie. Met het oog op de begeleiding van het stroomopwaarts thermomechanisch productieproces wordt een ‘contribution factor’ voorgesteld om de bijdrage van de volumefracties van bepaalde individuele textuurcomponenten tot de gevoeligheid voor rimpelvorming in te schatten. Voor de onderzochte materiaalfamilie bleken de textuurcomponenten CG-$\{021\}\langle 100\rangle$, Goss-$\{011\}\langle 100\rangle$, CH-$\{001\}\langle 120\rangle$ enQ-$\{013\}\langle 231\rangle$ volgens deze werkwijze bij te dragen tot de neiging tot rimpelvorming.

Glossary

cov covariance. 54, 87

D_0 reference strain rate. 21
δ difference between two plastic engineering strains in a specific direction. 88, 90, 91
$[D_{ij}]$ strain rate tensor. 21

e engineering strain component. 88
ϵ logarithmic strain component. 70, 99–102
η contribution factor. 84–86, 88, 90–93, 95, 96

f frequency. 54

g an orientation, or a texture component. 85, 87, 88, 90–93, 95, 96

h surface height. 86–88, 90–92
h_0 original window height. 51

λ wavelength. 6, 7, 13, 17, 26, 35–37, 39, 54, 81, 95, 97
l_{max} harmonic series expansion rank. 20, 103, 104

q contraction ratio. 21, 22, 71, 75

r strain ratio, or Lankford coefficient. 13, 14, 22–24, 28, 33, 35, 44, 45, 51, 54, 55, 59, 64, 68, 70, 71, 75, 77–79, 85, 88, 89, 92, 94, 96, 99, 101, 102, 104, 106–110, 113, 114, 117
R_a arithmetic mean roughness. 7, 17, 24, 26, 33, 36, 37, 39–43, 45, 53, 54, 57–59, 61, 63, 64, 66, 78, 79, 97
R_q root mean squared roughness. 7
ρ correlation coefficient. 54, 55, 59, 60, 65, 66, 68, 87, 88, 90, 91

S sample standard deviation. 54, 87, 88, 90–92
σ logarithmic stress component. 99–101

$\boldsymbol{\sigma}$ logarithmic stress. 21

t_0 original sample thickness. 51

v volume fraction. 85–88, 90–92

w window width. 42, 51

Acronyms

2D two dimensional. 5, 9, 11, 12, 23, 32, 57
3D three dimensional. 8, 11, 15, 96

AA3xxx 3xxx series of aluminum alloys. 6, 46
AA5xxx 5xxx series of aluminum alloys. 2
AA6xxx 6xxx series of aluminum alloys. 1–3, 5–12, 14, 15, 17, 25, 30, 44, 46, 52, 66, 92, 94, 96, 97
AACF areal auto correlation function. 7
ALAMEL advanced LAMEL. 78
APSD areal power spectral density. 7

CPFEM crystal plasticity finite element method. 5, 9, 11, 15, 26, 78, 97

EBSD electron backscatter diffraction. iii, 5, 8, 9, 11–13, 15, 17–24, 26–31, 33, 35, 36, 38, 39, 41–45, 47, 48, 50, 51, 53, 55, 56, 62, 65, 68, 71, 77, 84–88, 90–92, 94–96, 103–105, 111–114

FC Taylor full constraints (rate insensitive) Taylor polycrystal plasticity model. 22, 24, 25, 44, 45, 47, 51, 68, 72, 75–78, 85, 88, 94, 104, 113
FFT fast Fourier transform. 7, 54, 55, 66, 67, 69
FSS ferritic stainless steels. 2, 3, 5–7, 12, 46, 47, 97

IPF inverse pole figure. 19, 27, 33, 36, 38, 45, 48, 49, 56

M-RVE mesoscopic representative volume element. 22–24, 26, 39, 42, 44, 51, 53, 61–64, 68, 71, 72, 79–81, 96, 104
MAF moving average filter. 44
MTEX a MATLAB toolbox for quantitative texture analysis. 26, 90
MW moving window. 13–15, 17, 20–27, 33–37, 39, 41, 42, 44, 45, 47, 51–53, 55, 58–60, 62–71, 77–81, 84–87, 94–97, 103, 104, 111

ND the normal direction. 3–5, 11, 15, 19, 23, 24, 26, 32, 33, 42, 44, 48–53, 55–57, 59–61, 63–65, 68, 71, 74–76, 80, 81, 88, 91, 112–114, 117

ODF orientation distribution function. 19, 20, 29–31, 41, 50, 52, 57, 85, 96, 103–117
OIM orientation imaging microscopy. 19, 48
ORG overall roping grade. 7

PF pole figure. 20, 30
PSD power spectral density. 32, 33, 43
PSN particle stimulated nucleation. 29, 84, 89

RD the rolling direction. 2–7, 11, 15, 18–20, 23, 26, 32, 33, 43, 44, 46, 48, 50, 51, 57, 58, 65, 66, 68, 70, 71, 76–81, 85, 87, 89, 92, 99, 100, 102, 104, 114
RVE representative volume element. 24, 25, 45

SEM scanning electron microscope. 18, 48
SRM simple roping model. 11

T4 state a temper state: solution annealed and pre-aged at room temperature. 1, 8–10, 55, 90
T6 state a temper state: age hardened during paint bake cycle. 1, 8
TA tensile axis. 4–7, 21, 23, 46, 80, 81
TD the transverse direction. 3–7, 11, 14, 15, 17–21, 23–25, 28, 32, 33, 35, 37, 38, 43, 44, 46–48, 50–53, 56–58, 65, 68, 70–72, 74, 75, 77–81, 85–89, 92, 99, 100, 102, 104, 106–110, 112, 113, 117
TI texture index. 103, 104, 106, 112, 114, 117

UT uniaxial tensile/tension. 3–5, 17, 18, 21–24, 33, 43, 46, 47, 50, 51, 58, 68, 70–72, 75–77, 79–81, 85, 89, 92, 100–102, 104, 113

VPFFT visco-plastic fast Fourier transform. 5, 12, 15, 44, 47, 97
VPSC visco-plastic self-consistent. 5, 9, 11, 78

Wyko an optical profilometer based on a non-contact white-light interferometry system. 21, 50, 53, 55, 66

XRD X-ray diffraction. 8, 20, 30, 31

Contents

Chapter 1

General introduction

"The secret of getting ahead is getting started."
Mark Twain

1.1 Roping phenomenon and characteristics

Aluminum has attracted more and more attention in the automotive industry because of the growing demand of weight saving for more fuel-efficient vehicles [1–8]. For the autobody sheet application, 6xxx series of aluminum alloys (AA6xxx) become ideal candidates to replace heavier metals [4]. These Al-Mg-Si alloys of the AA6xxx series are heat-treatable, leading to an optimum combination of good formability in a temper state: solution annealed and pre-aged at room temperature (T4 state) and sufficient service strength in a temper state: age hardened during paint bake cycle (T6 state) [5]. Therefore, they are well suited for automotive body panel applications, where high dent resistance is required [9].

Besides the thermo-mechanical properties, another critical factor for the outer panel applications is the surface quality after final forming operations [4, 9]. During the forming processes, surface imperfections may develop as a result of the inherent inhomogeneity of plastic deformation over a range of different spatial scales. At the microscopic level, dislocation movements may cause surface defects such as crystallographic slip steps and non-crystallographic glide traces [10]. At the mesoscopic and macroscopic levels, the commonly observed surface roughening phenomena of polycrystalline metals are "orange peel" [10–

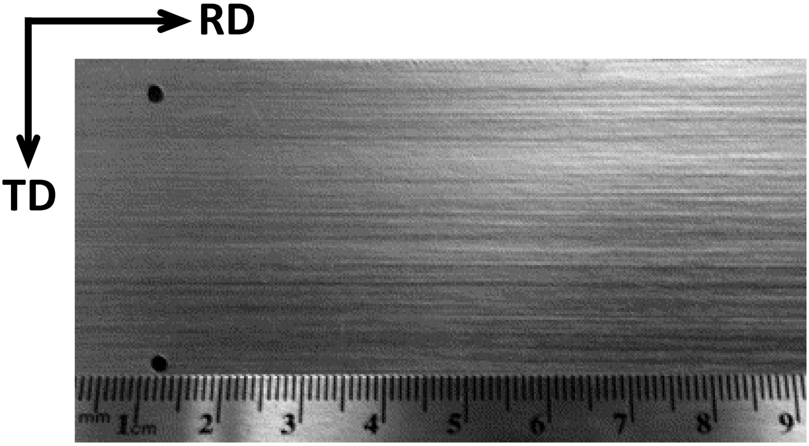

Fig. 1.1: Ridging topography of an AISI 430 FSS sheet under uniaxial tension in RD at 25% elongation. (Adapted from Ref. [24])

12], roping and Lüders lines [13, 14]. The latter usually occur in annealed 5xxx series of aluminum alloys (AA5xxx) under drawing or stretching operations, and cause loss in formability [5, 15–17]. Observed in AA6xxx alloys, the former two are often aesthetically objectionable and need to be removed by additional surface finishing procedures.

Roping, also known as ridging, has been observed in ferritic stainless steels (FSS) [18, 19], copper alloys [20, 21] and aluminum alloys [20, 22]. Scientific research to understand roping and methods of reducing ridging have been carried out over half a century. When FSS sheets are stretched in the rolling direction (RD), they often result in a series of ridges aligned in RD as shown in Fig. 1.1. In general, there are three types of roping or ridging. They are defined based on the topographical relationship of the upper and lower surfaces as shown in Fig. 1.2. It is reported that the FSS sheets generally develop a corrugated surface such that opposing sheet surfaces follow the same profile as shown in Fig. 1.2b. Ridges in FSS sheets can extend over the whole sheet length, and have a depth of $20 - 50\mu m$. The typical wavelength of ridging in FSS is much larger than the characteristic length-scale of the microstructure, being on the order of $1mm$ [23]. This surface imperfection reduces the cosmetic quality of the sheet and hinders its application for outer panel applications in the automotive industry.

The mechanism of ridging formation in FSS has been studied extensively [18, 19, 23, 24, 26–30]. The heterogeneous plastic response of FSS sheets upon

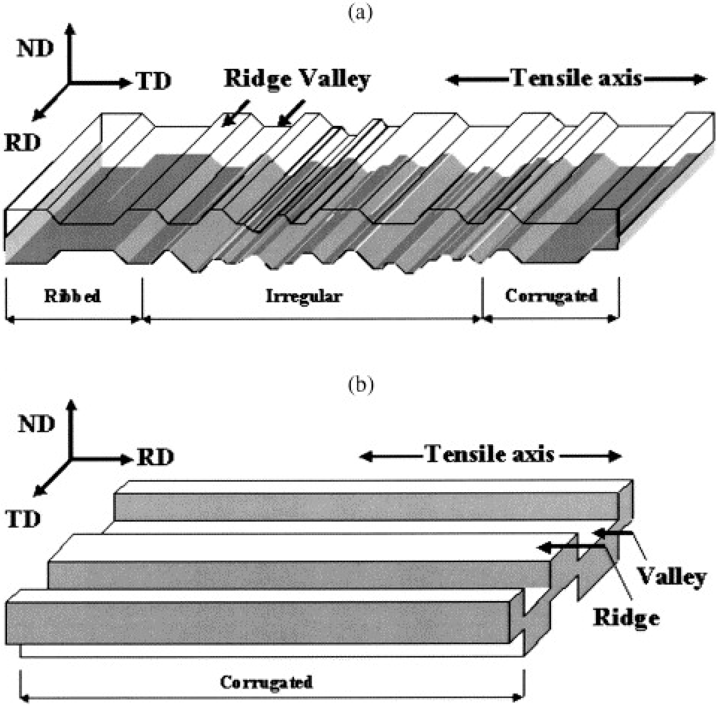

Fig. 1.2: Schematic representation of (a) roping topography observed in AA6xxx after tensile deformation in the transverse direction (TD) and (b) ridging observed in FSS after tensile deformation in RD. (Adapted from Ref. [25])

stretching in RD may be attributed to microstructural inhomogeneity, e.g. second phase segregation and/or crystallographic texture variation. An experimental investigation by Wilson *et al.* [22] precluded the association of roping with inclusion or impurity segregation using metallographic examination and electron micro-probe analysis. It is generally accepted that the occurrence of ridging is associated with clustering of grains having a similar tendency for deformation [18, 19, 23, 26, 27, 30, 31]. Among all the early proposals intended to explain this inhomogeneous deformation, Lefebvre *et al.* [23] demonstrated that the Takechi model [27] most closely resembles what is observed experimentally. In the original Takechi model, the through-thickness corrugation of the FSS sheet is attributed to the banded distribution of grains having crystallographic orientations whose slip systems are enantiomorphically (i.e. mirror symmetrically) oriented with respect to the plane containing RD and the normal direction (ND) as shown in Fig. 1.3. When uniaxial tensile/tension (UT) loading is imposed parallel to the length of the bands (the

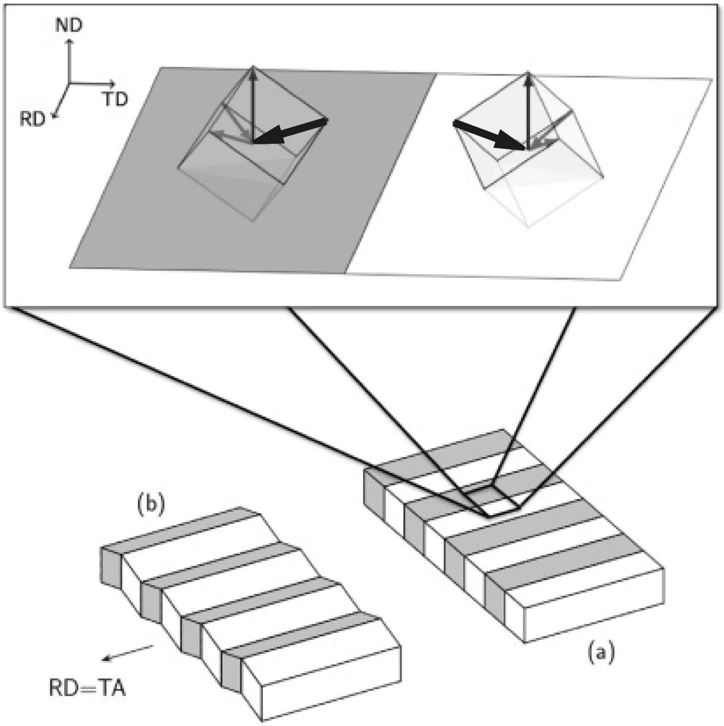

Fig. 1.3: The Takechi model for ridging envisions parallel bands of grains along the prior RD which is taken to be parallel to the tensile axis (TA). Alternating grains with different variants of the $\{111\}\langle 110\rangle$ orientation (gray and white) have enantiomorphically oriented slip directions (i.e. they are mirror images). During a UT performed parallel to RD the two variants tend to have a net out-of-plane shear in opposite directions resulting in a corrugation of the sheet (b). The inset schematically illustrates the orientations of the $\langle 111\rangle$ slip directions in two variants of $\{111\}\langle 110\rangle$ misoriented by 180° about ND. In this case the two gray slip directions cause elongation parallel to the TA but no contraction parallel to ND or TD. For contraction the thick black slip direction has to operate but this results in an unbalanced out-of-plane shear that leads to a rigid rotation in opposite directions for the grey and white grains. The result on a macroscopic scale is the bending or corrugation of the sheet as illustrated in (b). (Adapted from Ref. [23])

bands experimentally found to be parallel to the prior RD), a net out-of-plane shearing tendency occurs due to slip activity, causing a rigid rotation of the grains about the long axis of the bands.

Bearing in mind the importance of the spatial distribution of grains with certain crystallographic orientations, modeling work has been done to quantitatively link microtexture [32, 33] to roping using crystal plasticity simulations. Engler *et al.* [30] used the mean-field visco-plastic self-consistent (VPSC) code [34, 35] to identify grain clusters having a high tendency for through-thickness shearing from two dimensional (2D) EBSD data, collected from ND plane (i.e. the plane containing RD and TD) of an FSS sheet. While previous studies had been confined to identifying clustering of grains with similar orientations, the work of Engler *et al.* [30] was among the first to demonstrate large-scale clustering of grains with a strong out-of-plane shearing tendency lying in bands parallel to RD. Wu *et al.* [24] performed crystal plasticity finite element method (CPFEM) calculations on data similar to that used by Engler *et al.* [30] to predict the inhomogeneous distribution of shear tendency corresponding to the banded distribution of texture components along RD. Later, Sinclair [36] used the VPSC code with idealized microstructures to study the shearing behaviour of individual grains embedded within different media, implying the importance of the local environment to embedded grains. Following the work of Sinclair [36], Lefebvre *et al.* [23] used a full field visco-plastic fast Fourier transform (VPFFT) model to investigate the role of local environment of individual grains on the tendency for shearing by examining the information contained in the through-thickness RD plane (the plane containing ND and TD) of the sheet. Their full field approach successfully predicted both the amplitude and wavelength of one roping valley based on through thickness microtexture. The above simulations have greatly advanced our understanding of the phenomenon of ridging in FSS[1].

Recently, research focus has shifted to some AA6xxx alloys which are susceptible to roping. Specifically, roping is described as a series of ridges and valleys along RD, resulting in a wavy surface profile. Those ridges and valleys, also called paint brush lines, cannot be covered by subsequent painting [44, 45]. An image of a stoned surface appearance of an AA6xxx sheet subject to 15% plastic deformation is shown in Fig. 1.4. According to Refs. [9, 25], those ridges are approximately $5 - 50mm$ along RD, up to $30\mu m$ in depth and a few millimetres apart in TD. Experimentally, the roping intensity in AA6xxx sheets is accentuated by doing a UT test with the TA parallel to TD [9, 25, 44, 46–48]. Thus, the UT test along TD has become the standard method to reveal roping in aluminum alloys [49]. Instead of making standard tensile test samples [50–52], a common practice in Al industry is to prepare samples with a width of 50 to $75mm$ parallel to RD and to stretch them by typically 15% deformation in a conventional tensile tester when the TA is perpendicular to the former RD.

---

[1] Based on the progressive knowledge of ridging formation mechanism, methods have been developed to suppress ridging in FSS, including intermediate annealing between cold rolling passes [37–39], cross rolling [39, 39], introduction of phase transformation [40] and adjustment of other thermomechanical parameters [41–43].

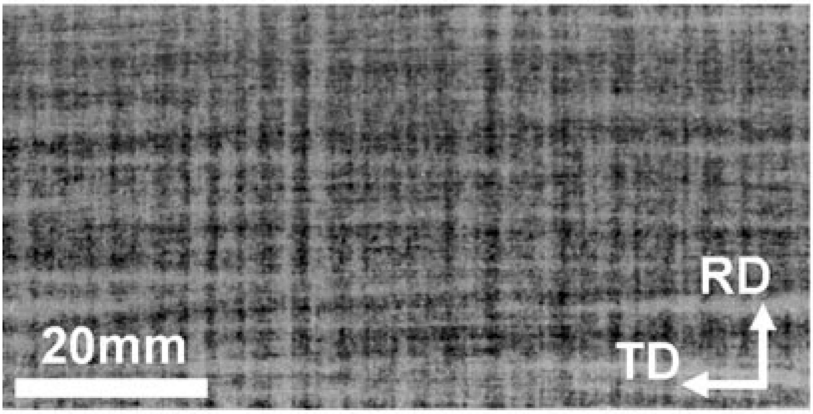

Fig. 1.4: Surface appearance given by the image of a stoned/ground surface after a 15% stretch along TD. This “stoning” technique is generally accomplished by careful manual grinding of the roughened surface with a P800 grade abrasive paper. Note that the visible lines along the TD are not relevant information, because they were artificially generated by the stoning technique. Note also that this technique tends to overstate the roping wavelength due to the fact that small peaks in-between two larger ones may not be affected by the grinding. (Adapted from Ref. [54])

A very recent experimental study carried out on sheet surfaces up to an area of $37 \times 28mm^2$ using a non-contact white light interferometer with a lateral resolution of $36\mu m$ and a vertical resolution of $20nm$ showed that the roping wavelength is between 1 to $12mm$ and the depth of the appearing minimal valleys up to $50\mu m$ [53]. This result has been considered to be the most reliable so far, because the measurement domain was large enough to be statistically relevant in the context of roping and the sample surface was not subject to any surface manipulation, e.g. inking or stoning.

It is experimentally observed by [25] that the upper and lower surfaces are not symmetrical and the distribution of ridges and valleys is irregular in AA6xxx alloys (see e.g. Fig. 1.2a). Besides this irregular type of roping, symmetrical shapes identified here as a ribbed type are very rare and are only reported by Writtridge and Knutsen [46] for a 3xxx series of aluminum alloys (AA3xxx) sheet. Unlike the ridging morphology in FSS, the corrugated type is not common and has not been reported for aluminum alloys to the knowledge of the author. Another major difference from ridging in FSS is that the intensity of roping in aluminum alloys is maximized when the TA is parallel to TD and is appreciably reduced for tensile specimens stretched along RD [9, 25, 44, 46–48]. These differences could be due to the fact that different mechanisms may operate in FSS and Aluminum alloys. Note that the effect of the TA on roping formation will be further discussed in Chapter 4.

The topographical characteristics of roping or ridging with banded feature parallel to the prior RD can be typified as high frequency roughness components superimposed on low frequency waviness components in TD, which gradually develop in the course of plastic deformation [53, 55]. Low frequency here refers to be waviness components having wavelengths comparable to the magnitude of the sheet thickness [56]. As Guillotin *et al.* [54] pointed out, the roping level given by a manufacturer's visual assessment after sheet forming and painting is binary (surface quality accepted or not) and quite subjective because it depends on a global human appreciation. To reduce human subjectivity, an image processing software Audi Roping Tool v.054 was developed to automatically evaluate the roping grade based on an inked and ground roping surface [57]. Standard statistical roughness parameters, such as arithmetic mean roughness, R_a, and root mean squared roughness, R_q [58], are commonly used to quantify the roped surface by many researchers [25, 46, 56, 59]. Then modified roughness parameters were introduced based on the separate distribution of peaks and valleys to tune the sensitivity to the contribution from different frequency components [56]. Because of the periodic characteristics in the roping morphology, frequency methods, such as areal auto correlation function (AACF) [54, 60], areal power spectral density (APSD) [61] and fast Fourier transform (FFT) [53, 55, 62], turned out to be very powerful and essential for roping characterization. Therefore, the two aspect, viz. amplitude (R_a or R_q) and wavelength (λ), should be considered together to fully characterize the roping morphology. Recently, the overall roping grade (ORG), expressed as the quotient of the unidirectional and the isotropic component, was proposed to quantitatively assess the roping level in an objective manner [53, 55, 61]. According to Schäfer *et al.* [53], this ORG in combination with the white-light interferometry surface measurement was able to make reliable, reproducible and objective roping evaluation.

Although ridging in FSS is a very interesting topic within the groups of crystallographic texture and crystal plasticity, this thesis will mainly focus on roping in AA6xxx due to the fact that no microtexture or surface topographical data corresponding to a FSS sample is available. Nevertheless, it is believed that ridging in FSS may be analyzed by an adapted moving window model as proposed in Chapters 2 and 3, if the data related to FSS ridging samples is available.

1.2 Microstructure and texture patterning

Roping in aluminum alloys is generally observed in T4 state sheets after the final forming process. The T4 state is a typical state delivered to the automotive manufactures, which generally exhibits good forming behavior. The final forming operations, such as stretching, stamping or drawing, can result in roping as an optical surface defect, which cannot be tolerated in outer skin applications [57, 63, 64]. It is believed that the microstructure in T4 state before the final forming process is responsible for roping. Therefore, the microstructure in AA6xxx T4 state sheets prior to the final forming process is generally studied to understand roping. However, roping may also appear in T6 state sheets after stretching because an artificial aging [65–67] during an paint baking cycle does not change the texture of T4 state sheets, which is believed to be related to roping.

The inhomogeneous feature of roping directly implies microstructural inhomogeneity. From a metallurgical point of view, microstructural inhomogeneity can be due to second phase segregation, i.e. segregation of precipitates or inclusions, or/and crystallographic texture variation. Early work by Wilson *et al.* [22] precluded the association of roping with inclusion or impurity segregation using metallographic examination and electron micro-probe analysis. To the knowledge of the present authors, no second phase segregation has been reported to be associated with roping in the commercial AA6xxx T4 state sheets so far, though particles to the scale of micrometer can be observed [63, 68, 69]. Therefore, the effect of the precipitates and inclusions on roping formation will not be considered in the regime of the crystal plasticity simulations. Herein, the roping formation is solely attributed to spatial texture variation and its associated plastic anisotropy [9, 10, 20, 22, 24, 25, 45, 46, 63, 70–74].

Experimental work on the roping phenomenon of aluminum alloys has shown that the roped surface is generally associated with texture inhomogeneity. Early work by Bate [71] using conventional X-ray diffraction (XRD) indicated that spatial texture variation would be a plausible cause for roping. Later, an alternating distribution of texture components was found once the EBSD technique [75–87] became available. Different research groups have reported band-like distribution of grains with cube orientation [44, 45, 88], as well as R [46], X [72], and alternating cube and Goss orientations [25, 54, 70, 89]. Fig. 1.5 shows such a banded distribution of cube grains. Attempts have been made to correlate the spatial distribution of grains, which belong to a specific texture component, with roping [44, 45, 48, 54]. Three dimensional (3D) serial sectioning microtexture measurements [76, 90–95] revealed that alternation of cube and Goss bands could persist through the thickness of the sheet samples [25, 54, 70]. Through a correlation study between the roped surface topography

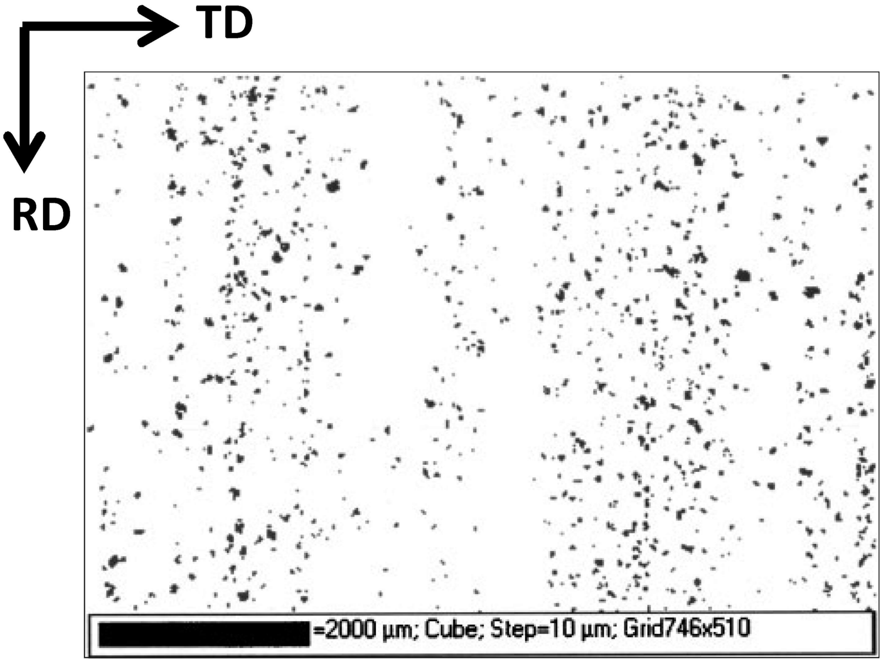

Fig. 1.5: Grains within 11° spread of the cube orientation of an AA6xxx T4 state sheet extracted from a large-scale experimental EBSD map, which is stitched by many small ones. (Adapted from Ref. [70])

and the strain maps, Guillotin *et al.* [54] stressed that the greater contribution to roping came from the subsurface grain layers just below the sheet surface. Jin *et al.* [70] reported that the spatial distribution of the through thickness averaged volume fractions of cube and Goss components from the sheet surface to 1/3 of thickness was similar to that in any 2D section, despite the fact that the spatial distribution of texture components changed in the thickness direction, with the peaks in the orientation profiles changing position with depth from the surface.

Crystal plasticity simulations including the CPFEM and the VPSC model have concluded that the occurrence of roping in Al alloy sheets is caused by the collective deformation of band-like clusters of grains with similar crystallographic orientation [9, 96]. Such a microstructure is a result of the thermo-mechanical treatments.

The typical steps (see Fig. 1.6) of thermo-mechanical processing of AA6xxx sheet

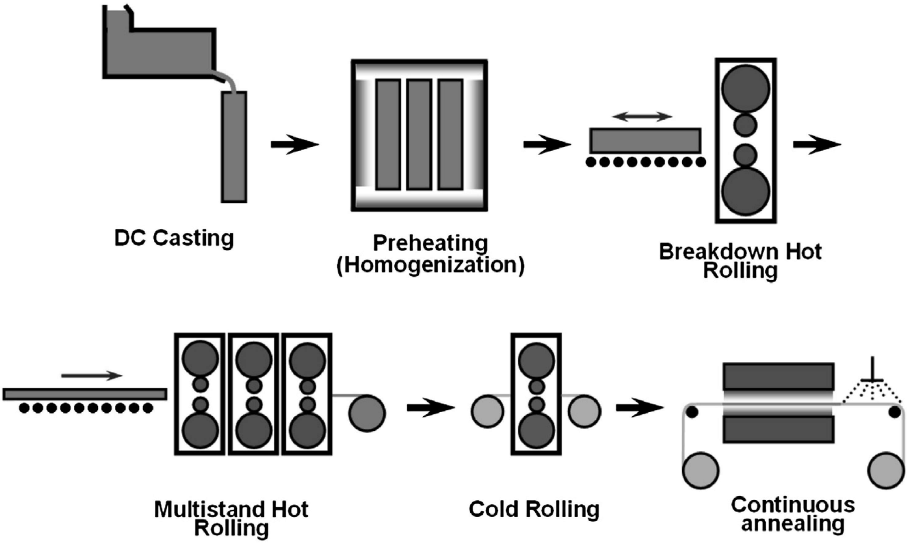

Fig. 1.6: Schematic illustration of the typical steps of thermomechanical processing of AA6xxx sheet alloys. (Adapted from Ref. [97])

alloys include casting, homogenization, hot rolling, cold rolling and annealing [5, 9, 63]. In both rolling processes, a highly elongated band structure is formed [63]. Especially, after cold rolling which is just before the T4 state, the sheets comprise a highly fibrous, deformed microstructure. Phenomenologically, the band-like microstructure in the T4 state could trace back to the striated/elongated grain structure at an earlier stage. These striated structures usually have their origin in coarse grains formed during hot rolling or intermediate annealing and drawn out into fibers during tempered rolling. These same fibers can produce roping in the annealed sheet if they recrystallize to a fine grain structure in which the grains originating from a given fiber have a few characteristic preferred orientations and tend to deform as a single fibrous grain. The term “ghost grain” is sometimes applied to structures containing such colonies of fine grains outlining portions of an earlier, larger grain structure[13]. Therefore, a band-like cluster of similarly oriented grains might originate from a single fibrous grain, i.e. a mother grain, at an earlier stage of the thermo-mechanical process. In other words, the microstructure of the T4 state inherits the spatial banding characteristics from the earlier processing stages [68, 71, 88] and therefore promotes roping [46]. This forms the foundation on which the mesoscopic approach to analyzing roping as proposed in this thesis is built. This approach tries to consider the local textures of the mesoscopic volumes of grain colonies instead of individual orientations.

Meanwhile, modeling work has been done to study the origin of the roping phenomenon. Basically, all the numerical studies on surface roughening consider the crystallographic anisotropy in terms of crystal plasticity, except the one of Romanova *et al.* [98]. Becker [74] pioneered the application of the CPFEM to the analysis of surface roughening. The simulations on 77 grains showed that strain localization could be responsible for the surface depression. Wu *et al.* [72, 73] directly incorporated large scale EBSD scans into a CPFEM to separately investigate the effects of elasticity, strain rate sensitivity, strain hardening, deformation path, EBSD step size, inhomogeneous deformation within individual grains, initial texture, texture evolution and spatial orientation distribution on surface roping. Their detailed parametric study indicated that the spatial distribution of orientations is the predominant factor for roping. Based on this observation, Wu *et al.* [49] developed the simple roping model (SRM), in which the interaction at each integration point is relaxed and the roping tendency is pre-computed for individual orientations, to quickly analyze the roping potential based on EBSD orientation maps. Engler *et al.* [9, 30] proposed another simple approach based on the VPSC model to account for the grain interactions to some extent. Subsequently, they readily adapted their model to the band approach to analyze the spatial distribution of the plastic strain of narrow bands of grains through the sheet thickness [9, 30].

Beaudoin *et al.* [96] presented the first 3D CPFEM model to analyze roping. They found that grains of similar orientations could deform collectively to form ridges or valleys. Later, Zhao *et al.* [47] did a direct 3D numerical analysis based on artificial 3D crystallographic microstructures. They confirmed the importance of spatial orientation distribution on the formation of surface roughening. Despite the fact that both 3D models provided valuable insight into grain interactions, they are impeded by the difficulty of generating a 3D texture distribution from the EBSD technique [72, 76, 92, 95]. Additionally, CPFEM simulations on a representative roping region demand substantial computation power [23, 96], which is not accessible for all laboratories.

Before roping topography can be simulated by an efficient full field CPFEM model based on a precise large-scale 3D texture distribution measured by an advanced 3D serial EBSD technique, it is practical to investigate the influence of the 2D through-thickness microtexture, which is measured at the TD/ND plane, on roping formation. Engler *et al.* [9] are among the first to publish a complete through-thickness EBSD orientation map for an AA6xxx sample suffering from roping as shown in Fig. 1.7. This experimental observation clearly confirmed that the banded distribution of specific orientations on the RD/TD plane (see e.g. Fig. 1.5) does not form continuous through-thickness bands [70]. Therefore, the texture patterning in AA6xxx sheets is of the 2D banding character (in RD/TD plane); no 3D banding can be identified based on the current texture

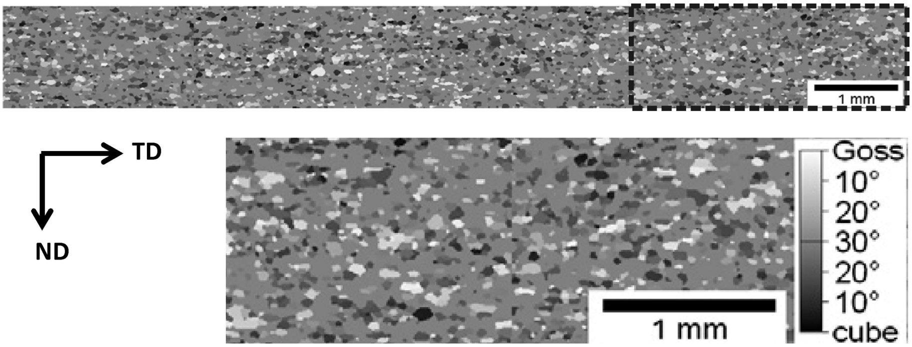

Fig. 1.7: A large-scale through-thickness EBSD orientation map of an AA6xxx sheet with pronounced roping. A rectangular region within the dashed border is enlarged to show the details. This EBSD map, stitched by 5 neighboring ones, is grey-shaded according to the angular deviation from Goss orientation (bright) and from cube orientation (dark). It is worth noting that care has been taken to retain the upper and lower sub-surfaces, which can be easily lost due to electro-polishing. The microtexture and its associated crystal plasticity analyses based on incomplete through-thickness EBSD maps without access to the microtexture close to the original surface planes may neglect the critical role of grains at the sub-surface and their interactions with underlining microstructure. (Adapted from Ref. [9])

analysis. Then, as Engler *et al.* [9] pointed out, the relevant question is how the local strain heterogeneities caused by the texture clusters of the 2D banding character can add up to significant height variations through the entire sheet thickness. The noncontinuous through-thickness banding character makes such a question unclear because a layer of surface grains cannot lead to considerable roping amplitude [99]. Therefore, an integral consideration of a number of subsurface grain layers is necessary.

The corrugated roping morphology in FSS basically implies that grains through the thickness deform collectively, which was revealed by a VPFFT model with focus on local grain interactions [23]. The collective plastic behavior of grains through the thickness was widely accepted for modeling roping in FSS. In contrast, roping in Al alloys was considered to be originating from inhomogeneous plastic deformation of grains at the surface and subsurface. Engler *et al.* [9] stressed the importance of the plastic contribution of grains located at subsurface layers. Guillotin *et al.* [54] did a correlation study and found that plastic strain variation of a layer at $50 \mu m$ below the surface correlated best with its roping profile. The present author found that a number of subsurface grain layers would contribute to the surface roping profile. All these studies indicate the importance of the influence of plastic behavior of grains underneath the ones at the outermost surface on the formation of the roping profile.

So far, most numeric studies have attempted to understand the macroscopic roping phenomenon based on the spatial distribution of grains with specific crystal orientations. According to a detailed mechanical analysis based on commonly observed ideal orientations in Al alloys, the texture components can be divided into two groups according to their r-value (see Fig. 1.8). The orientations, such as S, CH, R and Q, have an r-value lower than 1. In contrast, the r-value of Goss and CG is greater than 1. However, this approach cannot quantitatively predict the roping propensity. Through in-situ experiments and crystal plasticity finite element simulations, the deformation behavior of these individual grains is considered to be responsible for "orange peel" [10]. This is reasonable because the length scale of "orange peel" phenomenon, characterized by out-of-plane displacement fields (negative or positive) which roughly map the grain shape after plastic deformation, is the same as that of the grain size. Therefore, there is a big gap from the scale of individual grains to the macro-scale of roping. In other words, the width of the roping valleys and peaks is much larger than the grain size. These roping valleys and peaks are formed upon stretching indicating differential plastic thinning of banded clusters of grains with particular textures. It is the characteristic roping wavelength, in the length scale of several millimeters, that links to the length scale of spatially banded texture distribution instead of individual orientations in such bands. Therefore, this gap is believed to be closely linked to the length scale of the "ghost grains", which is mesoscopic. Unfortunately, this length scale becomes invisible because the mother grains subdivide and/or recrystallize into grain clusters during the thermo-mechanical processes. So, a mesoscopic roping model and, associated to that, the moving window (MW) method will be presented in this work to fill in the gap. Then, the model will be applied to both synthetic and experimentally measured EBSD maps on the sheet surface to predict the roping propensity.

In summary, the purpose of this thesis is to try to predict roping features, viz. wavelength and amplitude, based on spatial texture bands. The MW roping model will be used to simulate the mechanical responses of these texture bands based on a statistical plasticity code due to CPU time limitations. Due to the fact that the experimentally observed roping wavelength is much larger than the grain size but most likely related to the mesoscopic length scale of the hypothetical "ghost grains", this MW will try to capture the plastically contrasting local textures of these "ghost grains" in order to interpret roping from EBSD orientation maps. Specifically, the effect of global texture and texture banding on roping need to be studied using the MW model. Furthermore,

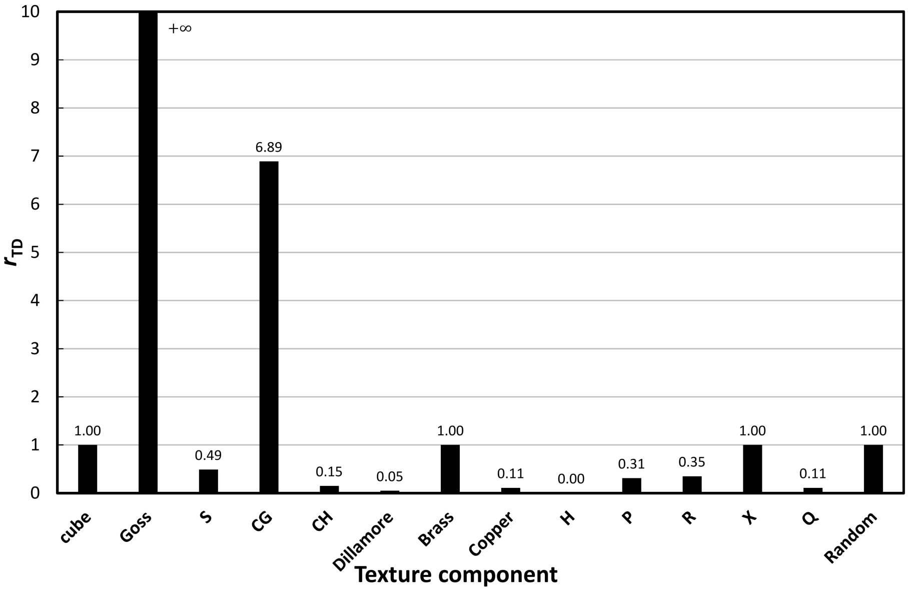

Fig. 1.8: r-value in TD simulated based on ideal orientations commonly observed in cold rolled and recrystallized AA6016 alloys. Detailed information on the r-value simulation is described in Section 5.2.1 and its numerical results are summarized in Table 5.1.

the MW model based on the through-thickness microtexture is used to try to find a minimal depth of material from the sheet surface that distinguishes the roping sample form the non-roping by simulating the collective behaviors of representative volumes of grains from both surface and subsurface.

1.3 Problem statement

In literature, the spatial gap between the grain scale of individual orientations and the macro-scale of roping has not been bridged. Based on microstructural evolution through the thermomechanical history, the invisible mesoscopic length scale of the "ghost grains" is believed to lie in between the scale of the individual grains and the macro-scale of roping. Therefore, it was decided to try to identify this invisible length scale in order to bridge up this gap. A method is proposed below to achieve that task (moving window method).

The automotive aluminum sheets of the AA6xxx series are known to suffer from roping. At present, 3D microtexture is hard to obtain and can be extremely difficult to be implemented into a CPFEM model [70, 72, 73, 92, 100, 101]. The full field VPFFT and CPFEM methods require substantial computation power, which is not accessible for many laboratories and industries. Due to practical reasons, a simple mechanical model accessible to most laboratories should be developed. Thus, a meso-scale crystal plasticity roping model based on the so-called MW method is proposed in Chapter 2 to numerically analyze the roping propensity in AA6xxx sheets. This meso-scale roping model uses EBSD data prior to the final forming operation to predict the roping propensity. The effect of texture banding and global texture in RD/TD plane on roping should be analyzed using surface EBSD maps. Then the influence of through-thickness microtexture on a surface profile should be analyzed based on EBSD orientation maps measured in the TD/ND plane. At last, the sensitivity of a specific texture component to roping should be analyzed to provide information for industry to fine-tune their upper-stream thermomechanical process parameters in order to reduce roping in a more cost-efficient way.

1.4 Thesis outline

This thesis consists of five chapters.

Chapter 1 covers a brief overview of the problem of roping or ridging. The current understanding of this problem is reviewed briefly. Then the research focus of this thesis is addressed.

Chapter 2 brings out the meso-scale moving window model and its application on surface profile simulation based on the EBSD data in the RD/TD surface plane.

Chapter 3 involves application of the meso-scale roping model to analyze through-thickness contribution to a roping profile based on the EBSD maps in the TD/ND plane.

Chapter 4 discusses the moving window simulation in other deformation modes.

Chapter 5 describes an industrial application of the moving window method to analyze roping contribution from a specific texture component.

Chapter 6 summarizes this thesis.

Chapter 2

Moving window simulation on surface texture distribution

> *"The true sign of intelligence is not knowledge but imagination."*
>
> Albert Einstein

This chapter is in part a reworked version of the paper:
Qin, L., Seefeldt, M., Van Houtte, P. (2015). Analysis of roping of aluminum sheet materials based on the meso-scale moving window approach. *Acta Materialia*, *84*, 215-228.

2.1 Introduction

The roping wavelength, λ, and amplitude in terms of R_a are sought by assuming that roping is caused by the existence of mesoscopic volumes with contrasting textures. The moving window method, on which a meso-scale roping model is based, is proposed to bridge the scale gap between the grain level of the individual orientations and the macro-level of the surface roping. Distinct from the methods of Lefebvre [23] and Wu [49], this MW method focuses on the collective mechanical response of a group of grains within a meso-scale volume lying in between the scale of the individual grains and the macro-scale of roping. The mesoscopic roping model is applied to numerically analyze the roping propensity in an AA6xxx sheet under UT testing in TD. The measured EBSD data of the sheet surface are directly incorporated into the meso-scale roping model, in which a Full Constraints Taylor polycrystal plasticity model is used to simulate the r-value and then the thickness change for the material in each window. The simulated surface profiles are compared quantitatively with experimental measurements. The effect of global texture and texture banding to roping is studied. The effect of the window size is discussed. A method to identify the banding wavelength is proposed.

2.2 Experimental

2.2.1 Alloys and sample preparation

The present chapter focuses on surface microtexture of two samples taken from commercial autobody aluminum alloy AA6016-T4 sheets subject to different heat treatment procedures. However, the detailed information on those thermomechanical procedures is confidential according to our industrial partner Aleris. These two samples are differentiated by their roping levels, and are designated roping and non-roping. The chemical composition of the two sheets is shown in Table 2.1. The roping sample is known to show severe roping after tensile plastic deformation in TD, while the non-roping sample gives little roping after stretching in TD. Both samples have been taken prior to the final forming process. The gauge thickness was $1.01mm$ and $1.16mm$ for the roping and non-roping sample, respectively.

Table 2.1: Nominal chemical composition (in wt.%) of alloy AA6016 for two automotive sheets (balance Al), both in T4. Note that the Panalytical PW2400 wavelength dispersive X-ray fluorescence spectrometer was used in the elemental analysis. The software used for semi-quantitative analysis is UniQuant 5.

	Si	Mg	Mn	Fe	Cu	Cr	Zn	Ti
roping	1.01	0.473	0.168	0.245	0.113	0.034	0.021	< 0.04
non-roping	1.05	0.399	0.032	0.212	0.191	0.029	< 0.01	< 0.03

For both EBSD measurements and UT tests prior to the surface measurements, all samples were mechanically polished down to $0.10\mu m$ colloidal silica followed by electro-polishing ($30V$, $-30°$C) for $60s$ using an electrolytic solution consisting of 70% ethanol, 10% 2-butoxyethanol, 8% perchloric acid and 12% distilled water. For all samples, approximately $60\mu m$ of surface material in thickness was removed by careful polishing.

2.2.2 EBSD measurement

Micro-texture measurements were conducted by means of automated EBSD using a Dual Beam FEI Nova 600 Nanolab scanning electron microscope (SEM). The EBSD maps in the sheet plane, i.e. the RD/TD plane, were measured to investigate spatial orientation distribution.

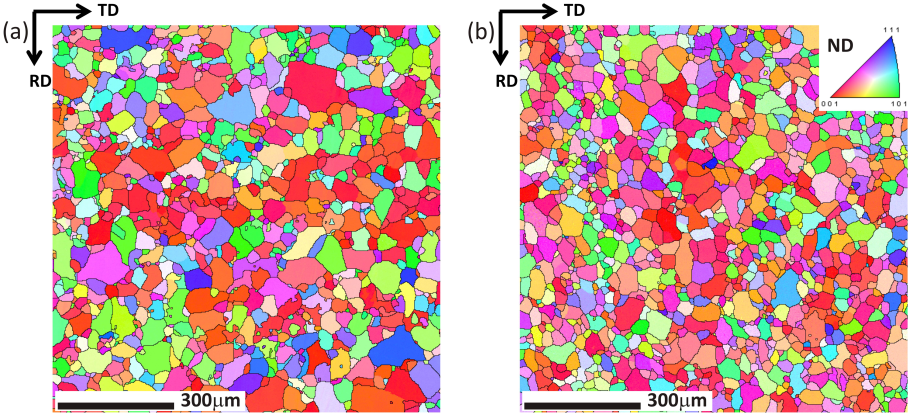

Fig. 2.1: inverse pole figure (IPF) maps of (a) roping and (b) non-roping samples with color coding according to their crystallographic direction along the sample's ND.

Grain size analysis was done on EBSD maps with scanning step size of $2\mu m$. Those maps include more than 5000 grains in order to be statistically significant. Fig. 2.1 shows a part of the IPF maps of both samples with grain boundaries higher than $5°$ indicated by black thin lines. The color coding scheme is defined according to the crystallographic direction along the sample's ND. Hereafter, all the IPF-EBSD maps adopt the same color coding, as illustrated by the standard triangle on the top right of the EBSD maps. The average grain size calculated by the TSL orientation imaging microscopy (OIM) software is approximately $27\mu m$ and $26\mu m$ for the roping and non-roping sample, respectively. They are quite similar and cannot be used to distinguish roping or not. The grain size distributions of both samples are shown in Fig. 2.2. It can be seen in Fig. 2.2 that the non-roping sample features a narrower grain size distribution than the roping sample. However, this grain size distribution difference between the two samples cannot explain their difference in roping propensity.

Large-scale EBSD maps with the size of $7.8mm$ in TD and $2.6mm$ in RD were obtained at a low magnification (80X) with a working distance of $15mm$. The scanning step size was $8\mu m$, resulting in 318176 indexed data points for each sample. Although the step size of $8\mu m$, being smaller than $\frac{1}{3}$ of the average grain size, is too large to provide the precise grain boundary morphology, it gives a statistically satisfactory orientation distribution and overall texture.

2.2.3 ODF

The orientation distribution functions (ODFs) were computed by the MTM-FHM software system [102] using the discrete EBSD orientation data [103]. Specifically, a

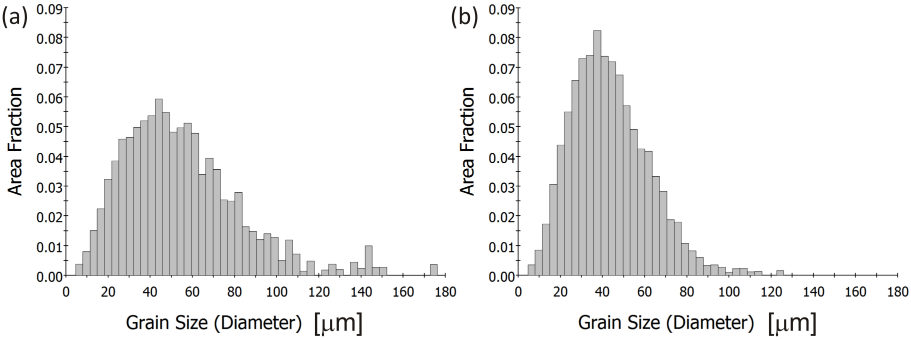

Fig. 2.2: Grain size distribution of (a) roping and (b) non-roping sample on the sheet plane, i.e. the RD/TD plane.

Gaussian distribution was applied around each orientation (in the convention proposed by Bunge [104]) of the EBSD data to produce an ODF and afterwards all these ODFs for the single orientations were added together to form a final ODF for the whole EBSD data. During the ODF calculation process, a Gaussian spread Φ_0 of 7° was used together with triclinic sample symmetry and a harmonic series expansion rank, l_{max}, up to 30. In addition, the texture indices of both samples were calculated according to Bunge[104] by the MTM-FHM software system.

Meanwhile, XRD in reflection mode was applied to measure the overall texture. A Siemens D500 texture goniometer was used with Copper X-ray radiation generated at $40kV$ and $40mA$. The ODFs were approximated by a harmonic series expansion up to $l_{max} = 30$ on the basis of cubic crystal symmetry and triclinic sample symmetry from {111}, {200}, {220} and {311} incomplete pole figures (PFs). The exponential ghost correction method proposed by Van Houtte [105] was used during the ODF calculation. The 4 PFs were measured on the same sample as EBSD measurement to check whether the EBSD scan is large enough to represent the overall texture with good statistics.

It is worth noting that the triclinic sample symmetry is used herein in order to show the complete ODF, since surface texture measured by either EBSD or XRD may not possess orthorhombic sample symmetry due to velocity and temperature gradient during rolling and annealing processes.

The quantitative texture analysis of typical texture components in AA6016-T4 aluminum alloys was conducted using a convolution method [104] based on the texture data. Firstly, the volume fraction of texture components of the overall texture was calculated. Then the local volume fraction variation of texture components was analyzed with the help of the MW method (see Section 2.3.2). In the first test case, the volume fraction distribution of R and cube by using window width of $500\mu m$ will be discussed (see Section 2.4.1).

2.2.4 Surface topography measurement

For a quantitative surface characterization, an optical profilometer based on a non-contact white-light interferometry system (Wyko)[1] was used in the VSI mode [106] with a low magnification (0.8X) objective lens. The vertical and lateral resolution is $3nm$ and $12.88\mu m$, respectively. For both materials, a plastic tensile strain of 0.15 was applied to dog-bone shaped UT samples whose TAs were aligned with TD. See Section 2.4.3 for detailed surface analyses.

2.3 Modeling strategy

In the present chapter, a simulation of the surface profile based on a surface EBSD map is presented. Specifically, the mechanical behavior under tensile testing in TD is simulated based on the mesoscopic representative local texture, which is selected by the MW method. The resulting simulated thickness change will be used to predict the surface profile for a certain uni-axial plastic deformation. The model uses $\{111\}\langle 110\rangle$ as potential slip systems.

2.3.1 Modelling a tensile test

In a UT test with x_1 being the tensile direction, all the macroscopic stress components are zero except σ_{11}, which is the tensile stress. So, the stress boundary conditions are:

$$\boldsymbol{\sigma} = [\sigma_{ij}] = \begin{bmatrix} \sigma_{11} & 0 & 0 \\ 0 & 0 & 0 \\ 0 & 0 & 0 \end{bmatrix}. \tag{2.1}$$

This is the stress at the meso-scale, i.e. the length scale of the MW (see Section 2.3.2). The mechanical properties of the materials at meso-scale are assumed to have a point group symmetry belonging to the orthorhombic symmetry family named "orthotropic symmetry" in the metal forming community. Their strain rate tensor is given by Eq. (2.2) implying plastic volume incompressibility:

$$[D_{ij}] = \begin{bmatrix} 1 & 0 & 0 \\ 0 & -q & 0 \\ 0 & 0 & -(1-q) \end{bmatrix} D_0. \tag{2.2}$$

In this, D_0 is a reference strain rate. q is the contraction ratio ranging from 0 to 1, as proposed by Bunge [107] and Hosford [108]. It is defined as minus the ratio of the plastic strain rate in the width direction to that in the tensile direction during

---

[1] Wyko is the name of the non-contact white light interferometer Wyko profilometer developed by the Veeco Metrology Group

a UT test. Empirically speaking, the shear components of the strain rate tensor in Eq. (2.2) are basically negligible for engineering materials for a tensile test, even if the assumption of orthorhombic sample symmetry is not valid [109].

The present thesis uses a full constraints (rate insensitive) Taylor polycrystal plasticity model (FC Taylor) to simulate the mechanical behavior of a texture in a tensile test. The FC Taylor model (see, e.g. Refs. [107, 109]) seeks the q-value (Eq. 2.2) iteratively by minimizing the plastic power dissipation per unit volume, i.e. the average Taylor factor. This energy minimization method proposed by Bunge [107] and Hosford [108] is physically equivalent to satisfying the stress boundary conditions in Eq. (2.1), which has been proved by Van Houtte in the appendix of Ref. [109].

Specifically, a series of 7 values ranging from 0 to 1 were assigned to q. The average Taylor factor was computed for each of them. Afterwards, the q-value corresponding to the minimal average Taylor factor was estimated by means of an interpolation method. Next, this q-value is used to compute the strain ratio:

$$r = \frac{q}{1-q}. \tag{2.3}$$

The r-value is the Lankford coefficient defined as the ratio of the plastic strain in the width direction to the concomitant plastic strain in the thickness direction during UT deformation. Thus, it is a parameter to characterize resistance to strain thinning under UT loading. The higher the r-value is, the higher the resistance to strain thinning is.

2.3.2 Moving Window Simulation

The MW method is proposed to automate the EBSD map analysis and surface profile simulations with regard to the mesoscopic representative volume element (M-RVE). The development of the MW method is based on the test box method in Ref. [110]. Comparable methods have already been described, including band approaches with narrow bands in Refs. [9, 30, 45], a scan box approach in Ref. [25], a static window approach in Ref. [46], a specimen window apparatus in Ref. [71] and a moving window approach attempting to quantify texture uniformity [111–113]. All these approaches have been designed to reveal the heterogeneous distribution of texture.

In the present chapter, the MW method is used to build up a simple meso-scale mechanical model based on the EBSD orientation data measured at the sheet surface. This MW tries to capture the plastically contrasting grain colonies, i.e. the hypothetical “ghost grains”, originating from the invisible mother grains at an earlier stage so that the influence of the thermomechanical history can be considered to some extent in order to predict roping propensity based on EBSD orientation maps. In other words, roping will be tentatively interpreted as a result of the existence of volumes with contrasting textures at a meso-scale. The simulation strategy of this model has been schematically illustrated in Fig. 2.3 (see also Refs. [110, 114]).

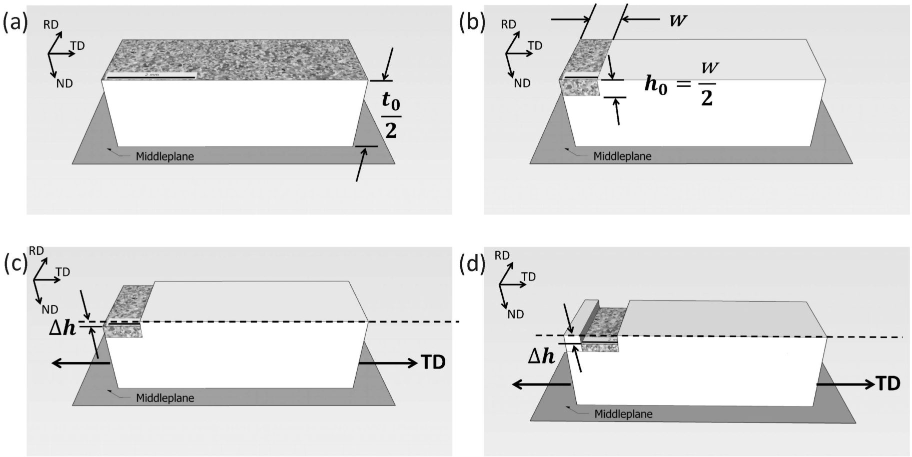

Fig. 2.3: Schematic illustration of the MW method in the RD/TD plane.

Firstly, a surface EBSD map is assumed to represent the crystal orientation distribution at the outermost surface.

Secondly, a M-RVE containing a band-like grain cluster is selected by a window on top of the EBSD map, where the window width is w and the length is set to be the dimension of the EBSD map along RD. w is a model parameter which will be given several values, as explained further. Furthermore, it is temporarily assumed that there is no texture gradient in ND in the M-RVE. This is not in contradiction with the observation that the spatial distribution of the through-thickness averaged volume fractions of cube and Goss components from the sheet surface to 1/3 of thickness was similar to that in any 2D section [70]. The initial thickness, h_0, of the M-RVE is set to be $w/2$ according to the analysis of the boundary conditions in section 2.3.3. It is worth noting that the minimal size of the M-RVE can be that of the "ghost grain" if known (see Section 1.2). However, this minimal size cannot be smaller than the step size used in the EBSD measurement. In the context of roping or ridging, the M-RVE containing a band of single grains could be too small, whereas one which would contain all grains could be too big.

Then, a UT test in TD would result in a thickness change of the M-RVE, Δh, which writes:

$$\Delta h = h_0 \left(e^{\left(-\frac{\epsilon_{\mathrm{TD}}}{1+r_{\mathrm{TD}}}\right)} - 1 \right), \tag{2.4}$$

where ϵ_{TD} is the imposed plastic strain in TD and r_{TD} is the simulated r-value from Eq. (2.3) when the TA is TD. In this chapter, ϵ_{TD} is set to 0.15.

Lastly, moving the window to a new position will include another grain cluster (whether coming from a different "ghost grain" or not). The step size of the MW can be as small as the step size of the EBSD map. The strain response of the new M-RVE can be simulated based on its texture information for a UT test in TD. So, Δh of the new M-RVE can be calculated by Eq. (2.4). If the window moves continuously scanning the entire EBSD map, the mechanical response of all the possible grain clusters can be analyzed by simulating the thickness change of all the corresponding M-RVEs. Consequently, the roping profile can be visualized by plotting the thickness change of grain clusters against their corresponding position.

To some extent, it is possible to use the simulated roping profile to understand how the local strain heterogeneities caused by the texture bands can add up to significant height variations through the entire sheet thickness, that is to say, to noticeable roping heights. Arithmetic mean roughness, R_a [115], is frequently used to characterize the surface roughness quantitatively. It is an amplitude parameter to characterize the surface based on the vertical deviation of the roughness profile from the mean line. Herein, it writes:

$$R_a = \frac{1}{N}\sum_{i=1}^{N} |\Delta h_i - \overline{\Delta h}|, \tag{2.5}$$

where Δh_i is the thickness change of a M-RVE, $\overline{\Delta h}$ the average thickness change of all M-RVEs and N the total number of the M-RVE.

2.3.3 Choice of the M-RVE dimension

In order to get an r-value [2] of a chosen representative volume element (RVE), i.e. the volume defined by a MW, the FC Taylor model computes the plastic strains in transverse and thickness direction by minimizing the total plastic work whereby a homogeneous distribution of the plastic strain rate is assumed. However, in reality, the sheet surface deforms differently from its interior. At a free surface, the strain compatibility requirement normal to the surface is relaxed compared to that of the core. At least, the surface grains tend to rotate and deform freely in ND, whereas the inner grains are more constrained by their surroundings. To be more specific, there is a layer of grains, where the stress components normal to the surface plane are zero at the free surface. This, therefore, can result in the heterogeneous distribution of the thickness strains after tensile deformation since neighboring grains may have different orientations.

Several researchers used single crystal plasticity models to calculate the strain distribution [9, 30, 49]. However, we, on the contrary, prefer to use a meso-scale volume of grains presumably belonging to a “ghost grain”, itself corresponding to a mother grain in an earlier stage of the processing (see Section 1.2). This mother grain is assumed to have been split up into several grains which together have a particular texture. The problem is that it is a priori unknown how large such mother grain has

---

[2] It is worth noting that the r-value is obtained by modeling a tensile test applied on a volume of polycrystals. This r-value is not an averaged value of those simulated on the basis of single crystals.

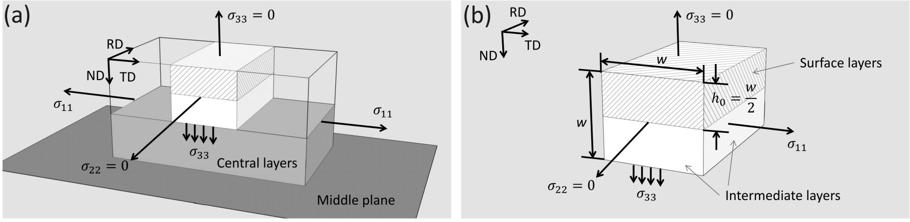

Fig. 2.4: Boundary conditions of the representative mesoscopic volume used in the MW method. The tensile test is done in TD. According to the boundary conditions, the sheet can be divided into (a) central layers as well as (b) intermediate and surface layers. A mesoscopic representative volume element (M-RVE) illustrated by the hatched volume is supposed to include a “ghost grain”.

been and that it is also unknown at which position it used to be. The MW method will try to find these things out.

Before the critical MW model parameters can be defined, the boundary conditions concerning surface and subsurface RVEs of grains are presented herein. Specifically, the sheet is partitioned into surface and central layers as shown in Fig. 2.4(a), where only one brick-shaped polyhedron of the surface layers is shown. The polyhedron is selected in such a way that it supposedly encloses a mesoscopic volume with characteristic texture which is different from that of its neighbors. So, this selected volume can have different plastic anisotropy resulting in a mechanical behavior different from the one of its neighbors. In contrast, the central layers are assumed to deform homogeneously and thus, taken together, behave as assumed by the FC Taylor model. Note that only half of the sample thickness is considered as shown in Fig. 2.4a. This is because the development of roping on the upper and lower surfaces in AA6xxx samples is identified to be irregular as defined in Ref. [25].

It is widely accepted that the stress boundary condition at the free surface is $\sigma_{33} = 0$, which means the outer surface of the mesoscopic volume is stress free during a tensile test as illustrated in Fig. 2.4(a). It is assumed that the strain boundary conditions at the free surface can be described by Eq. 2.2. However, the boundary of this volume with the central layers is not stress free. In other words, the response of the grains to the imposed macroscopic stress/strain rate leads to internal stresses, which depend on the variation in anisotropy among these grains.

It is speculated that there might be intermediate transition layers of grains with a somewhat intermediate plastic behavior, between the stress boundary condition dominated surface layers and strain boundary condition dominated central layers. In order to accommodate this effect, the mesoscopic volume is halved. As shown in Fig. 2.4b, the hatched volume with half height of the original polyhedron will be used to mimic the stress free grain layers, whereas the rest represents the intermediate transition layers. Hereafter, this hatched volume is taken to be the mesoscopic representative volume element M-RVE, which is assumed to behave as an ideal standard free-standing tensile test sample. The intermediate layers, of which the boundary conditions are unknown, are imagined to accommodate the stress/strain incompatibility between the M-RVE and the central layers. It is further assumed that the strain compatibility in ND and RD between neighboring M-RVEs and between these and the intermediate transition layers is relaxed in order to promote roping. In other words, it is assumed that the boundary conditions along the outer surface of the M-RVE prevail over these along the other surfaces. This assumption of the stress/strain behavior through the thickness of the material could be avoided by using a more complex model, such as a CPFEM (see, e.g. Ref. [74]).

MW simulation on artificial EBSD maps

Artificial EBSD orientation maps were generated to separately study the effect of combination of texture components and window width on the roping profile simulation. These artificial EBSD maps with alternating ideal texture component bands were made by invoking some functions of a MATLAB toolbox for quantitative texture analysis (MTEX) [116]. When discretizing the ideal orientation into Euler angles for EBSD ang-files, a de la Vallée Poussin function with a half width of 5° was used as kernel in MTEX. The ideal orientations considered are either those reported in literature as important roping contributors or experimentally observed in high volume fractions for the samples studied.

In order to investigate the influence of combination of texture components on roping profiles, artificial EBSD maps with equally spaced bands of two ideal orientations were generated. The width of the bands was $504\mu m$. The combinations of texture components, such as cube/random, X/random, R/cube and cube/Goss were selected due to their importance in inducing roping according to literature [25, 44–46, 54, 70, 72, 88, 89]. Additionally, CG/Q and Q/CH banding combinations were chosen because they were experimentally observed in high volume fractions according to Table 5.1. Then, the surface profiles were simulated by the MW model based on those artificial EBSD maps. A window width of $100\mu m$ was used in these simulations.

Various window widths were used to test the dependence of the predicted roping characteristics, such as the wavelength, λ, and amplitude, in terms of R_a, on the window width (selection) by using three different patterns of R/cube artificial EBSD maps. Pattern 1 consisted of R and cube bands with an equal band width of 504 μm. Then, different width ratios of the texture bands were considered to account for the effect of varying texture band widths on MW simulations. For pattern 2, the band width of R and cube was $256\mu m$ and $752\mu m$, respectively. In contrast, the band width of pattern 3 was $752\mu m$ and $256\mu m$ for R and cube, respectively. Moreover, the spatial coordinate of these three EBSD patterns was permutated randomly, respectively. This permutation operation therefore generated three corresponding R/cube patterns, i.e., randomized patterns 1, 2 and 3. MW simulations were also applied to these randomized patterns to explore the effect of the window width on the roping amplitude.

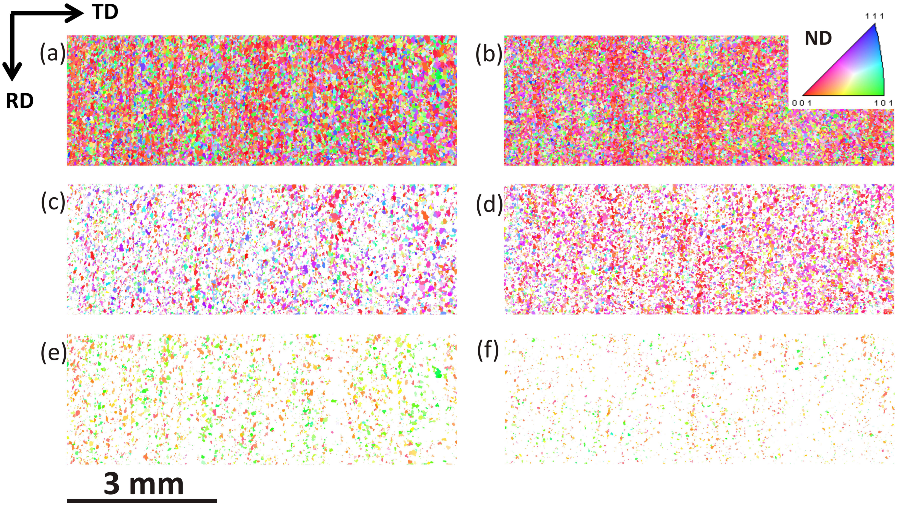

Fig. 2.5: Surface EBSD IPF maps (a) for the roping and (b) for the non-roping sample; IPF maps with only grains within 16.5° of exact S, CH, R and Q components (c) for the roping sample and (d) for the non-roping sample; IPF maps with only grains within 16.5° of exact Goss and CG components (e) for the roping sample and (f) for the non-roping sample.

MW simulation on experimental EBSD maps

MW simulations were also done on the experimental EBSD maps in order to validate the MW model. Those EBSD orientation data were incorporated into the MW model directly. Various window widths were used to simulate the surface profiles, on which the analysis of the length scales of texture band widths and their spacing was based. Additionally, the MW model was also applied to the EBSD map of the roping sample with its spatial orientation distribution being randomized but its orientation information being unchanged. Therefore, the global texture of the randomized roping EBSD map was the same as that of the roping sample, but the spatial coordinate was shuffled to remove any local texture variation. Similarly, the spatial coordinate randomization was also done on the EBSD orientation map of the non-roping sample.

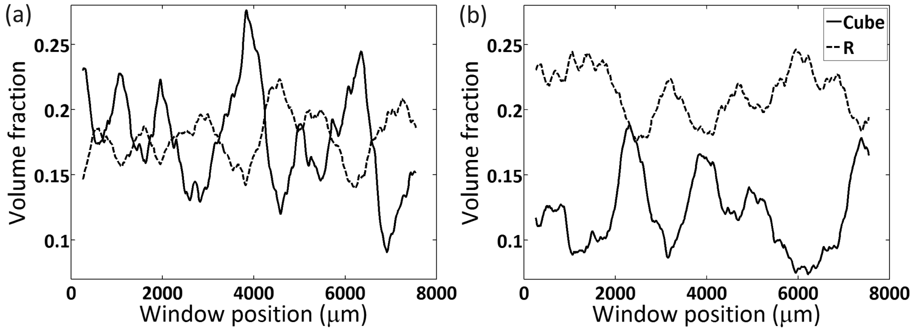

Fig. 2.6: Volume fraction variation of cube and R component along the TD (a) for the roping sample and (b) for the non-roping sample; window width = $504\mu m$, step size = $8\mu m$.

2.4 Results and discussions

2.4.1 EBSD analysis

The EBSD orientation maps are shown in Figure 2.5. It is common practice to extract the important texture components out of the EBSD orientation map to roughly identify the banding features. Here, the texture components can be divided into two groups according to their r_{TD}-value (see Fig. 1.8). The orientations, such as S, CH, R and Q, have an r-value lower than 1. In contrast, the r-value of Goss and CG is greater than 1. Thus, those two groups of orientations were separately extracted from the EBSD map as shown in Fig. 2.5. It can be seen clearly that the roping sample featured more Goss and CG components than the non-roping sample. Visually, a banded distribution of thinning resistant components, i.e. Goss and CG, seemed to appear in both samples. However, it is difficult to evaluate the roping tendency just based on this kind of subjective observation.

A more quantitative evaluation of roping tendency is to calculate the volume fraction distribution of the predominant texture components. Fig. 2.6 shows the volume fraction distribution of cube and R component in the EBSD maps along TD of both samples. Cube and R were selected because they were the most predominant texture components in both samples [3] (see Figs. 2.6, 2.7, 2.8 and 2.9). These orientations prevail during recrystallization of rolled Al alloys because of their favorable growth orientation relationship to certain deformation texture components after their nucleation at the so-called cube bands and grain boundaries [63, 118, 119]. It can be seen in Fig. 2.6 that fluctuations of the cube and R components existed in both samples. Furthermore, cube and R were mutually complementary in such a sense that peaks of cube volume

---

[3] According to Mao [117], cube and R are the main texture components after annealing of deformed commercially pure aluminums.

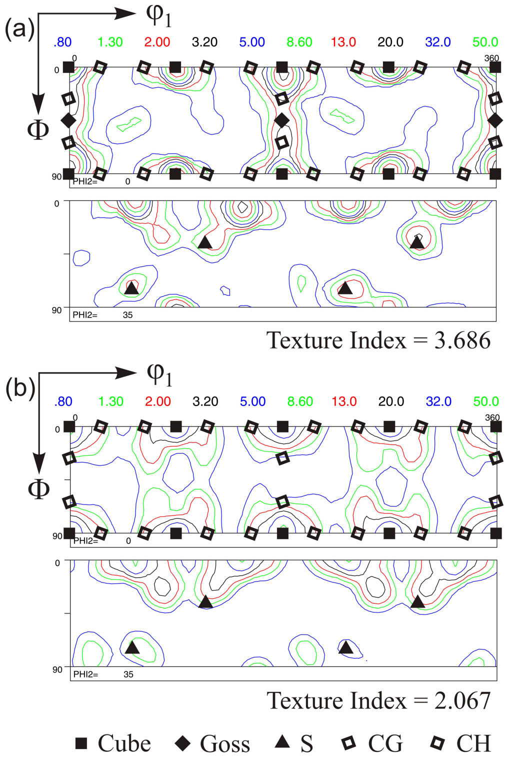

Fig. 2.7: ODFs of (a) roping and (b) non-roping samples calculated from discrete EBSD orientation data with typical texture components marked out.

fraction corresponded to valleys of R and vice versa. This implies that the formation of the cube orientation evolving from the cube bands competes with that of the R orientation nucleating at the former grain boundaries and the ‘random component’ due to particle stimulated nucleation (PSN). Although the roping sample showed a slightly higher volume fraction fluctuation of both texture components compared with the non-roping sample, Fig. 2.6 cannot distinguish the roping tendencies of the two samples. It seems that solely considering the spatial distribution of individual texture components cannot predict the roping tendency.

2.4.2 ODF analysis

The ODFs calculated from EBSD orientation data of both samples are shown in Fig. 2.7, where the most important texture components were identified on $\phi_2 = 0^\circ$ and $\phi_2 = 35^\circ$ sections. These calculated ODFs were found to be similar to those of

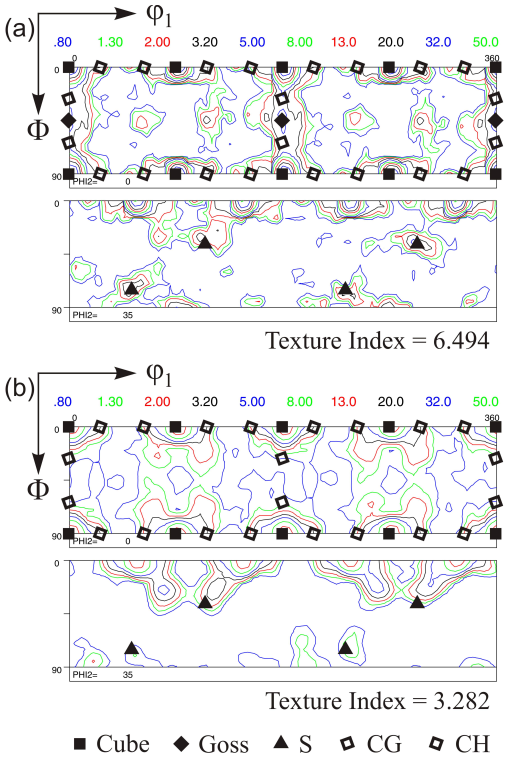

Fig. 2.8: ODFs of (a) roping and (b) non-roping samples measured by XRD with typical texture components marked out.

AA6xxx-T4 autobody sheets reported in Refs. [9, 25, 44, 63, 120]. The prominent texture components in the roping sample were cube, S, Goss, CG, and CH, whereas all the same components except Goss appeared in the non-roping sample. Then the volume fraction of common texture components shown in Fig. 2.9 (see also Table 5.1) confirmed that cube, S, CG and CH were the predominant texture components in both samples and the volume fraction of Goss in the roping sample was more than twice of that in the non-roping sample. Moreover, R and Q components were also found to be prominent in both samples from the volume fraction calculation in Fig. 2.9 (see also Table 5.1). Note that S and R components are very close to each other so that only the S component was marked in the ODF sections.

The $\phi_2 = 0°$ and $\phi_2 = 35°$ sections of the ODFs computed based on measured XRD PFs for both samples are shown in Fig. 2.8 with the major texture components marked out. The same major texture components could be identified for either sample by comparing the EBSD-ODF (Fig. 2.7) and XRD-ODF (Fig. 2.8). It is worth noting that similar textures have already been reported for AA6xxx-T4 sheets [25, 44, 63, 88, 120].

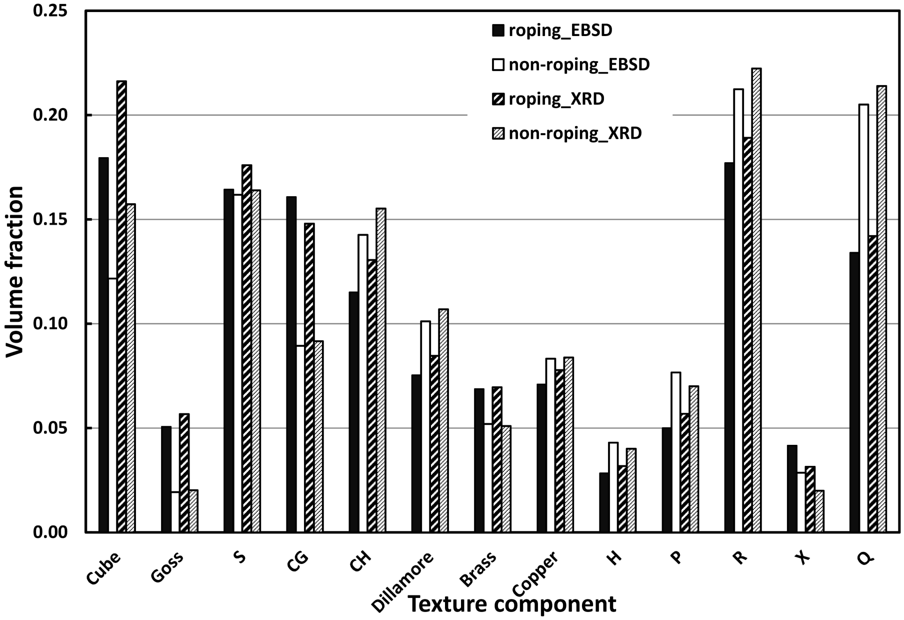

Fig. 2.9: Volume fraction of typical texture components calculated based on EBSD and XRD texture data.

The XRD-ODF featured higher texture index for either sample than the EBSD-ODF as shown in Fig. 2.7 and Fig. 2.8.

Fig. 2.9 shows the volume fraction of the typical texture components in both samples calculated from EBSD-ODF and XRD-ODF. For either sample, the volume fraction of each texture component from XRD-ODF was always higher than that from EBSD-ODF. This was in agreement with the observation that the texture index of XRD-ODF was higher than that of EBSD-ODF in either sample. However, the relative density of the texture components was approximately the same for either sample no matter which one of the two texture measurement techniques was used. Therefore, the higher texture indices of XRD-ODFs for both samples could be due to the fact that the mathematical implementation of ODF calculation is different for EBSD and XRD texture measurement [103, 121] (see subsection 2.2.3). In this case, the higher texture index for the sample did not necessarily mean that there was a stronger texture beneath the outermost surface grain layer. Instead, the same relative density of the texture components for either sample suggests that the scale of the EBSD scans was large enough to represent the overall texture.

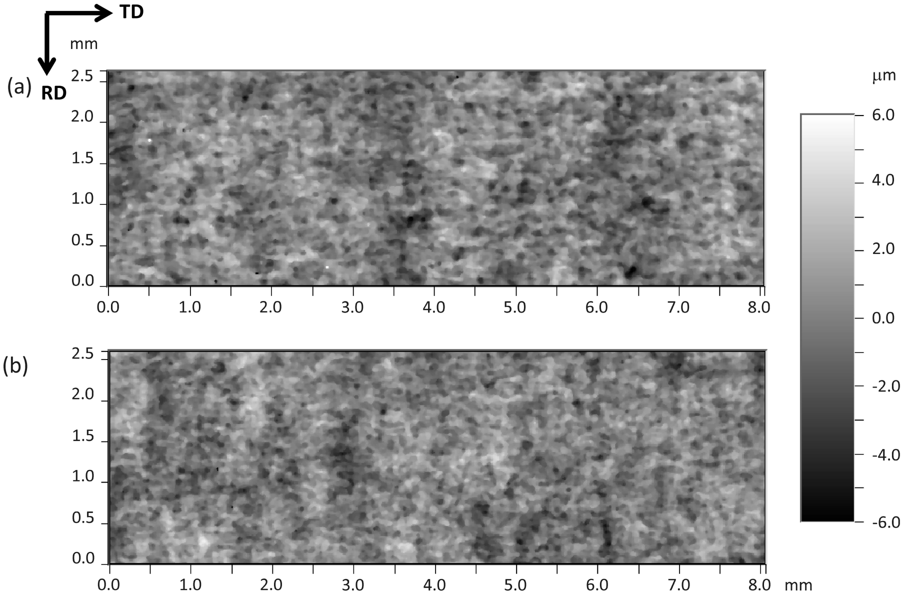

Fig. 2.10: 2D surface topography for (a) the roping sample and (b) the non-roping sample with the color code on the right referring to the surface height in ND.

2.4.3 Surface analysis

Fig. 2.10 shows the surface topography measured on the deformed tensile samples. There were peaks and valleys elongated along RD. Their overall length was larger for the roping sample than that for the non-roping sample.

In order to quantitatively assess the periodicity of the surface topography as shown in Fig. 2.10, the power spectral density (PSD) was computed. PSD, frequently used in the field of signal processing [122, 123], is based on the Fourier decomposition of the measured surface profile, i.e. the height as a function of the coordinate, into its component spatial frequencies. Mathematically, the PSD function is the square of the Fourier transform of the original height function [106, 122, 123]. For the 2D topography in Fig. 2.10, PSD of the height function was calculated for each horizontal (TD) and vertical (RD) line and then, averaged along RD and TD, respectively, as shown in Fig. 2.11. Herein, roping-TD represents the PSD of all TD-lines averaged along RD for the roping sample and so on. It can be seen in Fig. 2.11 that neither of the samples exhibited a predominant spatial frequency in RD, whereas the roping sample in TD showed a predominant frequency component of 0.61 mm^{-1} corresponding to a wavelength of 1.64 mm.

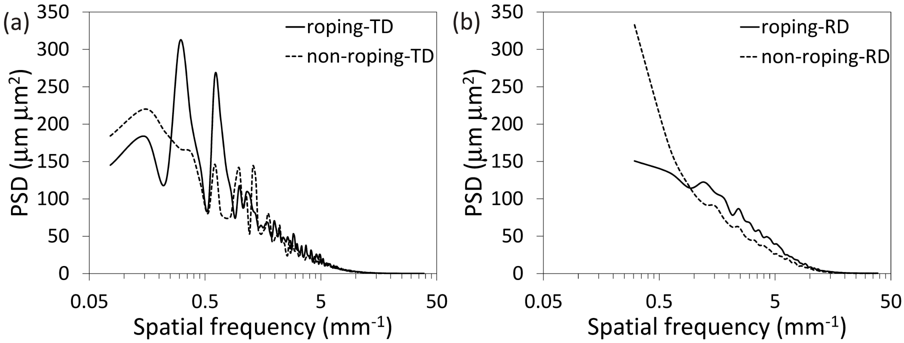

Fig. 2.11: Average power spectral density (PSD) against spatial frequency in (a) TD and (b) RD for both samples: (a) the PSD of all height profiles in TD is averaged along RD; (b) the PSD of all height profiles in RD is averaged along TD.

The TD-stylus-profiles of the surface topography in Fig. 2.10 were extracted line by line and then averaged along RD. Fig. 2.12a and c shows the resulting RD-averaged profiles, of which R_a was 0.53 and $0.35\mu m$ for the roping and non-roping sample, respectively.

2.4.4 Roping simulation using artificial EBSD maps

The roping profiles for a window width of $100\mu m$ were simulated for the artificial EBSD maps with equal texture bands of cube/random, X/random, R/cube, cube/Goss, CG/Q and Q/CH. cube or X texture bands embedded in the random textured matrix did not lead to surface undulation since their r-value in UT-TD was equal to 1 according to Fig. 1.8 (see also Table 5.1). However, all other alternate bands, such as R/cube, cube/Goss, CG/Q and Q/CH, resulted in obvious surface undulations due to the differences in r-value between the neighboring texture component bands. The hypothetical roping profiles for bands of cube/random and CG/Q are shown in Fig. 2.13 as an example. Therefore, texture component banding does not necessarily lead to roping. The difference in the r-value between neighboring bands is another requirement for the occurrence of roping.

The effect of the window width of the mesoscopic MW model on the surface profile simulation was discussed on the artificial EBSD maps with R/cube alternate bands. Three different patterns of R/cube EBSD maps were used. Window widths from $100\mu m$ to $3000\mu m$ were tested for all three patterns. Figs. 2.14, 2.15 and 2.16 show the effect of the window width on the roping profile simulation for the three patterns. The ND inverse pole figure color coding scheme for the IPF maps is shown on the top right corner in Figs. 2.14a and 2.16b. Note that the IPF maps and the simulated

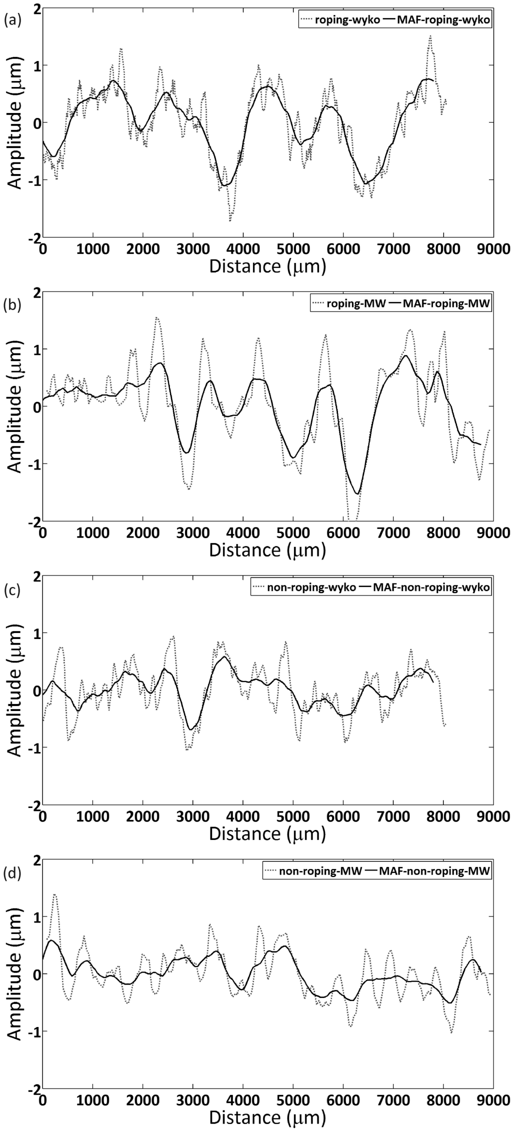

Fig. 2.12: Comparison of the surface profiles from (a, c) experiment (Wyko) and (b, d) simulation (MW), showing good quantitative agreement for both the wavelength and the amplitude for (a, b) the roping and (c, d) the non-roping sample. A moving average filter (MAF) is applied to the raw profiles to reveal the long-range waviness by suppressing the short-range roughness (see Section 2.4.5). More information on (b, d) will be given in Section 2.4.5.

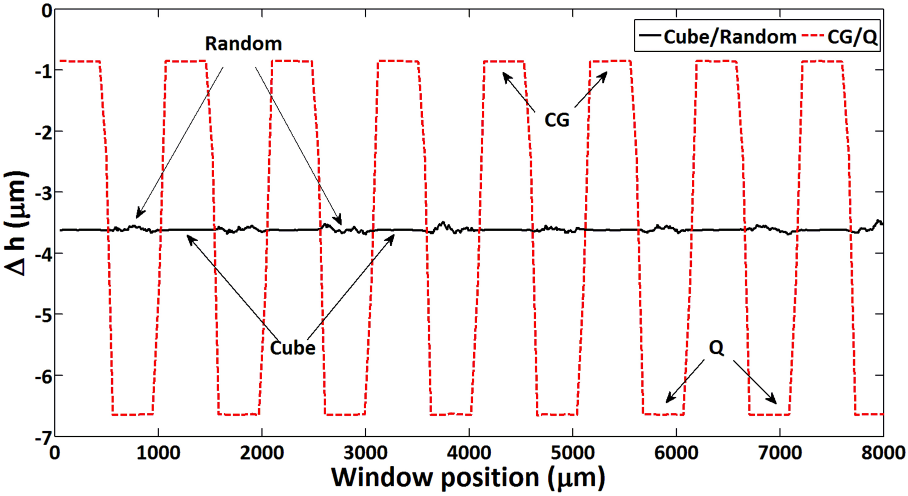

Fig. 2.13: Hypothetical surface profiles for the artificial EBSD maps with ideal texture component bands of cube/random and CG/Q simulated by the MW model using window width of $100\mu m$.

surface profile figures are aligned along TD to assist direct comparison in Figs. 2.14 and 2.16.

Fig. 2.14 shows the effect of the window width on the simulated surface profile for pattern 1. It can be seen that the MW simulation can identify the spatial orientation distribution pattern by using a wide range of window widths. Since the period of a pair of R and cube bands along TD was $1008\mu m$, this value would be the wavelength of the roping profile upon deformation. When the window width was smaller than the wavelength of the roping profile, for instance, from $100\mu m$ to $900\mu m$, the MW simulation predicted that R bands corresponded to the valleys whereas the cube bands to the peaks as shown in Fig. 2.14b. This type of simulated profile is called herein the positive tendency profile due to the fact that R and cube bands should form valleys and peaks, respectively, because the r-value in TD of R component is lower than that of cube (see Fig. 1.8). However, if the window width became larger than the wavelength but smaller than twice of that, the simulated profiles were flipped over with respect to a horizontal line. Here, it is called negative tendency, such as the simulated surface profile using the window width from $1100\mu m$ to $1900\mu m$ (see, e.g., Fig. 2.14b). Further increasing the window width by a magnitude of the wavelength would flip over the simulated profiles again along a horizontal line to the positive tendency, such as the profile based on the window width of $2100\mu m$. Therefore, the positive and negative tendency profile will repeatedly alternate with increasing window width by the multiple of the wavelength. Then, the effect of window width on roping profile morphology can be summarized as:

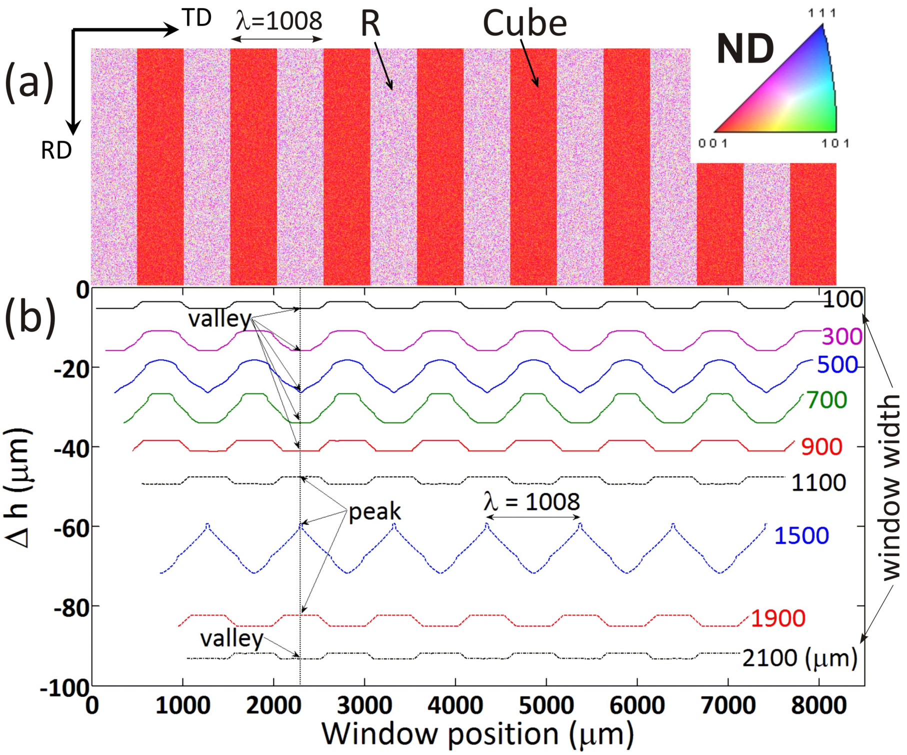

Fig. 2.14: Effect of the window width on the simulated surface profiles for pattern 1: (a) the artificial R/cube banded EBSD IPF map of pattern 1; (b) the simulated surface profiles by using different window widths, w, which are indicated at the right of the profiles.

$$\begin{aligned} &\text{positive tendency,} && \text{if } 2n < \tfrac{w}{\lambda} < 2n+1; \\ &\text{negative tendency,} && \text{if } 2n+1 < \tfrac{w}{\lambda} < 2n+2; \\ & && n = 0, 1, 2\cdots, \end{aligned} \tag{2.6}$$

where w is the window width and λ the wavelength.

No matter which window width was used, the wavelength could be identified as shown in Fig. 2.14b. Therefore, the mesoscopic MW model is insensitive to the choice of the window width for the purpose of identifying the roping wavelength. The amplitude changed with the choice of the window width due to the coordination of window width and volume height as shown in Fig. 2.4b and Fig. 2.3b. When the window width satisfies Eq. 2.7, the amplitude approximately reaches the maximum, as illustrated in Fig. 2.15. This can also be readily seen in the arithmetic mean roughness analysis (see, e.g. Fig. 2.17).

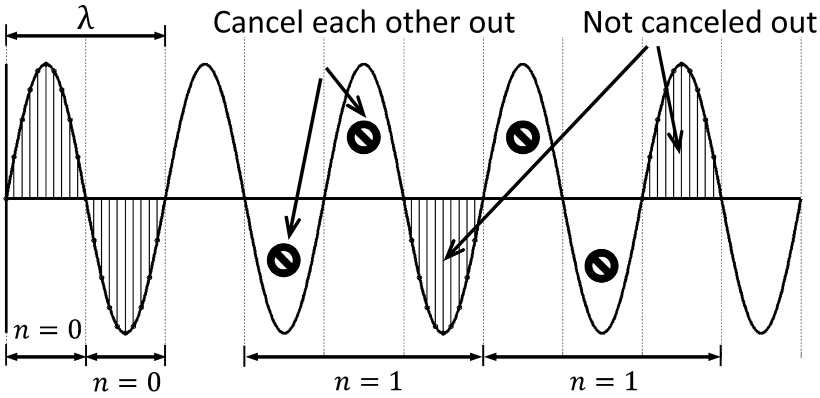

Fig. 2.15: Schematic illustration of the window width selection corresponding to the maximal roping amplitude by assuming an ideal sinusoidal roping profile. The horizontal and the vertical axis is spatial distance in TD and amplitude, respectively. When the window width w is $\left(\frac{1}{2}\right)\lambda$, an entire roping peak or valley can be selected to give a maximal integrated amplitude. If $w = \left(1 + \frac{1}{2}\right)\lambda$, a maximal integrated amplitude can still be obtained after a peak cancels a valley out. This is an illustrative proof of Eq. 2.7.

$$\begin{array}{l} w = \left(n + \frac{1}{2}\right)\lambda \\ n = 0, 1, 2\cdots \end{array} . \tag{2.7}$$

Moreover, the effect of window width on the simulated roping profiles was also investigated for pattern 2 and pattern 3 as shown in Fig. 2.16. For pattern 2 and 3, the band width of R and cube was not equal. The width of the narrow and wide bands was 256 μm and 752 μm, respectively. This made the wavelength of roping, λ the same as that of pattern 1. It can be seen in Fig. 2.16 that the simulated surface profile evolved with increasing window width. When the window width did not exceed the narrow band width, for instance, $100\mu m$ and $250\mu m$, the simulated surface profiles could explicitly reflect the R and cube bands distribution as shown in Fig. 2.16. If the window width was between $\frac{\lambda}{2}$ and λ, with λ representing the banding wavelength, the simulated profiles could not indicate the width of the R and cube bands (compare Fig. 2.16a and c with b and d, respectively). However, they could still trace the locations of the bands by keeping the positions of valleys and peaks unchanged compared with the profile of window width of $100\mu m$. This implies that the simulated profiles can always give a satisfactory prediction on the banding wavelength, regardless of the window width. Therefore, the mesoscopic MW model is insensitive to the choice of the window width for the purpose of identifying the predominant roping wavelength.

Fig. 2.17a shows the effect of the window width on the simulated arithmetic mean

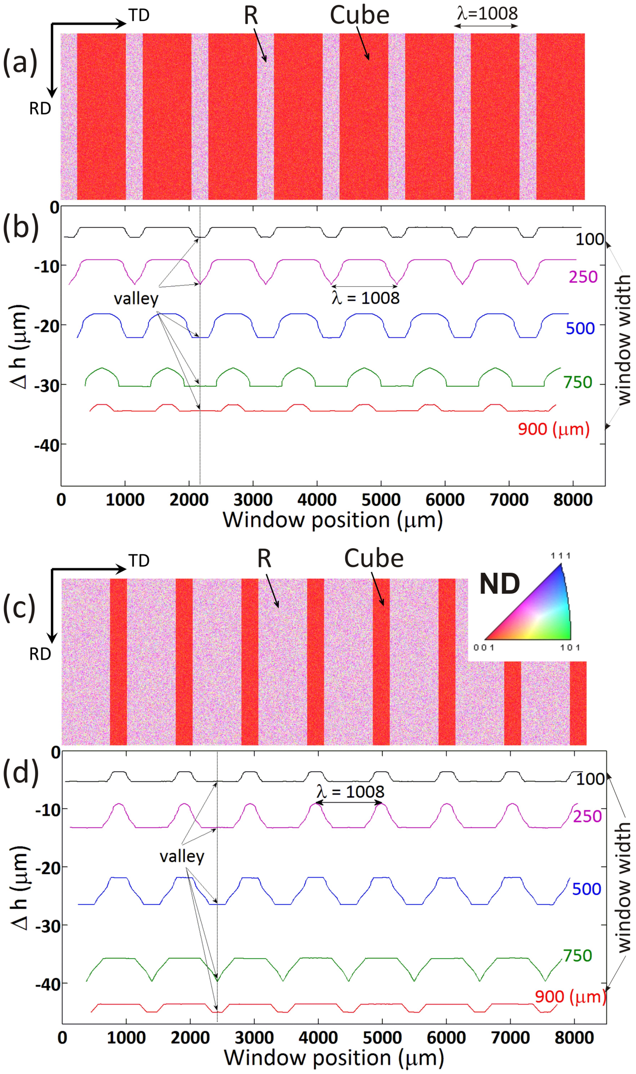

Fig. 2.16: Effect of the window width on the hypothetical surface profiles simulated based on the artificial R/cube EBSD maps with unequal bands: IPF map of (a) pattern 2 and (c) pattern 3, hypothetical surface profiles for (b) pattern 2 and (d) pattern 3 simulated by using different window widths. Note that the IPF maps and the hypothetical surface profile figures are aligned along TD to facilitate direct comparison.

roughness, R_a, for the synthetic R/cube patterns. It is worth noting that the wavelength of R/cube bands distribution is the same, namely $\lambda = 1008\mu m$, for all three banded patterns. It can be seen in Fig. 2.17a that, pattern 1 with equally large bands showed the highest roughness at all the window widths compared to other patterns. It can also be seen that the maxima of R_a for all three banded patterns corresponded to the window width of about 0.5, 1.5 times and 2.5 times of λ, which defined the mesoscopic volumes leading to the greatest fluctuation of Δh. In contrast, the minimal R_a values corresponded to the window widths of multiples of λ. Such window widths always included the same portion of each texture components in the ideally periodic EBSD patterns 1, 2 and 3. This therefore made the simulated roping profile exhibit the lowest thickness fluctuation. Consequently, the window widths corresponding to the minima of R_a, e.g., 1000 and $2050\mu m$, reveal the wavelength of the R/cube bands distribution. The influence of the window width on R_a for the randomized R/cube patterns (Section 2.3.3) was also investigated. Comparing Fig. 2.17a with b, it can be seen that R_a curves of the randomized patterns were always lower than those of the banded patterns. This observation therefore excludes the contribution of the global texture to roping and provide conclusive evidence that the minima of R_a can be used to identify the banding wavelength.

2.4.5 Roping simulation using experimental EBSD maps

To test the predictive capacity of the MW mesoscopic model, the roping simulations were done on both experimental EBSD orientation maps shown in Fig. 2.5. The simulated surface profiles on these EBSD maps are shown in Fig. 2.18. In the MW simulation, the window width used ranged from $32\mu m$ to $1000\mu m$, as indicated in the legend in Fig. 2.18. The width of $32\mu m$ was considered to be the lower limit of the width of grain clusters since the averaged grain sizes were $27\mu m$ and $26\mu m$ for the roping and non-roping sample, respectively. On the other hand, the initial thickness of the M-RVE described in section 2.3.3 should not exceed half of the sheet thickness and was defined to be half of the window width. Thus, it was reasonable to set the upper limit, i.e. the physical constraint, of the window width to be $1000\mu m$, because the gauge sheet thickness of the roping sample was $1.01mm$.

As can be seen in Fig. 2.18, the simulated surface profiles evolved with increasing window width for both samples. When the window width was $32\mu m$, which was the width of a single grain band, the simulated surface profiles in Fig. 2.18c-d fluctuated significantly with predominant high frequency components in the order of the grain size, i.e. at the same level of “orange peel”. Increasing the window width till $96\mu m$ smoothed out a portion of the grain-sized fluctuation. Further increasing the window width screened out most of the high frequency components, but kept the low frequency components as shown in Fig. 2.18a-b and e-f. Therefore, increasing the window width to some extent can serve as a high frequency filter, which is equivalent to filtering out the high frequency components in Fourier transformation [62].

Distinct differences of the simulated surface profiles could be found between the roping and non-roping sample. It can be seen in Fig. 2.18c and d that the surface profiles

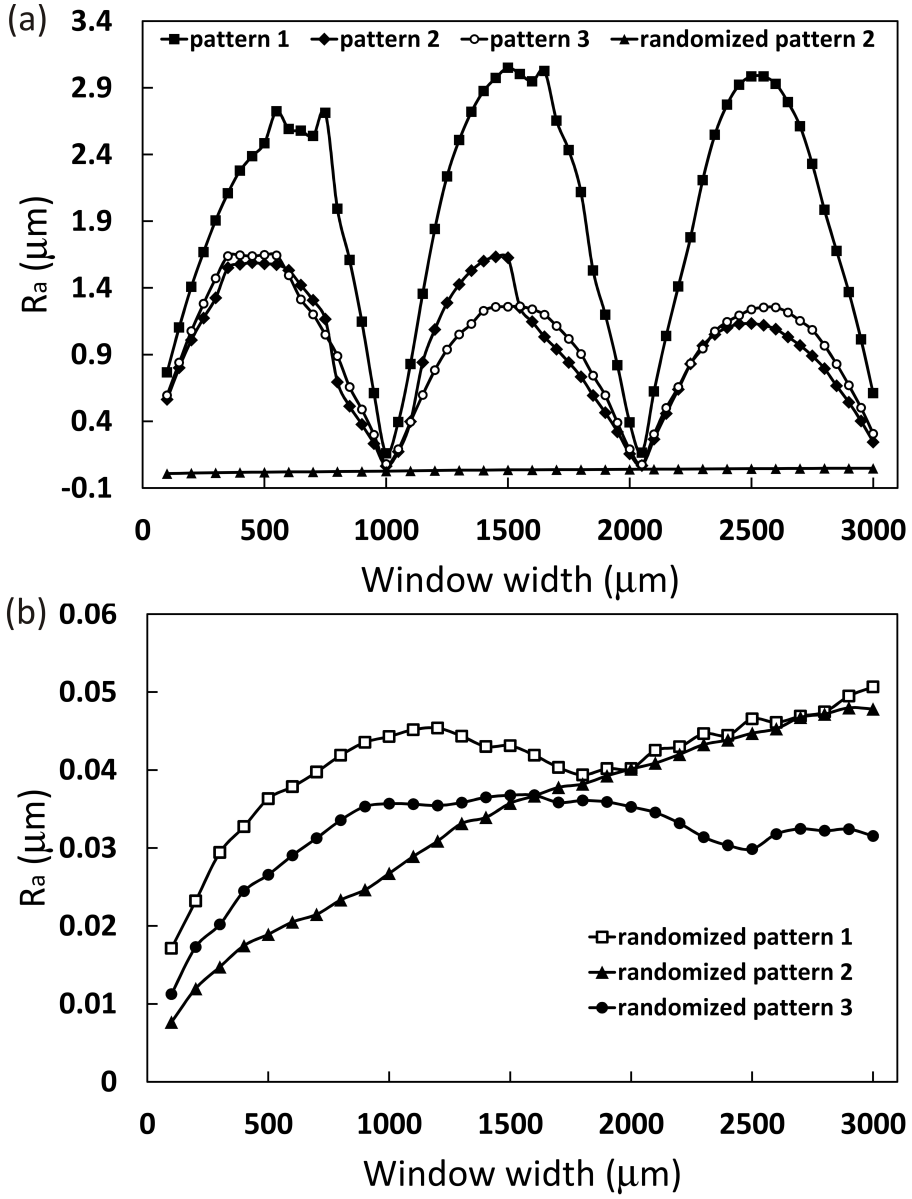

Fig. 2.17: Effect of the window width on the simulated arithmetic mean roughness for banded R/cube and spatially randomized patterns.

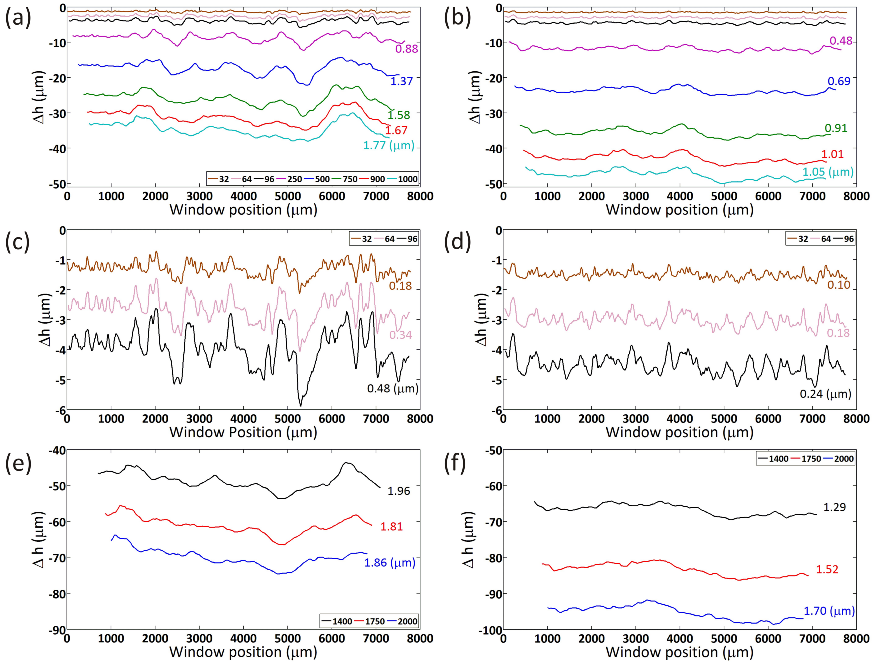

Fig. 2.18: Hypothetical surface profiles simulated by the mesoscopic MW model using various window widths based on the experimentally measured EBSD orientation maps for (a, e) the roping sample and (b, f) the non-roping sample; three profiles of (c) the roping sample and (d) the non-roping sample rescaled from (a) and (b), respectively. Note that R_a is given to the right of each profile.

simulated with window widths smaller than $100\mu m$ exhibited, besides the short-range (high frequency) fluctuations for the roping sample, long-range undulations with a wavelength of approximately $1mm$, whereas no obvious long-range undulation could be identified for the non-roping sample. When the window width was between $250\mu m$ and $750\mu m$, the long-range undulation of the roping sample became more obvious (see Fig. 2.18a). The wavelength estimated from the curves in Fig. 2.18a was between $1mm$ and $2mm$. However, two peaks at positions of $2800\mu m$ and $4000\mu m$ started to emerge at the window width of $250\mu m$ and rose with increasing window width for the non-roping sample (see Fig. 2.18b). Nevertheless, there was no significant periodic trend in Fig. 2.18b. Therefore, the observed differences of the simulated surface profiles between both samples may imply that the proposed MW mesoscopic model is able to predict the roping propensity. This can be directly seen in Fig. 2.19, in which the surface profiles simulated using a window width of $500\mu m$ for both samples are compared. The MW simulation can predict the roping wavelength based on the spatial texture distribution. The ODF analysis of the spatial texture heterogeneity is

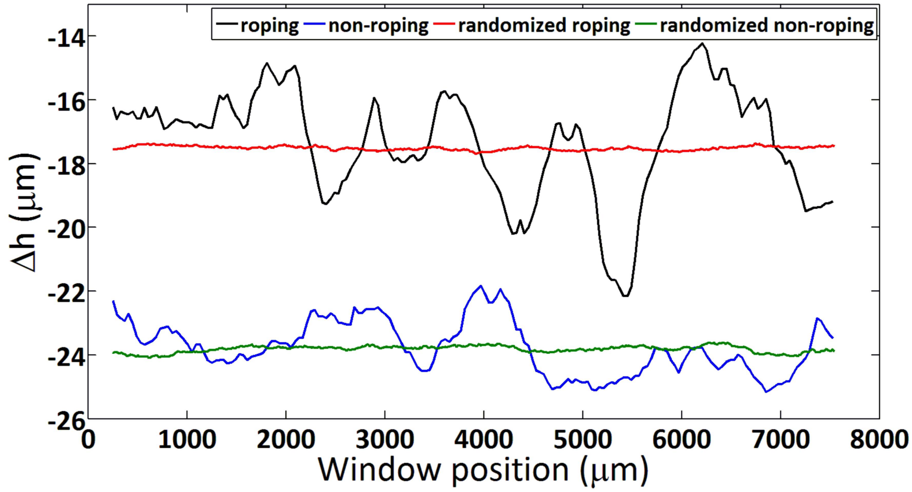

Fig. 2.19: Hypothetical surface profiles simulated by the mesoscopic MW model using window width of $500\mu m$ based on EBSD orientation maps of both roping and non-roping samples and on the spatially randomized roping and non-roping EBSD maps.

given in Appendix B.

On the right of each curve in Fig. 2.18, the corresponding R_a is shown. For either sample, R_a increased with increasing window width. This monotonic increase in R_a could be attributed to two aspects: one was that the height of the M-RVE increased with increasing window width, which involved more grain layers in ND (this can be seen in the analysis based on the randomized R/cube patterns in Fig. 2.17b); the other was that the major inherent wavelength of the banded texture distribution was greater than $1000\mu m$. Furthermore, it is interesting to note that the R_a corresponding to the window size of a single grain cluster, i.e. $32\mu m$, was much lower than that observed in roping samples subject to a plastic deformation of 0.15 [9, 25]. This finding indicates that a layer of surface grains cannot lead to considerable roping amplitude.

Fig. 2.20 shows the effect of the window width on R_a for both roping and non-roping samples. In this case, the physical constraint, i.e. $w < 1.01mm$, on the window width was relaxed to explore the wavelength of texture bands distribution. Unlike the R_a trend for the artificial EBSD maps (Fig. 2.17), no abrupt R_a variation could be found for both roping and non-roping samples. Specifically, R_a increased monotonically until the maximal window width of $3000\mu m$ for the non-roping sample, whereas a shallow fluctuation with a minimum point could be identified on a generally increasing R_a trend for the roping sample. These observations indicate that no periodicity of the wavelength range between $100\mu m$ and $3000\mu m$ is present for the non-roping sample, whereas a wavelength of $1750\mu m$, corresponding to the local R_a minimum, can be

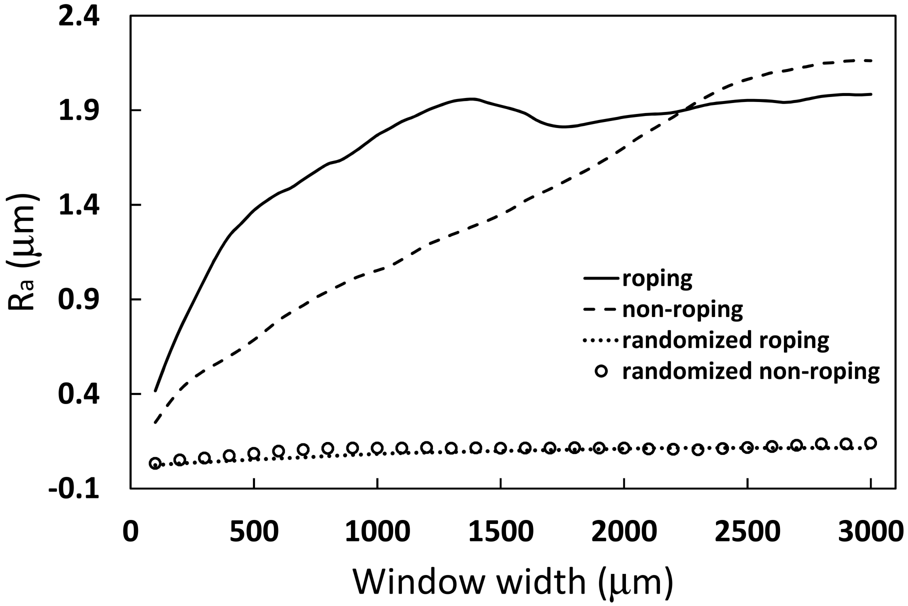

Fig. 2.20: Effect of the window width on the simulated arithmetic mean roughness for the roping and non-roping sample and their corresponding spatially randomized samples.

identified for the roping sample. These findings are consistent with the aforementioned wavelength analyses based on the simulated surface profiles in Fig. 2.18. It is worth noting that the coordinate along TD after UT-TD deformation was not updated but kept the same as before deformation in order to facilitate direct comparison of EBSD maps with simulated roping profiles (see Figs. 2.16 and 2.18). Therefore, a factor of 1.16 corresponding to $\epsilon_{TD} = 0.15$ should be multiplied to TD coordinate, if the simulated roping wavelength after UT deformation was compared with that observed experimentally. Thus, the resulting wavelength is $2.03mm$, which is close to the roping wavelength, $1.64mm$, determined by the PSD analysis (see Fig. 2.11). The difference in wavelength could be due to the fact that the EBSD and surface measurement was not done in-situ. The EBSD measurements, on which the surface profiles were simulated based, were done on specimens which were different from those of the surface measurements. Nevertheless, the identification of local R_a minima can be used to find the predominant wavelength component of the texture bands distribution quantitatively.

Moreover, it can be seen in Fig. 2.20 that the window width of $150\mu m$ yielded R_a of 0.59 and $0.34\mu m$ for the roping and non-roping sample, respectively. These simulated R_a values corresponded well to those (0.53 and $0.35\mu m$) experimentally determined from the RD-averaged surface profiles in Fig. 2.12a and c. Therefore, the simulated surface profiles using the window width of $150\mu m$ for the roping and non-roping sample are shown in Fig. 2.12b and d, respectively. A moving average filter (MAF)[4] [123, 124] with the window width of $500\mu m$ was applied to the surface profiles in Fig. 2.12 to facilitate comparison with focus on long-range waviness. Evidently, a good agreement is shown between both the wavelength and amplitude of the surface profiles predicted by the MW method and experiments for both samples. This agreement proves the validity of MW method in roping analysis. This finding suggests that a depth of approximately $75\mu m$ should contribute to surface roughening in these AA6xxx sheets studied. As already mentioned in Refs. [21–23, 73], the plastic deformation of subsurface layers, namely the through thickness distribution of grains, can play an important role in promoting roping. Among them, Lefebvre *et al.* [23] used a VPFFT model to simulate roping based on an experimentally measured EBSD map in the ND/TD plane. Their VPFFT approach focused on grain-to-grain interactions by conducting crystal plasticity simulations and simultaneously solving the governing equations of equilibrium of stresses and compatibility of deformations for each EBSD data point, which was treated as a periodic polycrystal. Their results showed that the neighbor-neighbor interactions tend to strongly perturb the behavior of orientations that tend to cause shearing. However, their predicted surface profile spanned less than one experimentally measured roping wavelength due to their very limited simulation domain. It is preferred to have simulation results including more roping waves in order to draw a solid conclusion on comparison of surface roughness profiles between the VPFFT simulations and experiments. In contrast, the present MW approach uses the FC Taylor model to simulate a r-value for a number of grains belonging to a M-RVE, within which the strain compatibility is maintained. Distinct from Lefebvre's method, this MW method focuses on the collective mechanical response of a group of grains within a meso-scale volume lying in between the scale of the individual grains and the macro-scale of roping. Surface EBSD maps were used to demonstrate the predictive capability of the present model and to facilitate better comparison with surface topography measurement data. With RD/TD EBSD maps at various levels through the thickness direction, one can definitely get better understanding of roping. Unfortunately, those data are not available for the present study. Although the present case is done in the RD/TD plane, the MW model can be readily applied to EBSD maps in the ND/TD plane. For both approaches, the crystallographic orientations were not updated, i.e. no texture evolution was considered.

Fig. 2.19 also compares the simulated surface profile of the roping sample with that of the randomized roping EBSD map (see Section 2.3.3). The spatially randomized EBSD map resulted in nearly no surface variation in contrast to the roping sample. This finding indicates that the mesoscopic banded texture distribution contributes to roping whereas the global texture has little influence on roping. Moreover, the difference in the profiles between the randomized non-roping and the original non-roping sample can be seen in Fig. 2.19. This finding suggests that there exists a limited spatial

---

[4] The moving average filter (MAF) is a simple Low Pass FIR (Finite Impulse Response) filter commonly used for smoothening an array of sampled data in the field of DSP (Digital Signal Processing). The MAF can be imagined as a window of a certain size (in this case $500\mu m$) moving along the array at a certain step size. The mean of all elements in the window is used to represent the value of this window.

texture inhomogeneity in the non-roping sample, though no clear periodicity can be identified based on the scale of the experimental EBSD map. Those findings together imply that roping is sensitive to a certain range of wavelengths of texture bands distribution, which is approximately between 1 mm and 2 mm.

2.5 Conclusions

Although the EBSD measurement can provide spatial orientation topography, the roping tendency cannot be quantified by visual assessment based on IPF-EBSD maps. Furthermore, the quantitative evaluation of the distribution of individual texture components cannot predict the roping tendency directly. Thus, it is recommended to understand roping with respect to banding of mesoscopic RVEs with contrasting textures instead of banding of grains having specific orientations.

The MW method, on which a meso-scale roping model rests, is proposed to bridge the spatial gap between the grain scale of the individual orientations and the macro-scale of roping. This simple roping model is based on the r-value prediction by the FC Taylor model. Local texture information of the statistically significant EBSD maps is selected by the MW, and then fed into the model to simulate roping. This MW tries to capture the plastically contrasting grain colonies, i.e. the hypothetical “ghost grains”, originating from the invisible mother grains at an earlier stage so that the influence of the thermo-mechanical history can be considered to interpret roping based on EBSD maps. In other words, roping can be interpreted as a result of the existence of volumes with contrasting textures at a meso-scale.

The MW simulations on artificial EBSD maps show that banding of texture components does not necessarily lead to roping. A difference in the r-value between neighboring bands is required to promote roping. It is also shown that the MW model is insensitive to the choice of the window width for identifying the roping wavelength. Furthermore, MW simulations are able to map the banded orientation distribution and predict the surface undulation. It is further shown that the window widths corresponding to the local minima in the R_a against window width curve can reflect the banding wavelength. Moreover, the global texture without spatial inhomogeneity per se is a necessary but not sufficient condition for roping. Thus, the spatial texture variation is a source of roping.

The application of the MW model to the experimental EBSD maps proves the capability of the model in the roping analysis. The model is able to predict both the wavelength and the amplitude with only the surface EBSD scan. It is found that the MW model using a window width of $150\mu m$ can predict both the wavelength and the amplitude of the roping profiles of the studied samples statistically (see, e.g. Fig. 2.12). Besides, it is demonstrated that a layer of surface grains cannot lead to considerable roping amplitude. However, the amplitude can be achieved by involving a number of subsurface grain layers to a depth of $75\mu m$ with an assumption of the homogeneous through thickness texture distribution.

Chapter 3

Moving window simulation on through thickness texture distribution

> *"All our knowledge begins with the senses, proceeds then to the understanding, and ends with reason. There is nothing higher than reason."*
> Immanuel Kant

3.1 Introduction

Experimentally, roping in ferritic stainless steels (FSS) [18, 19] is accentuated by doing a UT test with the TA parallel to RD. The deformed FSS sheets display corrugated roping characteristics, with ridges on one side of the sheet corresponding to valleys on the opposite side [25, 30]. In contrast, roping in Al alloys is aggravated by UT deformation with the TA parallel to TD [9, 25, 44, 46–48]. Roping of a ribbed type, i.e. with ridges on one side of the sheet corresponding to ridges on the opposite side, was observed in an AA3xxx sheet [46]. However, the frequently observed roping in AA6xxx sheets is of the irregular type, i.e. with the roping topographies on both sides of the sheet being uncorrelated to each other [25]. Those distinct roping features between FSS and Al alloys imply that different mechanisms may operate, i.e. the texture variation through the thickness direction is different.

Different theoretical models [18, 24, 27–29] have been proposed to explore the origin of ridging in FSS. All these models, which are based on spatial texture variation and crystal plasticity, have significantly improved understanding of ridging. However, ridging in FSS is beyond the scope of the present work.

The corrugated roping morphology in FSS basically implies that grains through the thickness direction deform in a coordinated manner, which was revealed by a VPFFT model with focus on local grain interactions [23]. The collective plastic behavior of grains through the thickness was widely accepted for modeling ridging in FSS. In contrast, roping in Al alloys was considered to be originating from inhomogeneous plastic deformation of grains at the free surface or subsurface. Engler *et al.* [9] stressed the importance of the plastic contribution of grains located at subsurface layers. Guillotin *et al.* [54] did a correlation study and found plastic strain variation of a layer at 50 μm below the surface correlated best with its roping profile. The present authors [99] found that a number of subsurface grain layers would contribute to the surface roping profile. All these studies indicate the importance of the influence of plastic behavior of grains underneath the ones at the outermost surface on the formation of the roping profile. All the evidence leads us to the hypothesis that roping in Al alloys can be a result of collective behavior of grain clusters at the surface and subsurface.

In this chapter, roping in Al alloys is regarded as a result of collective behavior of grain clusters at the surface and subsurface. Then, the relevant question is what is the minimal depth of material from the sheet surface that distinguishes the roping sample from the non-roping. To tackle this question, the meso-scale "moving window" model has been adapted to numerically simulate the surface profile based on through-thickness EBSD maps in an aluminum metal sheet under UT testing. The measured EBSD data on the cross section were directly incorporated into this meso-scale MW model, in which the FC Taylor model was used to describe the constitutive plastic response for the polycrystals in each window. The through-thickness texture gradient was discussed. Moreover, the collective mechanical behavior of the subsurface layers of grains was studied to approximate the depth until which the microstructure is most likely contributing to surface roughening. Statistical correlation between experimental and simulated surface profiles was studied. It has been statistically found that a minimal thickness of 8 ± 2 layers of grains close to the surface contributes to surface roughness for both roping and non-roping samples.

3.2 Experimental

3.2.1 Alloys and sample preparation

Two samples, designated as roping and non-roping, respectively, were used. The roping sample is known to show severe roping after tensile plastic deformation in TD, while the non-roping sample gives little roping after stretching in TD. Both samples have been taken in T4 state prior to the final forming process. Detailed sample description has already been given in Section 2.2.1.

3.2.2 EBSD measurement

Micro-textures on the two different samples were measured using automated EBSD using a Field Emission Gun Scanning Electron Microscope (FEG-SEM). Before the EBSD measurements, both samples were mechanically polished down to 0.10 μm followed by electro-polishing (30V, -30°C) for 60s using an electrolytic solution consisting of 70% ethanol, 10% 2-butoxyethanol, 8% perchloric acid and 12% distilled water.

The EBSD maps in the TD/ND plane, i.e. the cross section normal to RD, were measured to investigate the distribution and morphology of the (possible) texture bands through the sheet thickness. For EBSD measurements in the TD/ND plane, cautions should be taken when electro-polishing the samples. It is very important to retain the surface edges, so that the orientation information close to the outermost surface planes can be obtained, which is lost by the samples with their RD/TD plane polished. Fig. 3.1b shows the edge loss in a ordinary electro-polishing set-up (Fig. 3.1a). Using the sandwich design in Fig. 3.1c can retain both surface edges of the middle sample after electro-polishing as shown in Fig. 3.1d.

The TSL OIM software was used for the grain size and morphology analyses. EBSD orientation maps including more than 5000 grains were obtained with a scanning step size of $2\mu m$. Fig. 3.2 shows a part of the IPF maps of both samples with grain boundaries higher than 5° indicated by black thin lines. The color coding scheme is defined according to the crystallographic direction along the sample's ND. By assuming a circular grain shape, the calculated average grain diameter is approximately $20\mu m$ and $23\mu m$ for the roping and non-roping sample, respectively. It can be seen in Fig. 3.2 that most grains are compressed in ND. Fig. 3.3 shows the grain size distributions on the through-thickness plane for both samples. It can be seen in this figure that both samples have a similar grain size distribution based on EBSD measurement on the TD/ND plane. The average intercept lengths (excluding edge grains of the EBSD orientation maps) determined by using 289 lines parallel with ND are $13\mu m$ and $16\mu m$ for the roping and non-roping sample, respectively. Then the grain aspect ratio, i.e. the ratio of the minor axis to the major axis of the ellipse fit to a grain, averages at 0.43 and 0.48 for the roping and non-roping sample, respectively.

For the large-area EBSD measurements, magnifications of higher than 200X were used to avoid significant image mismatch when stitching neighboring scans. The obtained EBSD maps are $11416\mu m$ (in TD) by $972\mu m$ (in ND) for the roping sample and $12940\mu m$ (in TD) by $1056\mu m$ (in ND) for the non-roping sample. The step size of both maps was $4\mu m$. The original gauge thickness was $1.01mm$ and $1.16mm$ for the roping and non-roping sample, respectively. Thus, several layers of grains at the free surfaces were lost for both samples due to previous oxidation of the surface grains, electro-polishing and image trimming to obtain rectangle EBSD maps. Information on the grain size and shape and sheet thickness is summarized in Table 3.1.

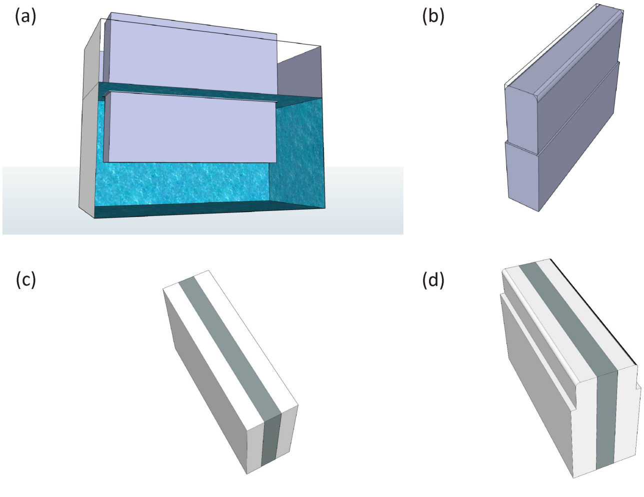

Fig. 3.1: Schematic illustration of the strategy of the electropolishing in order to retain the surface edges. (a) A sample is immersed in an electrolytic bath. (b) The sample geometry after electropolishing without edge protection prior to polishing. (c) A sandwich design to protect both surface edges of the sample in the middle. (d) The surface finish after electropolishing in case of edge retention of the middle sample through the sandwich design.

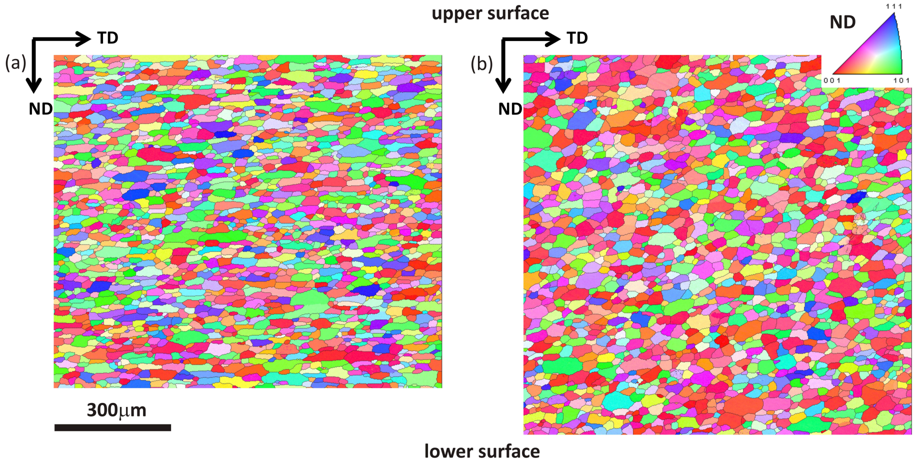

Fig. 3.2: IPF maps of (a) roping and (b) non-roping samples with color coding according to their crystallographic direction along the sample's ND. Note the entire thickness in the ND is characterized.

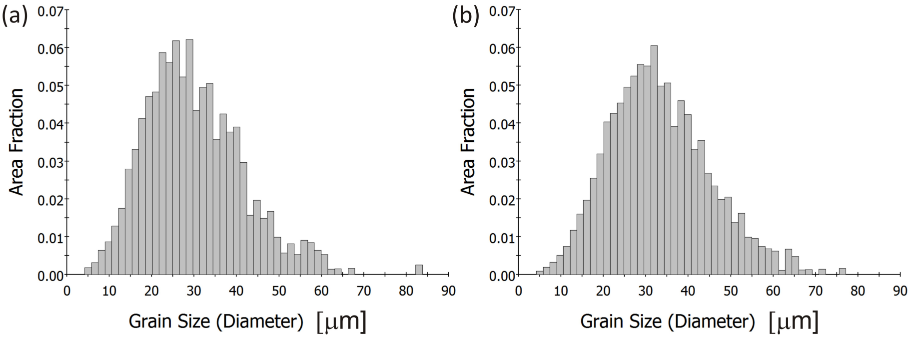

Fig. 3.3: Grain size distribution of (a) roping and (b) non-roping sample on the through-thickness plane, i.e. the TD/ND plane.

Table 3.1: Summary of grain size and shape and sheet thickness of both samples.

	Roping	Non-roping
Grain size in ND (intercept) (μm)	13	16
Original sheet thickness (μm)	1010	1160
EBSD map height (in ND) (μm)	972	1056
No. of layers of grains (measured by EBSD)	78 (75)	73 (66)
Aspect ratio (ellipse fitting)	0.43	0.48
Calculated grain size in TD (μm)	30	33

3.2.3 ODF

For information concerning ODF calculation, please refer to Appendix B.

3.2.4 Surface topography measurement

A Wyko non-contact white light interferometer was used to characterize the surface of both samples after a plastic tensile strain of 0.15 in TD. The Wyko surface measurements were done on the RD/TD plane using a low magnification (0.8x) objective lens. Before the tensile tests, the dog-bone shaped tensile samples were polished carefully to mirror finish to increase the white light reflection. Due to difficulty in sample preparation [75, 76, 91, 92], it was not possible to measure the surface roughness on the exactly same location of the same specimen, where the EBSD measurement had been done, after UT deformation in TD. Therefore, the Wyko specimen used was different from the EBSD one for either sample. This is the reason why statistical comparisons between a simulated surface profile and an experimentally measured one is needed (see Section 3.4).

3.3 Modelling strategy

The present study uses the MW method to select a M-RVE at the surface with a characteristic local texture, on which a UT test simulation in TD is based. By minimizing the plastic power dissipation per unit volume, the r-value is predicted using the FC Taylor model. Then, the thickness change of the M-RVE is obtained to represent the surface profile. The modelling philosophy, especially, the boundary conditions, has been described in detail in Section 2.3 (see, also Ref. [99]). In the present study, the potential slip systems are $\{111\}\langle 110\rangle$.

Unlike the previous simple mechanical analysis, which is based on surface (the RD/TD plane) EBSD maps, the present study uses the EBSD maps on the cross section normal to RD, i.e. the TD/ND plane. With such EBSD maps, the through-thickness texture information can be accessed. Therefore, the assumption of no texture gradient in ND is no longer needed. However, a through-thickness map reveals very limited information on microstructure in RD. The simulated surface profiles based on through-thickness EBSD maps should be compared with experimental stylus surface profiles. The simple meso-scale MW mechanical model based on through-thickness EBSD maps is schematically illustrated in Fig. 3.4.

Firstly, a TD/ND plane EBSD map is assumed to represent the crystal orientation distribution through the thickness as shown in Fig. 3.4(a). The dashed middle line in Fig. 3.4 divides the sheet into two halves, i.e. the upper and the lower half due to the fact that the development of roping on the upper and lower surfaces in Al samples is identified to be irregular as defined in Ref. [25]. The upper and the lower half sheet will be analyzed separately. Herein, only the mechanical analysis on the upper half of the sample thickness, $t_0/2$, is illustrated.

Secondly, a group of grains can be selected by a window on top of the EBSD orientation map as illustrated in Fig. 3.4(b), where the window width is w and the original window height is h_0. This window corresponds to a M-RVE, which is assumed to behave as an ideal standard free-standing tensile test sample. Therefore, the initial thickness of the M-RVE, h_0, corresponds to that of the surface layers as shown by the hatched volume in Fig 2.4. The intermediate transition layers, which are believed to exist between the stress boundary condition dominated surface layers and strain boundary condition dominated central layers, will not be selected by the MW in the present study. Details on boundary conditions are referred to Section 3 of Ref. [99].

Then, a tensile test in TD would result in a thickness change of the M-RVE, Δh, as shown in Fig. 3.4(c). Herein, a logarithmic plastic strain of 0.15 in TD is imposed in all the MW simulations.

If the window moves continuously scanning the entire EBSD map, the mechanical response of all the possible grain clusters (likely corresponding to "ghost grains") can be analyzed by simulating the thickness change of all the corresponding M-RVEs. Consequently, the roping profile can be obtained by plotting the thickness change of grain clusters versus their corresponding position. When the window size matches the

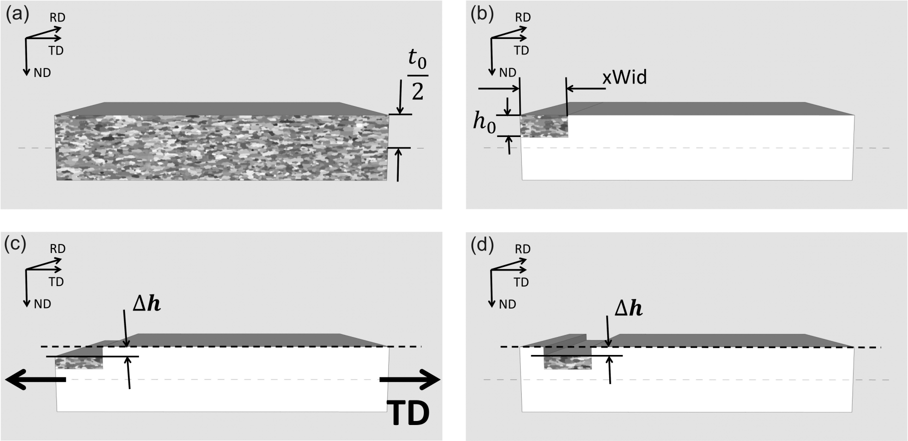

Fig. 3.4: Schematic illustration of the MW method in the TD/ND plane.

characteristic dimension of the grain clusters, the roping tendency can be expected to merge.

By varying the height of the MW, different layers of grains in ND can be chosen and fed into the simple mechanical model to simulate their corresponding surface profiles. Then, it is possible to use the simulated roping profile to understand how the local strain heterogeneities caused by the through thickness distribution of texture bands at different depths can add up to significant surface height variations, that is to say, to noticeable roping heights. This is due to the fact that the surface profile simulated by the MW model is the outward manifestation of spatial texture distribution. It is worth noting that the upper and the lower half sheet will be analyzed separately because the roping type in AA6xxx alloys is characterized to be irregular[25].

r_{TD} is calculated to characterize the through-thickness texture gradient, since tensile tension in TD is frequently used to reveal roping. In this case, the window width is chosen to be equal to the entire length of TD and the height is set to $32\mu m$ in ND. Then the window moves downwards at a step of $16\mu m$ through the entire sample thickness (see Fig. B.10). It is worth noting that it might be impractical to solely compare the ODF sections to reveal the through-thickness texture gradient since the difference in those ODF sections can hardly be distinguished visually.

3.3.1 Layer-wise moving window simulation

It is interesting to see how individual layers of grains would behave if they are regarded as the ones at free surface. By setting the window height to $16\mu m$, which is the average grain size in ND of the non-roping sample, the mesoscopic spatial texture distribution could be analyzed layer by layer (with layer, an individual layer of grains is meant) using the EBSD orientation map. To facilitate comparison, the same window thickness, i.e. $16\mu m$, was used for the roping sample too. This was due to a practical limitation, i.e. the step size of the large scale EBSD measurement was $4\mu m$.

The R_a-value was calculated to characterize the roughening propensity of each individual layer of grains. The window widths of 32, 64, 96, 128 and 160 μm were used to check the effect of window width on roughness prediction. Note that the width of $32\mu m$ corresponded to the average grain size in TD. So, the width of $160\mu m$ could include on average 5 grains in a window. The correlation between the simulated profiles was calculated to analyze the mesoscopic texture inhomogeneity.

3.3.2 Incremental thickness moving window simulation

It is expected that the surface profile is a result of collective plastic deformation of grains at the free surface and the sub-surfaces. Let the MW begin with the top surface layer. Then, increasing the window height incrementally includes more layers of grains below the free surface. Therefore, the collective behavior of grains within a M-RVE from the free surface can be quantitatively analyzed through crystal plasticity computation. Consequently, the influence of subsurface layers in the through thickness direction on the surface profile can be investigated.

In this case, the window width was fixed to $160\mu m$, different window heights were used to include various depths of grain layers in ND. The simulated surface profiles were compared with the Wyko TD-stylus-profiles statistically in terms of R_a and frequency spectrum. A preliminary minimal thickness of material contributing to the surface roughness could be approximated. With the approximated minimal thickness, simulations on the lower half sheet could be compared with those on the upper half to study the correspondence of the surface profiles.

According to Eq. 2.4, Δh increases with increasing h_0, i.e. window height, if ϵ_{TD} and r_{TD} are not changed. This then leads to an increase in R_a (see, Eq. 2.5). This geometrical influence of h_0 can be understood by performing surface profile simulation on ideally homogeneous microtexture, which results in no r_{TD} variation. Such a microtexture can be numerically generated by randomly shuffling the spatial coordinate of an existing EBSD map. More specifically, the spatial orientation distribution of this EBSD map is randomized but its orientation information is unchanged. Therefore, the global texture of the randomized EBSD map is the same as that of its corresponding input map. This spatial coordinate randomization was done for the EBSD maps of both roping and non-roping samples. Moreover, the geometrical influence of h_0 could be eliminated by calculating arithmetic mean roughness of r_{TD}-profiles. This $R_a\_r_{\mathrm{TD}}$ can be computed using Eq. 2.5 by simply replacing all h with r_{TD}.

3.4 Statistical and numerical parameters

In order to compare the experimental and simulation results quantitatively, statistical parameters, such as arithmetic mean roughness, R_a, and correlation coefficient, ρ, were used. R_a [115] is frequently used to characterize the surface roughness quantitatively. A characteristic wavelength, λ, is used to quantitatively analyze the spectral properties of a surface profile.

3.4.1 Arithmetic mean roughness

R_a was used to represent the statistical distribution of surface height. It is defined in Eq. 2.5. The surface roughness can be quantitatively described by this compacted single parameter. It is worth noting that R_a is of statistical significance to characterize surface roughness. Specifically, R_a was calculated based on the discrete data of the surface profiles from both experiment and simulation.

3.4.2 Fourier spectral analysis

Discrete fast Fourier transform (FFT) is frequently used to analyze the periodical phenomena such as roping profiles [54]. The FFT transforms a surface profile from the spatial domain to the frequency domain, in which this profile is decomposed into a series of frequency components. The characteristic spatial texture distribution can be identified in terms of a predominant frequency, f, corresponding to the highest amplitude. In event of roping, λ, which is simply the inverse of f, is preferred. Therefore, the dominant wavelengths can be sought by spectral analysis based on the FFT.

3.4.3 Correlation coefficient

A linear correlation coefficient, ρ, can be used to quantitatively compare two data sets, x_i and y_i, where $i = 1, 2, ..., n$. The correlation coefficient is calculated by Eq. 3.1.

$$\rho_{xy} = \frac{cov(x, y)}{S_x S_y}. \tag{3.1}$$

In this, $cov(x, y)$ is the covariance between x and y and S_x and S_y the sample standard deviation of x and y, respectively. It is worth noting that Eq. 3.1 gives the definition of sample correlation coefficient, which is commonly represented by the letter r. However, the Greek letter ρ, which is usually referred to as the population correlation coefficient, is adopted herein to be distinguished from the strain ratio, or Lankford coefficient, r in this thesis.

ρ_{xy} is a measure of the linear interdependence of x and y in the sense that its value is a measure of accuracy with which x can be approximated by a linear function of

y [125, 126]. The value of ρ_{xy} always lies between -1 and 1. If $\rho_{xy} = 0$, there is no linear association between x and y. $\rho_{xy} = 1$ indicates that x and y are positively linearly perfectly correlated, whereas $\rho_{xy} = -1$ indicates that they are negatively perfectly correlated. A greater $|\rho_{xy}|$ indicates a stronger association between x and y [127]. Herein, the correlation coefficient was used to describe quantitatively the similarity between two hypothetical profiles. It was also used to quantify the similarity of the FFT spectra between the Wyko TD-stylus profiles and the hypothetical profiles simulated by the MW model.

3.5 Results and discussions

3.5.1 EBSD analysis

The EBSD orientation maps are shown in Fig. 3.5. The texture components are extracted from these EBSD orientation maps to check their distribution through the thickness direction, i.e. ND. The thinning susceptible orientations (with the r-value lower than 1), such as S, CH, R and Q, and the thinning resistant orientations (with the r-value greater than 1), such as Goss and CG, were separately extracted from the EBSD map as shown in Fig. 3.5. It can be seen clearly that the roping sample features more Goss and CG components than the non-roping sample. Visually, no banded distribution of texture components can be identified in both samples. This observation indicates that the banded texture distribution of the surface layer may not penetrate into the bulk. Furthermore, this implies that the thickness of the hypothetical "ghost grains" is at the same level of that of grains in T4 state due to a series of passes of rolling and annealing. It can also be seen in Fig. 3.5 that the roping sample contains more thinning resistant orientations than the non-roping one. Moreover, the central layers feature more Goss and CG components than the surface layers for the roping sample.

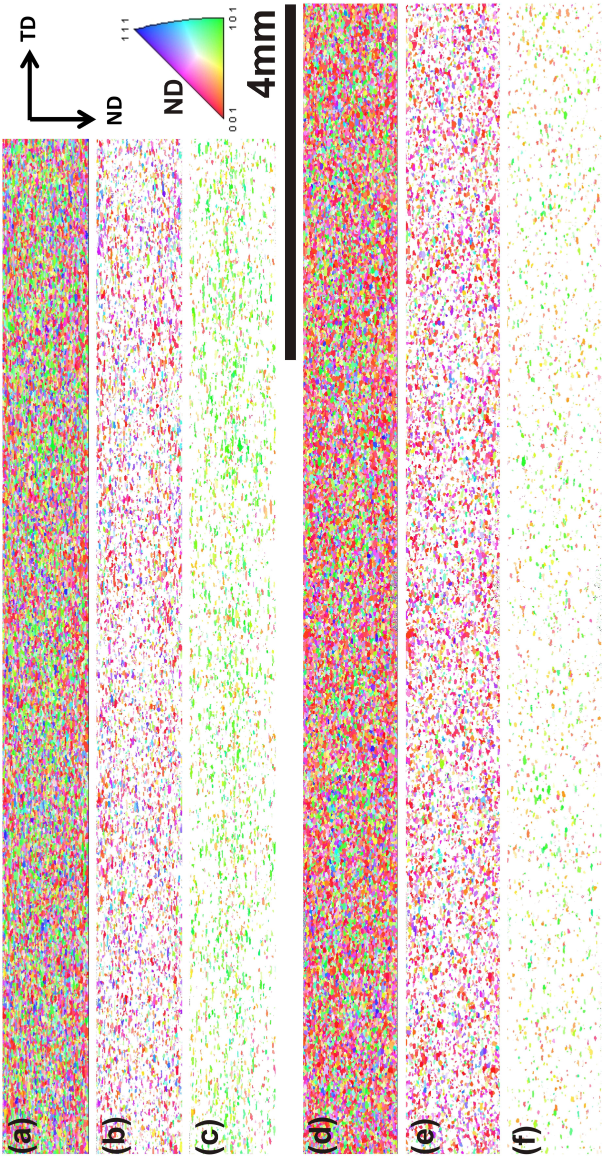

Fig. 3.5: EBSD IPF maps on the TD/ND plane (a) for the roping and (d) for the non-roping sample; IPF maps with only grains within 16.5° of exact S, CH, R and Q components (b) for the roping sample and (e) for the non-roping sample; IPF maps with only grains within 16.5° of exact Goss and CG components (c) for the roping sample and (f) for the non-roping sample.

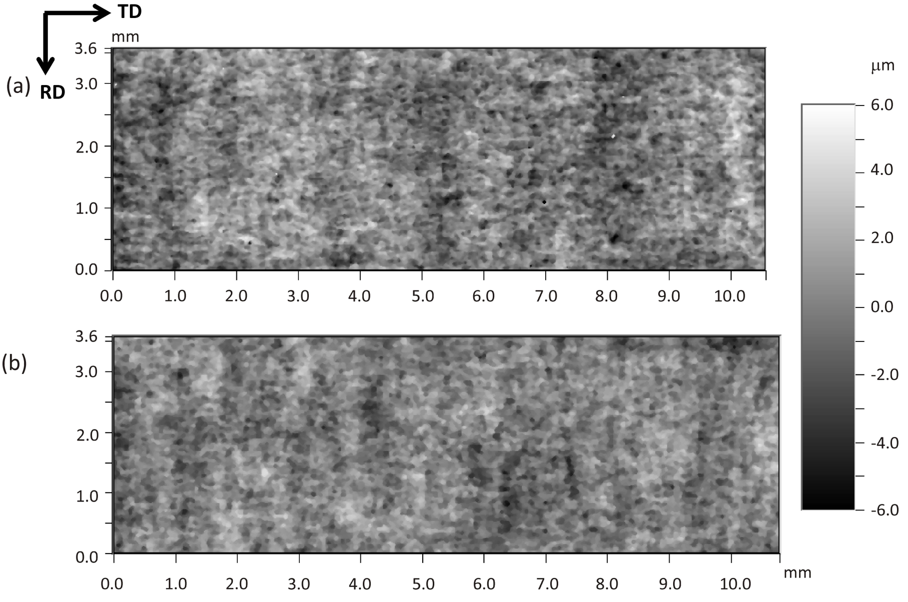

Fig. 3.6: 2D surface topography measured on the RD/TD plane after 15% plastic deformation along TD for (a) the roping sample and (b) the non-roping sample with the grey code on the right referring to the surface height in ND.

3.5.2 ODF analysis

ODF analysis is given in Section B.2.

3.5.3 Surface analysis

The measured surface topography maps on the deformed samples are shown in Fig. 3.6. A height profile cut by a line along TD is called a TD-stylus profile throughout this thesis. Due to the lack of in situ correlation between the surface data and the microtexture data, statistical analysis becomes necessary to obtain reliable results.

An R_a-value can be obtained for each TD-stylus profile. For the measured surface topography maps of both samples in Fig. 3.6, R_a-values of all the TD-stylus profiles are calculated and plotted against their position in RD as shown in Fig 3.7. It can be seen that both samples feature R_a variation along RD, indicating inhomogeneous plastic deformation in RD. $\bar{R_a}$ calculated by averaging all R_a-values along RD is $1.20\mu m$ and $1.02\mu m$ for the roping and non-roping sample, respectively. Thus, the roping sample generally shows higher R_a than the non-roping sample. This means

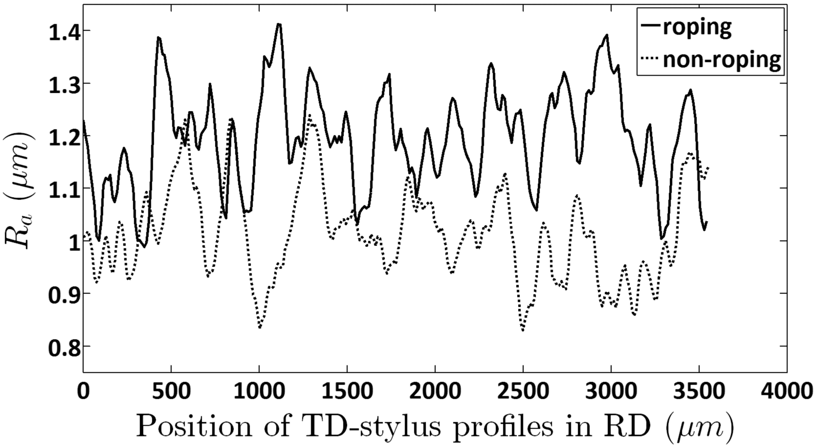

Fig. 3.7: Arithmetic mean roughness of TD-stylus profiles along RD.

that the roping sample exhibits a rougher surface than the non-roping one after the UT deformation in TD.

3.5.4 Roughening analysis using layer-wise microtexture

Hypothetical profiles were obtained for individual layers of grains, i.e. mono-grain-layers. For both samples, the window height was fixed to be $16\mu m$. Fig. 3.8 shows R_a of all mono-grain-layers in the upper half sheet for both samples. It can be clearly seen that the roping sample always yields higher R_a than the non-roping one for each mono-grain-layer. This result agrees with the experimental observation that the roping sample exhibits a higher surface roughness than the non-roping one as shown in Fig. 3.7. It should be reminded that the simulated surface profile is simply the mechanical consequence of the spatial texture distribution in the MW. Therefore, the R_a difference between the roping and non-roping sample can be attributed to the difference in the spatial orientation distribution of mono-grain-layers. In the MW simulation, window widths corresponding to 1 to 5 grains were used to predict the surface profiles. Increasing the window width from $32\mu m$ to $160\mu m$ decreases the R_a-value for each considered mono-grain-layer. Note that a detailed discussion on the effect of window width has been given in Chapter 2. Therefore, no matter which window width was used, the simulated R_a-values based on the mono-grain-layers are much lower than those measured on the surface (compare Fig. 3.8 with Fig. 3.7). This indicates that a single layer of grains is not sufficient to promote the experimentally observed surface roughness.

Due to the fact that a mono-grain-layer is not enough to generate sufficient surface roughness, the plastic behavior of the material beneath the free surface comes into play

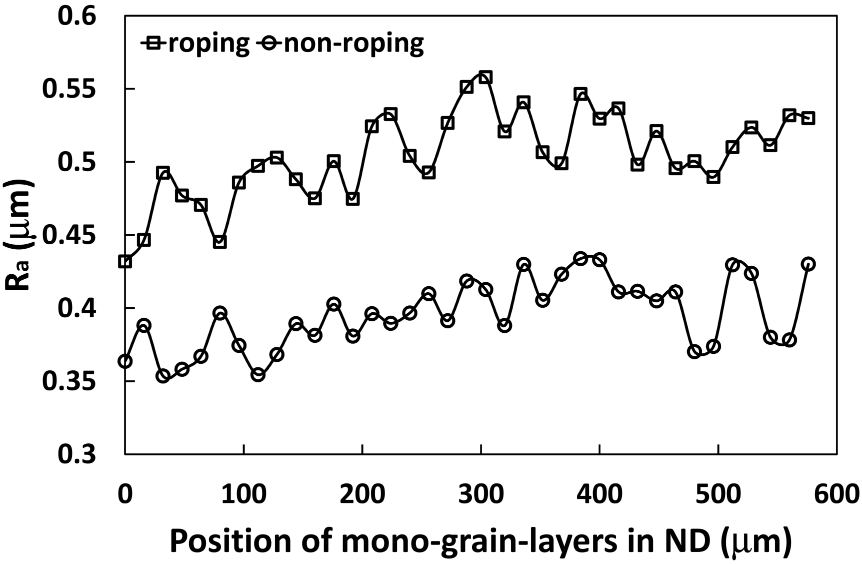

Fig. 3.8: R_a-values of all mono-grain-layers in the upper half sheet vs. their position in ND. The window width is $32\mu m$ and height is $16\mu m$ in the MW simulation.

for roping formation. Note that the mono-grain-layers were analyzed individually as if they behaved like surface grains. Therefore, the hypothetical profiles simulated by the MW model can reflect the plastic response of these mono-grain-layers upon loading. Furthermore, they can be used to represent the spatial distribution of mesoscopic texture to some extent, because the plastic response is a result of texture upon loading.

The correlation coefficient is used to quantitatively describe the linear inter-dependency between two simulated profiles. Thus, the similarity of the spatial distribution of mesoscopic texture between two mono-grain-layers can be quantified by this correlation coefficient to a certain extent. In other words, this correlation coefficient can serve as an indicator of whether the spatial texture distribution can persist in ND. Specifically, a positive correlation coefficient indicates that the spatial texture distributions of the two layers considered are similar. If these two are combined together, surface roughening will be strengthened. In contrast, a negative correlation coefficient indicates that the r-value distributions as a result of their corresponding spatial texture distributions are opposed. Then, the combination of the two layers will weaken surface roughening. When the correlation coefficient is close to 0, the two layers have low correspondence in the spatial texture distribution; whereas they have high correlation, if the correlation coefficient approaches 1.

Fig. 3.9 shows correlation coefficients between a reference mono-grain-layer and the other mono-grain-layers for both samples. In this figure, the horizontal axis is the

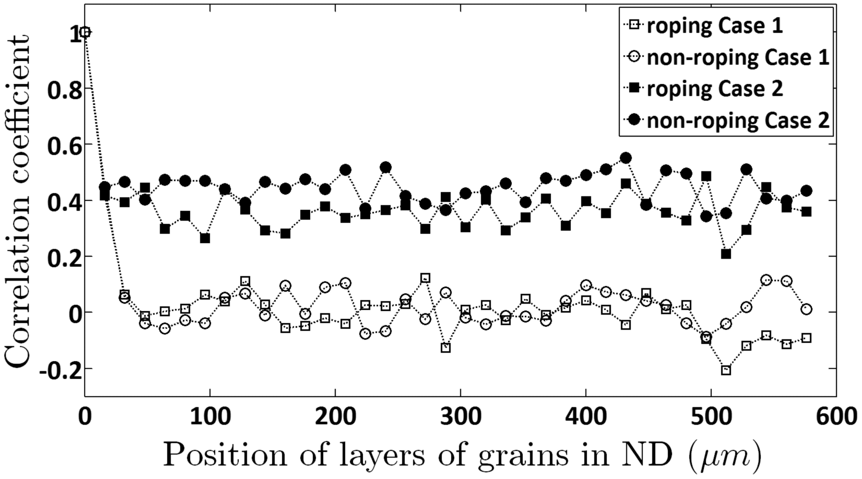

Fig. 3.9: Correlation coefficient between mono-grain-layers. The window width is $32\mu m$ and height is $16\mu m$ in the MW simulation. In the legend, Case 1 indicates that the reference mono-grain-layer is fixed to be the top surface layer, whereas Case 2 represents that the reference layer moves from the top surface layer to the middle of the sample.

distance of the upper edge of the other mono-grain-layer from the top surface in ND. When the top mono-grain-layer is fixed to be the reference one, the other one moves from the top surface to the middle of the sample. It can be seen in Fig. 3.9 that the correlation coefficient is 1 when the other-grain-layer is at the top surface, i.e. coincident with the reference mono-grain-layer, for both samples. When the other-grain-layer is beneath (and adjacent to) the top mono-grain-layer, the correlation coefficient decreases to be in between 0.4 and 0.5 for both samples. Therefore, these two layers are moderately correlated in terms of the spatial texture distribution. Then, moving the other-grain-layer away from the top layer makes the correlation coefficient fluctuate gently around 0 for both samples. This observation suggests that the grain layers at the subsurface and interior are hardly correlated with the one at the free surface with respect to the spatial texture distribution. In other words, the spatial texture distribution at the free surface does not penetrate into the bulk of both samples.

In another case where the reference mono-grain-layer moves from the free surface to the interior, the other mono-grain-layer is chosen to be the neighboring grain layer just beneath the reference one. It can be seen in Fig. 3.9 that the correlation coefficient between the neighboring grain layers fluctuate gently around 0.4, indicating the correspondence between these neighboring grain layers is moderate, for both samples. This observation implies that the spatial texture distribution changes gradually through the thickness direction for both samples. Besides, it can be suggested that no spatial texture distribution of a mono-grain-layer persists in ND. This finding confirms the earlier results that the texture bands are very thin, usually one or two grain layers only [9, 10, 73]. Therefore, one needs to think about several of these layers in order to explain the high surface roughness experimentally observed.

3.5.5 Roughening analysis using incremental thickness

Since a mono-grain-layer cannot induce sufficient surface roughness, the collective behavior of several mono-layers of grains from the surface and subsurface becomes crucial for roping formation. It is worth noting that the surface profile involving several mono-grain-layers is not simply the summation of the surface profiles of these layers. This is due to the fact that the grains in the interior are more constrained in ND than those at the free surface. The deeper the grains are inside a material, the higher the constraint they feel from the surrounding matrix. Therefore, it is necessary to simulate the surface profile for each increased window height. It is assumed that each selected M-RVE including the top surface grains and the added subsurface grains would behave as a free standing tensile test sample. This assumption therefore promotes surface roughening by neglecting the complex plastic behavior of the interior grains. Consequently, a minimal thickness of material contributing to the surface roughening can be approximated.

Fig. 3.10a shows two simulated profiles for the upper half surface of the roping sample. The first profile corresponds to a thickness of $16\mu m$ from the free surface, i.e. a mono-grain-layer. The second one is with a thickness of $104\mu m$, i.e. a summation of 5 mono-grain-layers from the free surface. It can be clearly observed that the second profile features a higher amplitude than the first one. This observation implies that addition of neighboring layers of grains to the top mono-grain-layer will increase the surface roughness. This is confirmed by calculating R_a for the simulated surface profiles with increasing thickness as shown in Fig. 3.11. It can also be seen in Figure 3.10a that addition of neighbouring layers of grains to the top mono-grain-layer will modify the position of peaks and valley. This is due to the fact that the spatial texture distribution changes in ND as shown in Fig. 3.9.

Fig. 3.11 shows the effect of increasing window height in ND on the surface roughness for the roping and non-roping as well as their corresponding randomized samples. Herein, the M-RVEs extend from the free surface to the interior and the upper and lower surfaces are analyzed separately. It can be seen in Fig. 3.11 that, increasing window height generally increases R_a for all samples. For the randomized samples, R_a increases very slightly. This indicates that the geometric effect of increasing h_0 is of much less importance, compared with the influence of spatial texture inhomogeneity. Therefore, in both roping and non-roping samples, increase of R_a is mainly due to spatial texture heterogeneity. It can also be seen in Fig. 3.11 that the roping sample exhibits higher surface roughness than the non-roping one for the same window height. This finding confirms that the roping sample features higher roughening propensity than the non-roping. This agrees well with the experimental observation as shown in Fig. 3.7. It can also be seen in Fig. 3.11 that the increase rate of R_a for the roping

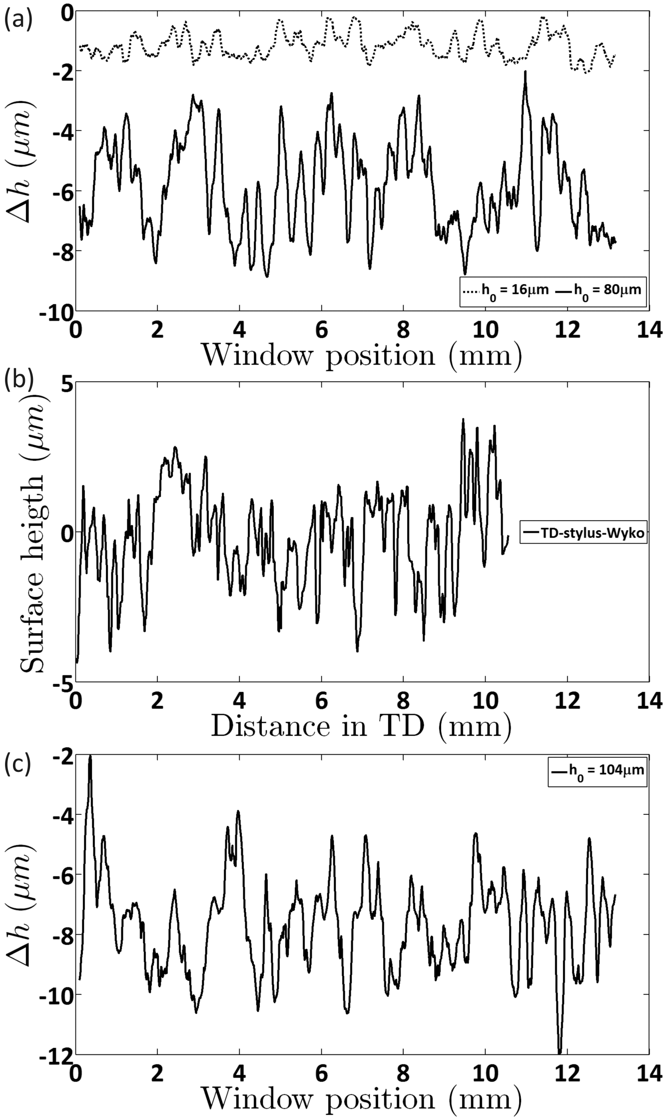

Fig. 3.10: Surface profiles of the roping sample. Hypothetical profiles simulated based on the EBSD data for (a) the upper and (c) lower surface. In the simulation, the window width is $160\mu m$ and the height is indicated in the legend. Note that all the M-RVEs in the MW simulation include the surface grains. Note also that window heights of $80\mu m$ and $104\mu m$ correspond to M-RVEs with 6 and 8 layers of grains, respectively. A TD-stylus profile (b) is randomly chosen from the experimental Wyko topography.

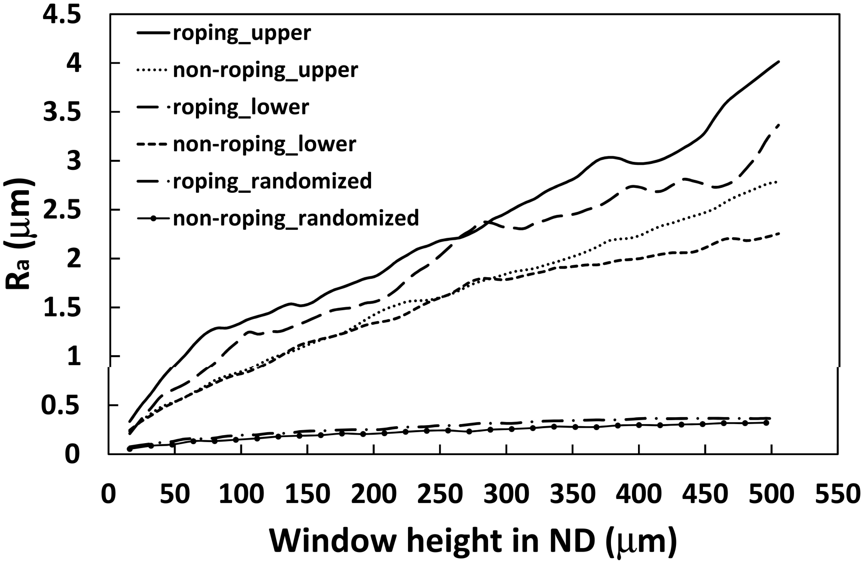

Fig. 3.11: R_a calculated based on the simulated surface profiles vs. window height in the MW simulation for both upper and lower surfaces of both samples. The window width is $160\mu m$, while the window height increases in ND in the MW simulation. Note that each M-RVE includes the grains at the free surface.

sample is higher than that of the non-roping with increasing window height up to approximately $100\mu m$. Beyond this point, it seems that both samples exhibit the same increase rate of R_a with increasing window height. This finding implies that the collective behavior of material up to a depth of approximate $100\mu m$ distinguishes the roping sample from the non-roping. A minimal thickness contributing to the surface roughening can be obtained by comparing Fig. 3.11 with the averaged experimental R_a-values, i.e. $\bar{R_a} = 1.20\mu m$ for the roping sample and $\bar{R_a} = 1.02\mu m$ for the non-roping. Therefore, the minimal thickness for the roping sample is $80\mu m$ and $104\mu m$ for the upper and lower surfaces, whereas it is $128\mu m$ for both surfaces of the non-roping sample. By dividing these minimal thickness values by their grain sizes in ND, which are $13\mu m$ and $16\mu m$ for the roping and non-roping sample, respectively, the number of layers of grains is approximately 8 for both samples. This finding suggests the first 8 layers of grains are crucial for surface roughening in both samples. If those 8 layers of grains behave together like the free surface grains, they are sufficient to induce the experimentally observed surface roughness. On the other hand, if addition of grains underneath those 8 layers still behave like the free surface grains, the hypothetical profile will get rougher than that experimentally observed. This is not possible in reality. Therefore, this may imply that the grains deeper than those 8 layers would be more constrained by their surrounding matrix.

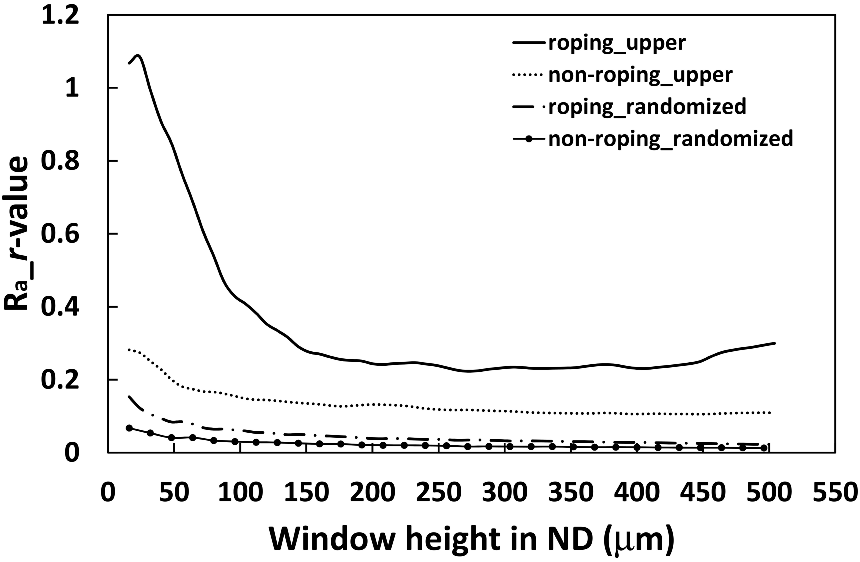

Fig. 3.12: R_a of r_{TD} calculated based on the simulated surface profiles vs. window height in the MW simulation for both upper and lower surfaces of both samples. The window width is $160\mu m$, while the window height increases in ND in the MW simulation. Note that each M-RVE includes the grains at the free surface.

It can be further seen in Fig. 3.11 that the increase rate of R_a becomes slower with increasing window height in ND for both roping and non-roping samples. This implies that the degree of spatial texture variation decreases with increasing h_0, which is confirmed by the R_a_r trend in Fig. 3.12. For the randomized samples, R_a_r is generally much lower and gets even lower with higher window height. This is expected since those randomized samples are designed to have very homogeneous microtexture. In contrast, the roping sample features a very high R_a_r with window height lower than $50\mu m$. Its R_a_r drops sharply with increasing h_0 and becomes stable when h_0 is larger than $150\mu m$. This implies for the roping sample that the degree of spatial texture heterogeneity becomes lower with higher h_0 until $150\mu m$. Beyond this point, it is constant. For the non-roping sample, its R_a_r behavior lies between the roping and randomized samples. Beyond $h_0 = 100\mu m$, the degree of spatial texture heterogeneity of the non-roping becomes stable too. Comparing the R_a_r trends between the roping and non-roping sample Fig. 3.12, one can see that the roping sample features a higher degree of spatial texture heterogeneity than the non-roping. The degree of heterogeneity decreases with increasing window height up to certain points and then becomes stable afterwards.

Fig. 3.13 shows the correlation coefficients between a hypothetical profile of a reference

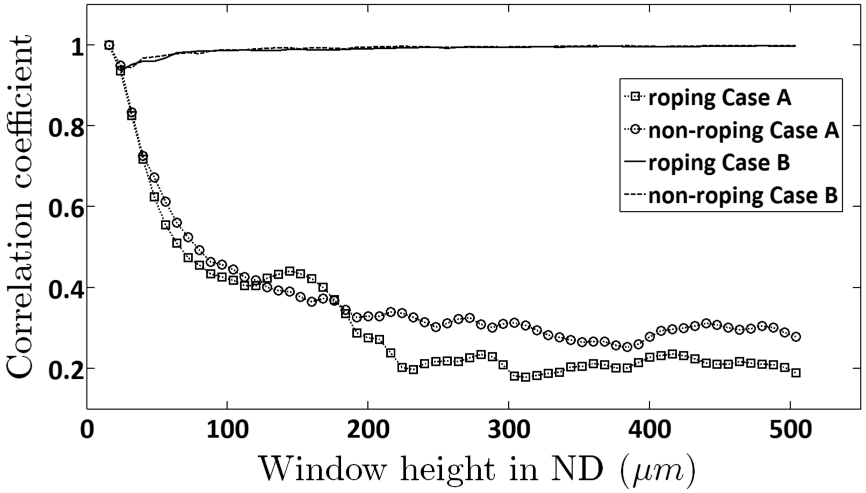

Fig. 3.13: Correlation coefficient between layers of grains with increasing thickness. The window width is $160\mu m$, while the window height increases in ND in the MW simulation. In the legend, Case A indicates that the reference layer is the top mono-grain-layer, whose thickness is fixed to $16\mu m$, whereas Case B represents that thickness of the reference layer increases in ND. Note that all layers of grains investigated in this figure start from the free surface. The horizontal axis is the window height of the other layer.

layer of grains and that of the other layer for both samples. In this figure, the horizontal axis is the window height of the other layer of grains. Two different cases of choosing the reference layer are considered for both samples. In case A, the top mono-grain-layer is chosen as the reference layer; the window height of the other layer increases at a step size of $16\mu m$. It can be seen in Fig. 3.13 that the correlation coefficient decreases when the other layer gets thicker. This indicates that the profile morphology of the other layer is deviating gradually from that of the reference with increasing thickness of the other layer. If this thickness does not exceed $130\mu m$, the correlation coefficient is higher than 0.4 for both samples, implying that moderate correlation exists between the profile of the other layer and that of the reference. It implies that the simulated surface profile/topography based on a layer of grains, e.g. a RD/TD EBSD map, can only partially represent that corresponding to a thickness of $130\mu m$. In case B, the window height of both the reference and the other layer increases, while the other layer has one more mono-grain-layer than the reference. It is interesting to see how addition of such an underneath layer of grains will influence the surface morphology. It can be seen in Fig. 3.13 that the correlation coefficient for case B is basically very high and increases with increasing window height for both samples. This indicates that the probability of modifying the profile morphology by an additional mono-grain-layer decreases with increasing window height.

The correlation coefficient is calculated to check the correspondence between the upper and lower surface profile. It is close to -0.07, indicating that there is no correlation between the two profiles. Therefore, the simulated roping is of the irregular type, which agrees well with the experimental observation [25]. Reversely, this good agreement indicates that roping in AA6xxx alloys is due to the spatial texture distribution at the free surface and subsurface. More specifically, the collective deformation of the first 8 layers of grains from the sheet surface with a specific spatial texture distribution plays the most important role in roping formation.

One drawback of the compact surface roughness parameter R_a is that no morphological information of a surface is involved. Due to the periodic property of roping, it is also important to compare the frequency spectra, besides a good match between the simulated and experimental R_a-values for both samples. A surface profile, either from the MW simulation or from the experimental Wyko surface topography, can be transformed by the FFT into the frequency domain, in which this profile is decomposed into a series of frequency components. These frequency components form a spectrum, which functions as a ‘fingerprint’ with respect to a profile in the spatial domain.

For the roping sample, the FFT spectra of the simulated profile with respect to the window height of $80\mu m$ (see, Fig. 3.10a) and of a Wyko TD-stylus profile (see, Fig. 3.10b) are shown in Fig. 3.14a. It is worth noting that only components corresponding to wavelengths larger than $0.03\mu m$ are considered. It can be seen in Fig. 3.14a that the two FFT spectra are very similar. The correlation coefficient between them is 0.82, indicating a high correlation. It is thus suggested that the simulated profile (see, Fig. 3.10a) significantly reproduces the spectral property of this experimental Wyko TD-stylus profile (see, Fig. 3.10b) for the roping sample. Moreover, it can be seen in Fig. 3.14b that the FFT spectrum of the simulated profile with respect to the window height of $128\mu m$ is very similar to that of a Wyko TD-stylus profile for the non-roping sample. The correlation coefficient between them is 0.80. This high correlation indicates the simulated profile can reproduce the spectral property of an experimental TD-stylus profile to a large extent for the non-roping sample.

For a more statistically relevant investigation, the FFT spectrum of the simulated profile with respect to the window height of $80\mu m$ is compared with all experimental TD-stylus profiles for the roping sample. The correlation coefficient is used to quantify their similarity. Then, the FFT spectrum of the simulated profile with respect to the window height of $128\mu m$ for the non-roping sample is analyzed in the same way. Fig. 3.15 shows the correlation coefficient between the spectra of the simulated profile and those of the experimental TD-stylus profiles along RD for both samples. It can be seen that high correlation coefficients are obtained for both samples, indicating that the finding that the simulated profiles reproduce the spectral properties of experimental TD-stylus profiles to a large extent for both samples is statistically relevant.

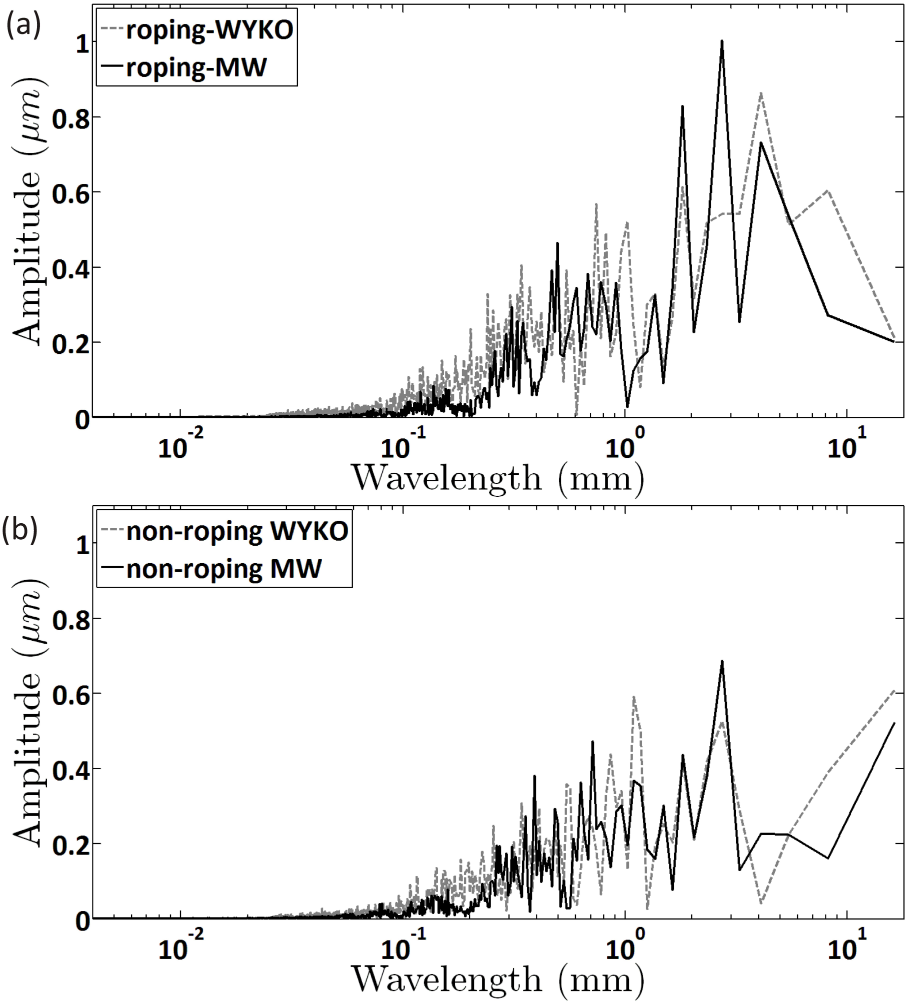

Fig. 3.14: FFT spectrum diagram of the simulated profiles and individual experimental TD-stylus profiles for (a) the roping and (b) non-roping sample. The window height is set to include 8 layers of grains from the free surface for both samples. The window width is $160\mu m$ in the MW simulation.

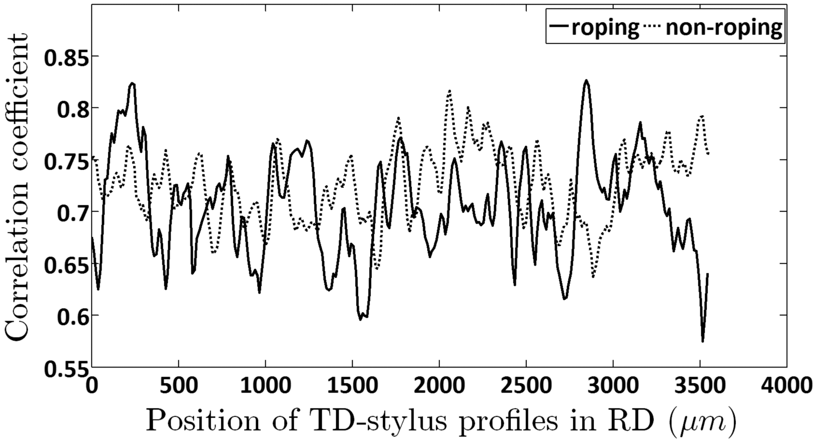

Fig. 3.15: Correlation coefficient between the spectra of the simulated profile and those of the experimental TD-stylus profiles along RD for both samples. In the MW simulation, the window height is set to include 8 layers of grains from the free surface for both samples and the window width is $160\mu m$. Note that the spectral components with wavelengths lower than $0.03\mu m$ are cut off to remove the effect of grain scale fluctuation.

3.6 Conclusions

Two samples with different levels of roughening tendency have been analyzed. Although the EBSD measurement showed that the roping sample features smaller grain size in ND than the non-roping, both samples have approximately 75 layers of grains through the thickness direction. For both samples, large-scale EBSD maps in the TD/ND plane does not reveal any banded distribution of texture, which is believed to be the source of roping.

The mesoscopic MW roping model is successfully extended to surface roughening analysis based on the through thickness microtexture. For a fixed deformation mode, i.e. UT in TD, the MW model use the FC Taylor crystal plasticity code to interpret a local texture within a M-RVE into a r-value. Therefore, the simulated surface profile is solely the consequence of the spatial texture distribution.

Intrinsically, the spatial texture distribution of the roping sample results in a higher probability to roughen than that of the non-roping through layer-wise analysis. A single layer of grains is not sufficient to promote the experimentally observed surface roughness. Therefore, the collective plastic behavior of a number of layers of grains from the free surface is important in roughness formation. However, the spatial texture distribution at the free surface does not penetrate into the bulk. Instead, it changes gradually through the thickness direction. Throughout the entire half thickness of the samples, no spatial texture distribution of a single layer extends to another layer.

For the incremental window height analysis, addition of grain layers underneath the surface will modify the original profile simulated based solely on the top mono-grain-layer. In order to promote the experimental surface roughness, the MW simulation shows that the minimal thickness of the roping sample is $80\mu m$ and $104\mu m$ for the upper and lower surface, respectively, whereas it is $128\mu m$ for both surfaces of the non-roping sample. Therefore, the first 8 layers of grains could be responsible significantly for the roughening formation in both samples. It is further suggested that the grains deeper than those 8 layers would be more constrained by their surrounding matrix.

The simulated surface profile/topography based on a layer of grains can only partially represent a real one. By analyzing the upper and lower surfaces separately, the simulated roping is of the irregular type. This irregular type agrees well with the experimental observation. The spectral analysis further confirms the good agreement between the simulation and the experiment. The FFT spectral correlation study statistically suggests that the simulated surface profiles reproduce the spectral properties of the experimental ones.

Chapter 4

Moving window simulation in other deformation modes

> *"Experience without theory is blind, but theory without experience is mere intellectual play."*
>
> Immanuel Kant

It is generally reported that development of roping or ridging in Al alloys depends on the loading modes. Roping formation is most pronounced after plastic deformation along TD [9, 25, 53, 72]. It is reported by Baczynski *et al.* [25] that roping is appreciably reduced for tensile specimens stretched along RD. Wittridge and Knutsen [46] even claimed that no roping is visible under tensile deformation in RD. So, it is interesting to test the predictive capability of the MW model under UT in RD.

Herein, the MW model is adapted to simulate the surface roughening propensity in other deformation modes. The stress boundary conditions are schematically illustrated in Fig. 2.4. The same conventions are used herein as in Section 2.3.1 for their description. Fig. 4.1 schematically illustrates in the UT reference frame, in which x_1, x_2 and x_3 are tensile direction, width/transverse direction and thickness direction, respectively. Note that texture is not updated in the current MW model since the amount of plastic strain, i.e. $\epsilon^p = 0.15$, is believed to be insufficient to induce obvious texture evolution. Besides, the experimental r-value is rather steady with increasing plastic strain as shown in Fig. A.3. This observation further implies that the trivial texture evolution could be of minor importance.

The strain ratio is defined in Eq. 2.3. Then, the contraction ratio q can be expressed in terms of r-value as:

$$q = \frac{r}{1+r}. \tag{4.1}$$

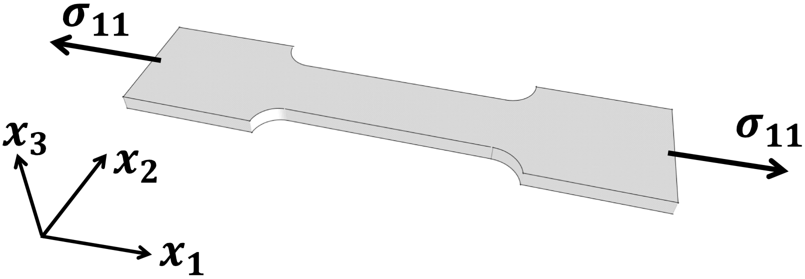

Fig. 4.1: UT reference frame.

4.1 Loading modes and strain compatibilities

Fig. 4.2 schematically illustrates two loading modes for neighboring M-RVEs A and B. It is worth noting that the MW always moves along TD on the experimental surface EBSD maps since the observed orientation bands are parallel with the prior RD. These M-RVEs are uniaxially tensile loaded in TD (see Fig. 4.2a) and in RD (see Fig. 4.2b). The initial dimension before the UT deformation of the M-RVEs is l_0 in RD, w in TD and h_0 in ND. In the MW model, a q-value and a r-value will be simulated for either loading mode.

Then, two strain modes as shown in Fig. 4.3 should be distinguished depending on prescribed strains. It can be seen in Fig. 4.3 that M-RVEs A and B can have different plastic anisotropy under loading if their texture differs. This difference, reflected by that in q-value or r-value between the neighboring M-RVEs, can result in surface roughening. In UT tests, plastic strains in length and width direction, i.e. x_1 and x_2 as shown in Fig 4.1, can be measured experimentally. Either of those experimental plastic strains can be used as a prescribed strain for the MW model. Fig. 4.3a schematically illustrates the strain mode 1, where the plastic strain in TD, ϵ_{TD}, is prescribed in the MW model. Specifically, in this strain mode, $\epsilon^A_{\mathrm{TD}} = \epsilon^B_{\mathrm{TD}} = \epsilon^{prescribed}$. To be more precise, this $\epsilon^{prescribed}$ is a measured macroscopic plastic strain averaged among several UT tests. It can also be seen in Fig. 4.3a that M-RVE A deforms differently in RD and ND from B, i.e. $\epsilon^A_{\mathrm{RD}} \neq \epsilon^B_{\mathrm{RD}}$ and $\epsilon^A_{\mathrm{ND}} \neq \epsilon^B_{\mathrm{ND}}$. Therefore, the surface roughening can be expressed in terms of the difference between h^A and h^B. However, this difference leads to strain incompatibility in RD, i.e. $l^A \neq l^B$ due to volume conservation during plastic deformation. Put differently, plastic contraction difference in RD contributes to the thinning difference of ϵ_{ND}, which in turn results in the surface roughening, if $\epsilon^A_{\mathrm{TD}} = \epsilon^B_{\mathrm{TD}} = \epsilon^{prescribed}$.

In mode 2 as shown in Fig. 4.3b, the plastic strain in RD, ϵ_{RD}, is prescribed in the MW model. More specifically, $\epsilon^A_{\mathrm{RD}} = \epsilon^B_{\mathrm{RD}} = \epsilon^{prescribed}$. It can be seen in Fig. 4.3b that, plastic anisotropy can cause plastic strain differences in both ND and TD, upon plastic deformation. This strain difference in ND, i.e. $\epsilon^A_{\mathrm{ND}} \neq \epsilon^B_{\mathrm{ND}}$, gives rise to surface roughening, i.e. $h^A \neq h^B$, which is compensated by the differential plastic strains in

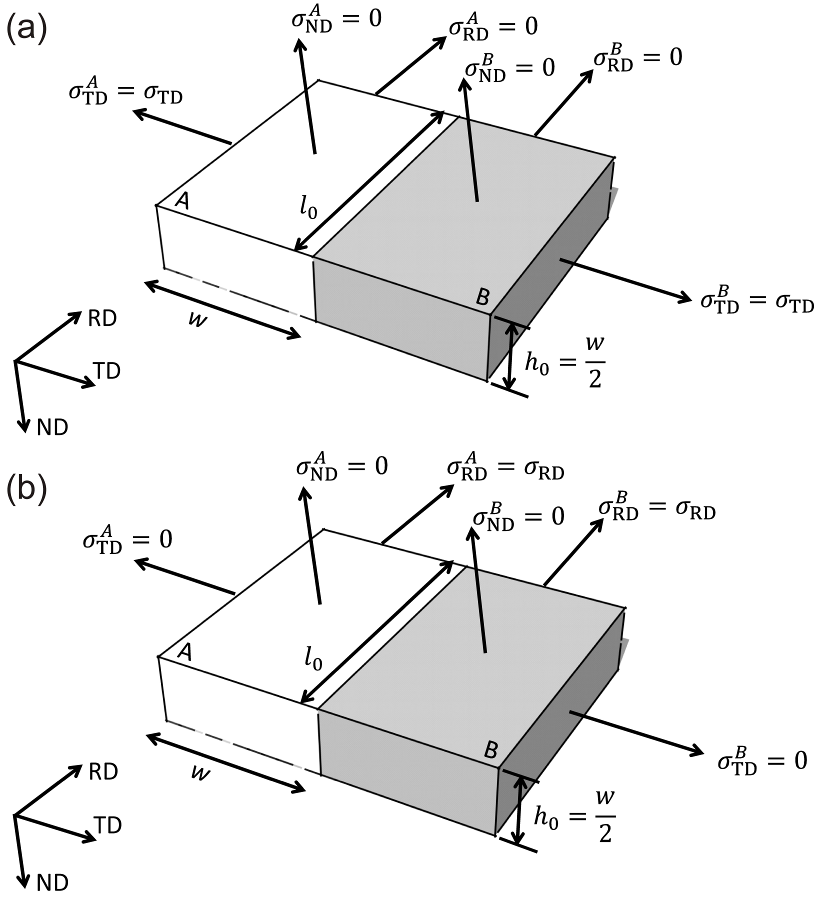

Fig. 4.2: Loading modes. (a) UT in TD: $\sigma_{\mathrm{TD}}^{A} = \sigma_{\mathrm{TD}}^{B} = \sigma_{\mathrm{TD}}$ and $\sigma_{\mathrm{RD}}^{A} = \sigma_{\mathrm{RD}}^{B} = \sigma_{\mathrm{ND}}^{A} = \sigma_{\mathrm{ND}}^{B} = 0$; (b) UT in RD: $\sigma_{\mathrm{RD}}^{A} = \sigma_{\mathrm{RD}}^{B} = \sigma_{\mathrm{RD}}$ and $\sigma_{\mathrm{TD}}^{A} = \sigma_{\mathrm{TD}}^{B} = \sigma_{\mathrm{ND}}^{A} = \sigma_{\mathrm{ND}}^{B} = 0$.

TD between the M-RVEs A and B.

4.1.1 Loading in TD with strain mode 1

The loading geometry with stress boundary conditions and the strain mode 1 with strain boundary conditions are shown in Fig. 4.2a and Fig. 4.3a, respectively. In this case, r_{TD} is simulated by the FC Taylor model since the UT direction is parallel to TD. Additionally, ϵ_{TD} is known:.

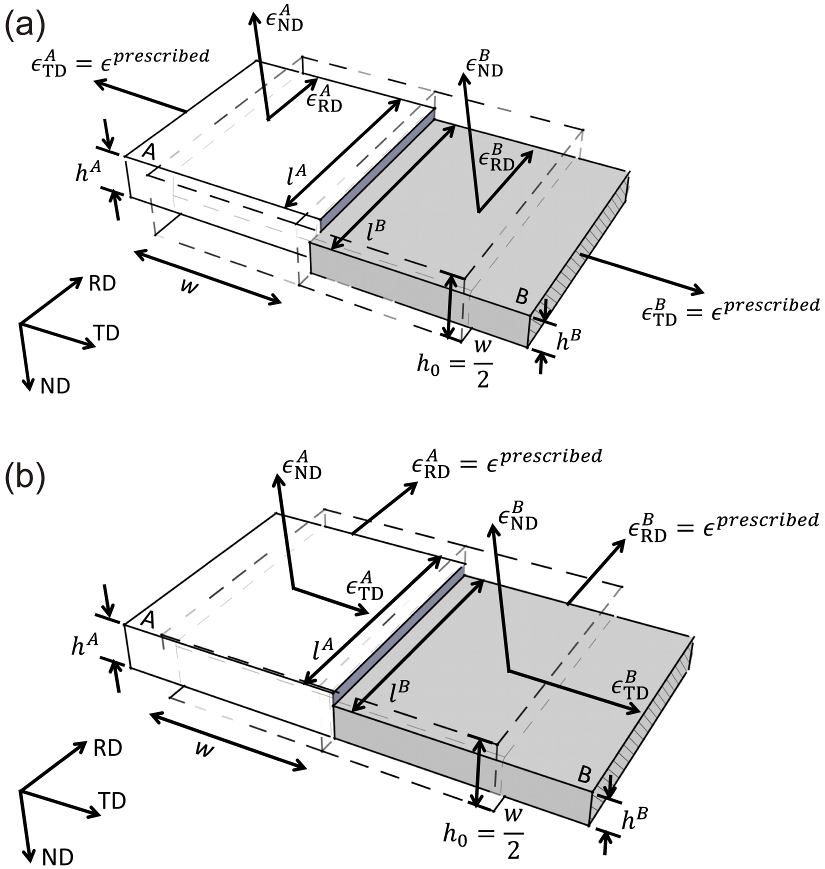

Fig. 4.3: Two strain modes are used for either loading mode to simulate surface profiles. (a) mode 1: $\epsilon^{A}_{\mathrm{TD}} = \epsilon^{B}_{\mathrm{TD}} = \epsilon^{prescribed}_{\mathrm{TD}}$; (b) mode 2: $\epsilon^{A}_{\mathrm{RD}} = \epsilon^{B}_{\mathrm{RD}} = \epsilon^{prescribed}_{\mathrm{RD}}$.

$$\epsilon_{\mathrm{TD}} = \epsilon_{\mathrm{TD}}^{prescribed}. \tag{4.2}$$

In the frame of a typical rolling process, r_{TD} can be expressed as:

$$r_{\mathrm{TD}} = \frac{\epsilon_w}{\epsilon_t} = \frac{\epsilon_{\mathrm{RD}}}{\epsilon_{\mathrm{ND}}}. \tag{4.3}$$

In this, ϵ_{RD} is the logarithmic plastic strain in the width direction, ϵ_w, and ϵ_{ND} the logarithmic plastic strain in the thickness direction, ϵ_t.

During the plastic deformation, the volume is assumed to be constant:

$$\epsilon_{\mathrm{RD}} + \epsilon_{\mathrm{TD}} + \epsilon_{\mathrm{ND}} = 0, \tag{4.4}$$

where ϵ_{TD} is the plastic strain in TD (tensile direction).
Combining Eq. 4.3 with Eq. 4.4 leads to:

$$\epsilon_{\mathrm{ND}} = -\frac{\epsilon_{\mathrm{TD}}}{1 + r_{\mathrm{TD}}}. \tag{4.5}$$

Plugging Eq. 4.2 into Eq. 4.5 results in:

$$\epsilon_{\mathrm{ND}} = -\frac{\epsilon_{\mathrm{TD}}^{prescribed}}{1 + r_{\mathrm{TD}}}. \tag{4.6}$$

According to the definition of true strain, we have

$$\epsilon_{\mathrm{ND}} = \ln(1 + e_{\mathrm{ND}}), \tag{4.7}$$

where e_{ND} is the engineering strain in ND. Combining Eq. 4.7 with Eq. 4.6 results in:

$$e_{\mathrm{ND}} = \exp(-\frac{\epsilon_{\mathrm{TD}}^{prescribed}}{1 + r_{TD}}) - 1. \tag{4.8}$$

Let Δh be the thickness change and h_0 be the original thickness of a M-RVE of the MW model. Then the engineering strain in ND can also be expressed as follows:

$$e_{\mathrm{ND}} = \frac{\Delta h}{h_0}. \tag{4.9}$$

Combining Eq. 4.8 and Eq. 4.9 gives rise to:

$$\Delta h = h_0 \left(\exp(-\frac{\epsilon_{\mathrm{TD}}^{prescribed}}{1 + r_{\mathrm{TD}}}) - 1 \right) \tag{4.10}$$

4.1.2 Loading in TD with strain mode 2

The loading geometry with stress boundary conditions and the strain mode 2 with strain boundary conditions are shown in Fig. 4.2a and Fig. 4.3b, respectively. In this case, q_{TD} is simulated by the FC Taylor model as the UT direction is parallel to TD. It is worth noting that simulating q_{TD} is equivalent to simulating r_{TD} due to Eq. 2.3. As illustrated in Fig. 4.3b, ϵ_{RD} is known:

$$\epsilon_{\mathrm{RD}} = \epsilon_{\mathrm{RD}}^{prescribed}. \tag{4.11}$$

In the sample framework of typical rolled sheets, q_{TD} can be expressed as:

$$q_{\mathrm{TD}} = -\frac{\epsilon_w}{\epsilon_l} = -\frac{\epsilon_{\mathrm{RD}}}{\epsilon_{\mathrm{TD}}}. \tag{4.12}$$

In this, ϵ_{RD} is the logarithmic plastic strain in the width direction, ϵ_w, and ϵ_{TD} the logarithmic plastic strain in the axial direction, ϵ_l.

During the plastic deformation, the volume conservation is assumed as expressed in Eq. 4.4.

Combining Eq. 4.12 with Eq. 4.4 leads to:

$$\epsilon_{\mathrm{ND}} = \epsilon_{\mathrm{RD}} \left(\frac{1}{q_{\mathrm{TD}}} - 1 \right). \tag{4.13}$$

Plugging Eq. 4.11 into Eq. 4.13 results in:

$$\epsilon_{\mathrm{ND}} = \epsilon_{\mathrm{RD}}^{prescribed} \left(\frac{1}{q_{\mathrm{TD}}} - 1 \right). \tag{4.14}$$

Combining Eq. 4.7 with Eq. 4.14, the engineering strain in ND e_{ND} can be expressed as:

$$e_{\mathrm{ND}} = \exp(\epsilon_{\mathrm{RD}}^{prescribed} \left(\frac{1}{q_{\mathrm{TD}}} - 1 \right)) - 1. \tag{4.15}$$

Combining Eq. 4.15 and Eq. 4.9 gives rise to:

$$\Delta h = h_0 \left(\exp(\epsilon_{\mathrm{RD}}^{prescribed} \left(\frac{1}{q_{\mathrm{TD}}} - 1 \right)) - 1 \right). \tag{4.16}$$

4.1.3 Loading in RD with strain mode 1

The loading geometry with stress boundary conditions and the strain mode 1 with strain boundary conditions are shown in Fig. 4.2b and Fig. 4.3a, respectively. In this case, q_{RD} is simulated by the FC Taylor model since the UT direction is parallel to RD. Additionally, ϵ_{TD} is known as in Eq. 4.2.

In the sample framework of typical rolled sheets, q_{RD} can be expressed as:

$$q_{\mathrm{RD}} = -\frac{\epsilon_w}{\epsilon_l} = -\frac{\epsilon_{\mathrm{TD}}}{\epsilon_{\mathrm{RD}}}. \tag{4.17}$$

In this, ϵ_{TD} is the logarithmic plastic strain in the width direction, ϵ_w, and ϵ_{RD} the logarithmic plastic strain in the axial direction, ϵ_l.

During the plastic deformation, the volume conservation is assumed as expressed in Eq. 4.4.

Combining Eq. 4.17 with Eq. 4.4 leads to:

$$\epsilon_{\mathrm{ND}} = \epsilon_{\mathrm{TD}} \left(\frac{1}{q_{\mathrm{RD}}} - 1 \right). \tag{4.18}$$

Plugging Eq. 4.2 into Eq. 4.18 results in:

$$\epsilon_{\mathrm{ND}} = \epsilon_{\mathrm{TD}}^{prescribed} \left(\frac{1}{q_{\mathrm{RD}}} - 1 \right). \tag{4.19}$$

Combining Eq. 4.7 with Eq. 4.19, the engineering strain in ND e_{ND} can be expressed as:

$$e_{\mathrm{ND}} = \exp(\epsilon_{\mathrm{TD}}^{prescribed} \left(\frac{1}{q_{\mathrm{RD}}} - 1 \right)) - 1. \tag{4.20}$$

Combining Eq. 4.20 and Eq. 4.9 gives rise to:

$$\Delta h = h_0 \left(\exp(\epsilon_{\mathrm{TD}}^{prescribed} \left(\frac{1}{q_{\mathrm{RD}}} - 1 \right)) - 1 \right). \tag{4.21}$$

4.1.4 Loading in RD with strain mode 2

The loading geometry with stress boundary conditions and the strain mode 2 with strain boundary conditions are shown in Fig. 4.2b and Fig. 4.3b, respectively. In this case, r_{RD} is simulated by the FC Taylor model since the UT direction is parallel to RD. Additionally, ϵ_{RD} is known as in Eq. 4.11.

In the sample framework of typical rolled sheets, r_{RD} can be expressed as:

$$r_{\mathrm{RD}} = \frac{\epsilon_w}{\epsilon_t} = \frac{\epsilon_{\mathrm{TD}}}{\epsilon_{\mathrm{ND}}}. \tag{4.22}$$

In this, ϵ_{TD} is the logarithmic plastic strain in the width direction, ϵ_w, and ϵ_{ND} the logarithmic plastic strain in the thickness direction, ϵ_t.

During the plastic deformation, the volume conservation is assumed as expressed in Eq. 4.4.

Combining Eq. 4.22 with Eq. 4.4 leads to:

$$\epsilon_{\mathrm{ND}} = -\frac{\epsilon_{\mathrm{RD}}}{1 + r_{\mathrm{RD}}}. \tag{4.23}$$

Plugging Eq. 4.11 into Eq. 4.23 results in:

$$\epsilon_{\mathrm{ND}} = -\frac{\epsilon_{\mathrm{RD}}^{prescribed}}{1 + r_{\mathrm{RD}}}. \tag{4.24}$$

Combining Eq. 4.7 with Eq. 4.24 results in:

$$e_{\mathrm{ND}} = \exp(-\frac{\epsilon_{\mathrm{RD}}^{prescribed}}{1 + r_{\mathrm{RD}}}) - 1. \tag{4.25}$$

Combining Eq. 4.8 and Eq. 4.9 gives rise to:

$$\Delta h = h_0 \left(\exp(-\frac{\epsilon_{\mathrm{RD}}^{prescribed}}{1 + r_{\mathrm{RD}}}) - 1 \right). \tag{4.26}$$

4.2 Results and discussions

The results of the MW simulations using different loading and straining modes as shown in Figs. 4.2 and 4.3 are discussed in this section. The input EBSD maps of the roping and non-roping samples are shown in Fig. 2.5. So, the same surface EBSD maps as used in Chapter 2 are studied. It is worth noting that all the surface EBSD maps are aligned with their horizontal and vertical axises parallel to TD and RD, respectively. Their dimension in TD is greater than that in RD in order to reveal more texture bands along RD.

Three UT loading directions, viz. TD, RD and 45° from RD, are studied. Fig. 4.4 shows the r-value profiles simulated under these three loading directions for both samples. It is worth noting that r-value simulation using a FC Taylor model depends only on the loading direction for a given texture. It can be seen in Fig. 4.4 that the hypothetical r-value profiles vary with UT loading directions for either sample. This observation is due to plastic anisotropy. Since r-value represents strain thinning property of metal sheets, a hypothetical r-value profile can serve as a preliminary estimate of roping propensity. The higher the r-value variation is, the higher probability of inducing roping the microstructure has. It can be seen in Fig. 4.4a that the roping sample exhibits the highest roping propensity when loading in TD. Moreover, the roping propensity of the roping sample decreases when loading in the other two directions.

This is confirmed by R_a-values of the r-value profiles for the roping sample (see, e.g. Fig. 4.4a) as shown in Table 4.1. On the contrary, the non-roping sample yields the lowest roughening tendency when loading in TD as shown in Fig. 4.4b and Table 4.1. These observations imply that the loading modes will influence the roping propensity due to plastic anisotropy. It can also be seen in Fig. 4.4 and Table 4.1 by comparing the two samples that the roping sample always shows higher roping propensity than the non-roping no matter along which direction the sample is loaded. This finding indicates that the local texture variation in the microstructure of the roping sample intrinsically leads to higher roping propensity than that in the non-roping sample for all loading directions.

It should be stressed that the observations that roping sample exhibits higher roping propensity than the non-roping no matter on which direction the sample is loaded and that the roping sample exhibits the highest roping propensity when loading in TD agree well with experimental observations. This implies the predictive capability of the MW model in the roping analysis.

It can be seen in Fig. 4.4a that TD is macroscopically the most strain thinning resistant direction for the roping sample. However, RD is macroscopically the most strain thinning resistant direction for the non-roping sample as shown in Fig. 4.4b. It can be further seen in Fig. 4.4 that the direction, which is 45° from RD, features the lowest strain thinning resistance for both samples. By comparing with Table A.1, it can be observed that the general trend that the simulated macroscopic stain thinning resistance changes with loading directions is in accordance with that measured experimentally. Put differently, the macroscopic strain thinning properties, represented by means of each r-value profile as shown in Fig. 4.4, agree qualitatively with the experimental r-values listed in Table A.1 for both samples. However, the quantitative agreement between simulation and experiment cannot be reached due to the fact FC Taylor model may not give accurate r-value prediction [128–131] and the amount of grains considered is insufficient to be statistically relevant. Besides, the texture gradient through the thickness direction may exist as shown in Fig. B.10. This would add additional inaccuracy to r-value prediction. Furthermore, the grain shape can also influence r-value, which has been shown both experimentally [132] and numerically [109, 132]. Therefore, better agreement can be achieved by using advanced crystal plasticity models, i.e. advanced LAMEL (ALAMEL), VPSC or CPFEM model, with sufficient grain statistics.

Although the roping propensity can be evaluated in terms of r-value profiles as shown in Fig. 4.4, the surface profile with amplitude and wavelength cannot be simulated unless further strain boundary conditions (see, e.g. Fig. 4.3) are considered. The results concerning surface profile simulations will be given in the Sections 4.2.1 and 4.2.2.

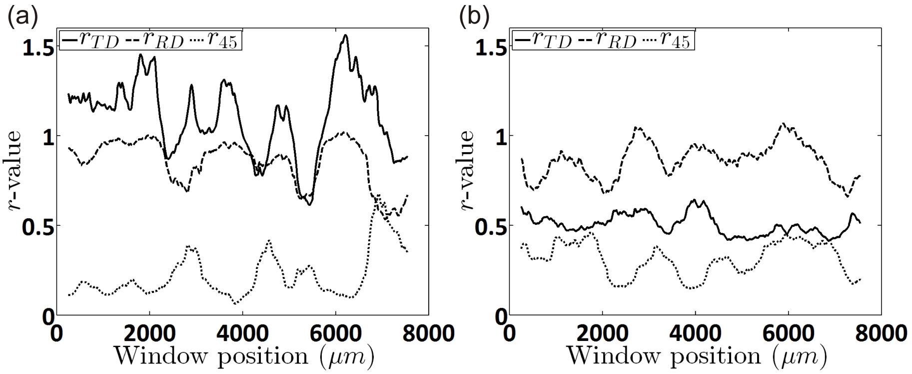

Fig. 4.4: r-value profiles simulated under UT loading in TD, RD and 45° from RD for the (a) roping and (b) non-roping sample. The window size in TD used in these MW simulations is 504 μm.

Table 4.1: Summary of arithmetic average roughness, R_a, of r-value profiles of both samples using window width of 504 μm in the MW simulation.

sample	${R_a}^{r_{\mathbf{RD}}}$[1]	${R_a}^{r_{45}}$	${R_a}^{r_{\mathbf{TD}}}$
Roping	0.105	0.103	0.168
Non-roping	0.079	0.077	0.046

[1] ${R_a}^r = \frac{1}{N}\sum_{i=1}^{N}|r_i - \overline{r}|$, where r_i is r-value of M-RVE i, $\overline{r}$ the average r-value of all M-RVEs and N the total number of the M-RVE.

4.2.1 Moving window simulation under UT loading in TD

To simulate a surface profile by the MW model, a strain mode (see, e.g. Fig. 4.3) needs to be assumed in addition to a loading mode (see, e.g. Fig. 4.2). It is experimentally reported that UT loading in TD yields the highest roping intensity among all directions [9, 25]. Therefore, UT in TD is the most interesting loading mode with respect to roping analysis. Two strain modes are considered under this loading mode.

Fig. 4.5 shows the effect of strain modes under TD loading on simulated surface profiles by the MW model. It can be clearly seen that strain mode 2, in which the plastic strain in the width direction, $\epsilon_w = \epsilon_{\mathrm{RD}}$, is prescribed, leads to higher surface roughening for both samples. This observation implies that variation in plastic strain along TD produce higher surface fluctuation. Note that both strain modes yield similar surface morphology. That is to say, positions of peaks and valleys are the same for both strain modes when loading in TD. It is worth noting that strain mode 1 is implemented for all the MW simulation results based on UT loading in TD, unless

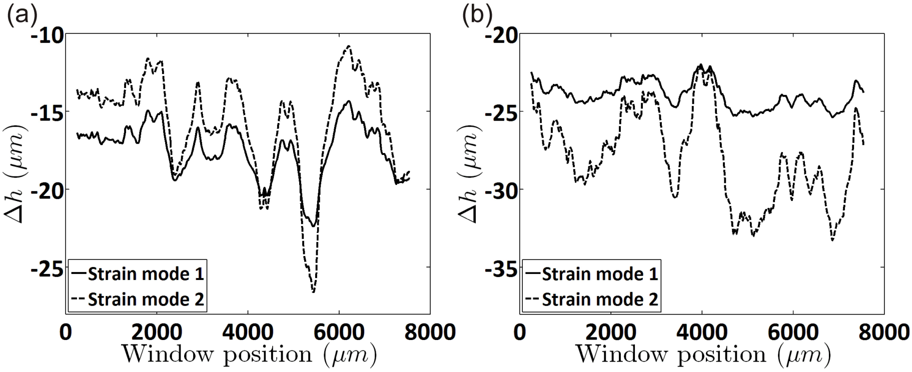

Fig. 4.5: Surface profiles simulated under UT loading in TD for the (a) roping and (b) non-roping sample. The window size in TD used in these MW simulations is $504\mu m$.

explicitly stated otherwise.

4.2.2 Moving window simulation under UT loading in RD

These two strain modes as show in Fig. 4.3 are also considered under RD loading mode. Fig. 4.6 shows the effect of strain modes under RD loading on simulated surface profiles by the MW model. It can be seen that strain mode 1, in which the plastic strain in the width direction, $\epsilon_w = \epsilon_{\text{TD}}$, is prescribed, leads to higher surface roughening for both samples. Similar to TD loading mode as show in Fig. 4.5, confining ϵ_w to be the same for all M-RVEs, which allows plastic strain in the TA to vary, results in higher surface roughness. However, if plastic strain in RD is prescribed to be the same for all M-RVEs, the surface roughening is reduced. Note also that positions of peaks and valleys are the same for both strain modes when loading in RD.

Experimental observations basically show that UT loading in RD leads to reduced roping or even no roping for the same sample which suffers from severe roping when loading in TD. This therefore suggests that strain mode 2, where $\epsilon_{\text{RD}} = \epsilon^{prescribed}$ for all M-RVEs, should be realistic. In other words, strain mode 2 promotes roping when loading in TD but suppresses it in the UT-RD loading mode for both samples. It should be reminded that the strain mode 2 would allow plastic strain heterogeneity in TD which thereupon gives rise to plastic heterogeneity in ND. It is thus recommended to use strain mode 2 for roping analysis. However, this requires further experimental validation, which can be done as future work.

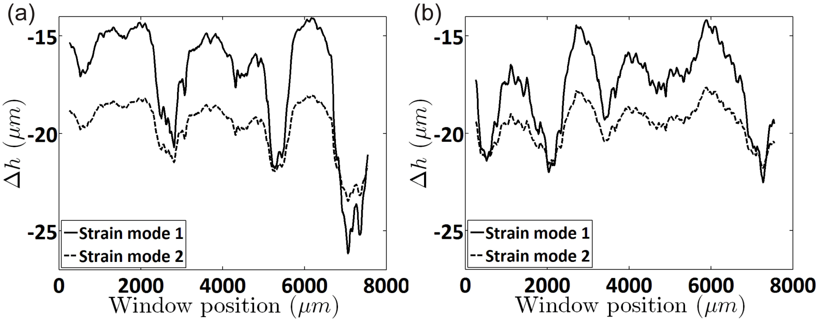

Fig. 4.6: Surface profiles simulated under UT loading in RD for the (a) roping and (b) non-roping sample. The window size in TD used in these MW simulations is 504 μm.

4.3 Conclusions

The predictive capability of the MW model under UT in different directions has been tested. It is shown by the MW simulation that the loading modes influence the roping propensity due to plastic anisotropy. The predicted roping tendency under UT in RD, TD and 45° to RD agrees qualitatively well with the reported experimental observations. This, therefore, indicates the predictive capability of the MW model in the roping analysis.

Besides the loading mode, the way one prescribes the strain influences the model prediction. It is found that prescribing ϵ_w promotes surface roughening under the assumption that the plastic flow varies in the TA to produce strain fluctuation in ND for the M-RVEs. This assumption needs experimental verification to help a critical user to choose between strain mode 1 or 2. Nevertheless, both strain modes yield the same roughness morphology, implying their capability of capturing the most important feature of roping, i.e. λ.

Chapter 5

Contribution factor: a parameter quantifying the role of an orientation in roping or ridging

"Simplicity is the ultimate sophistication."
Leonardo da Vinci

5.1 Introduction

It has been demonstrated by Engler [133] that texture control can be applied during industrial processing of Al alloy sheets in order to improve their plastic property through fine-tuning the thermomechanical parameters related to rolling and recrystallization processes. Specifically, texture control can be used to improve the deep drawability [134] and to reduce surface roughening due to heterogeneous plastic straining [120]. Roping or ridging as a result of heterogeneous plastic deformation is basically attributed to the occurrence of the meso-scale banding of grains with similar orientations. In order to eliminate roping or ridging effectively and efficiently by fine-tuning the pertained thermomechanical parameters, one should first know which orientations are its major contributors. Different texture components present in these bands were claimed to be the predominant cause of a roping profile. However, it is difficult to assess the 'sensitivity' of roping tendency to the strength of a particular texture component. In this work, a "contribution factor" is proposed to just do that. An AA6016 sample was studied as an example. The CG-$\{021\}\langle100\rangle$, Goss-$\{011\}\langle100\rangle$, CH-$\{001\}\langle120\rangle$ and Q-$\{013\}\langle231\rangle$ were found to be the predominant texture components which according to this method contributed to the roping profile.

Texture forms during grain growth or deformation and is modified during recrystallization or phase transformation and theories exist to predict its origin [135]. Texture formation and evolution during thermomechanical processes of aluminum alloys have been investigated extensively [63, 136], leading to theories explaining origins of specific texture components. For example, P-$\{011\}\langle122\rangle$ orientation results from particle stimulated nucleation (PSN) during annealing [137] and H-$\{001\}\langle110\rangle$ orientation is caused by shear deformation [138, 139], *etc.* From a metallurgical point of view, these theories can, in turn, be used to guide industrial practice to reduce roping if the predominant texture components contributing to roping can be derived.

Thanks to the rapid development of the automated EBSD technique, clustering of similarly orientated grains, i.e., orientation banding, has been found by several research groups [10, 45, 63, 70, 96, 140]. Furthermore, much effort has been made to correlate the spatial distribution of grains, which belong to a specific texture component, with roping. Then, the band-like distribution of grains with cube-$\{001\}\langle100\rangle$ orientation [44, 45] as well as Goss [25, 73], R-$\{124\}\langle211\rangle$ [46], X-$\{112\}\langle110\rangle$ [72] and combinations of Goss-cube [89, 140, 141] and X-cube-Goss orientations [72] was reported to be the predominant cause of roping.

It, however, turned out to be difficult to correlate this type of patterning with the valleys or ridges of the roping profile. The distances between the bands with high densities of cube or Goss orientation, were found to be similar to those separating the "ridges" of the roping profile [9, 25, 44, 45, 54, 89, 140]. Therefore, various attempts have been done to simulate the roping or ridging profiles by means of micromechanical models [9, 23, 24, 49, 72, 73, 96]. One of them is the MW method [99] by the present authors. It makes use of an intermediate mesoscopic length scale, between those of the grains and the entire sample (see, e.g. Chapter 2). However, the feeling of how important the effect of a particular texture component is, with respect to roping or ridging, is lost when one exclusively uses such complex models. It is the purpose of the present chapter to present for each texture component a "contribution factor" that would give the researcher an idea how much a particular texture component 'contributes' to the roping tendency, so that one may estimate whether or not an increase or decrease of this texture component would have a positive or negative effect on the roping tendency. In other words, this "contribution factor" characterizes the 'sensitivity' of the roping tendency to the strength of a texture component.

5.2 Methodology

5.2.1 Plastic behavior of ideal crystal orientations

It is reported by different research groups that band-like local distributions of grains with cube orientation [44, 45, 88], as well as R [46], X [72], and alternating cube and Goss orientations [25, 54, 70, 89] have been observed. Thus, it is necessary to analyze their plastic behavior upon loading. The first attempt was to investigate the plastic behavior of ideal crystal orientations, which are commonly observation in Al alloys.

Due to the plastic anisotropy of single crystals, different texture components can have differing plastic responses. The r-value was simulated for a set of ideal texture components. The typical ideal texture components [142–145] in cold rolled and recrystallized aluminum alloys were generated by the MTM-FHM software system. These texture components were created at particular points, whose Miller indices are given in the second column in Table 5.1, in the Euler space with a Gaussian distribution of 16.5°. The orthorhombic sample symmetry was imposed when generating these ideal components, which therefore include all possible texture variants [33, 146] for each component. The r-values were simulated by a FC Taylor model for the UT tests at 0°, 45° and 90° to RD and are listed in Table 5.1. Note that the methodology of r-value simulation has been described in Section 2.3.1.

5.2.2 Contribution factor

Large-scale EBSD orientation maps are used as input to analyze the spatial distribution of grains belonging to a specific texture component, g, with the help of the MW method [99, 110]. This method is primarily used to predict the roping or ridging profile of a sample (see e.g. Fig. 5.1 (c)) [99]. However, it also provides results about the patterning of texture components (see e.g. Fig. 5.1b). A schematic illustration of this MW method is shown in Fig. 5.2. The window extends over the entire RD length of an EBSD map and its width is w in the the transverse direction (TD). Each window includes a mesoscopic volume of grains, the texture of which is obtained by transforming discrete orientation data into an orientation distribution function (ODF). Then the volume fraction of a texture component can be calculated by the MTM-FHM software system[102] using a convolution method[104]. This particular calculation is not required for simulating the roping or ridging profile, but it is useful for finding the “contribution factor”, which is the subject of the present chapter. By scanning the window along TD, the spatial distribution of volume fraction of this texture component, v_g, can be obtained. v_g is a function of the distance x of the window centre from the left side of the EBSD map (see, e.g. Fig. 5.1 (b)).

A surface roping profile can either be measured or simulated on the same region where the analysis of the spatial distribution of volume fraction has been done. In the present study, the roping profiles are simulated by this meso-scale MW model based

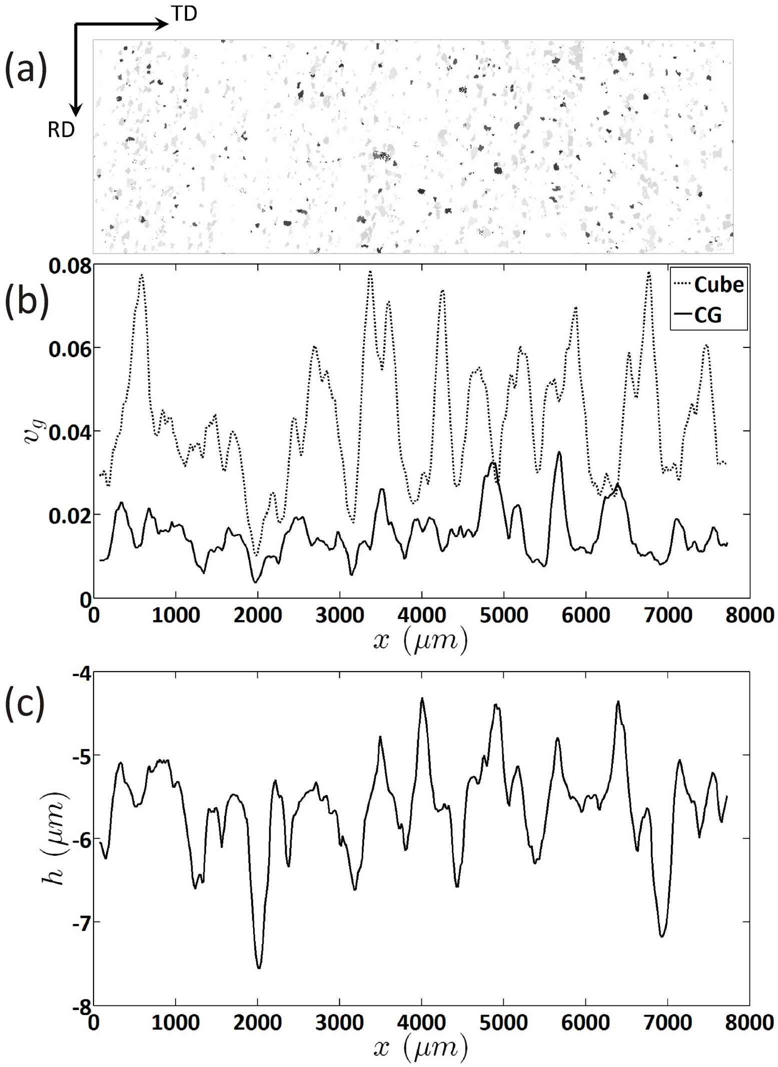

Fig. 5.1: Contribution factor η_g for an experimental EBSD map: (a) EBSD map with only grains within 7° of exact cube (in grey) and CG (in black) component; (b) spatial distribution of volume fraction v_g of cube and CG component calculated using the MW method; (c) simulated surface profile h using the meso-scale MW model by assuming $\epsilon_{\mathrm{TD}} = 0.15$. Note that the window width w in TD for both (b) and (c) is $150\mu m$. The orientation map in (a) is on the same scale with the x-coordinate in (b) and (c).

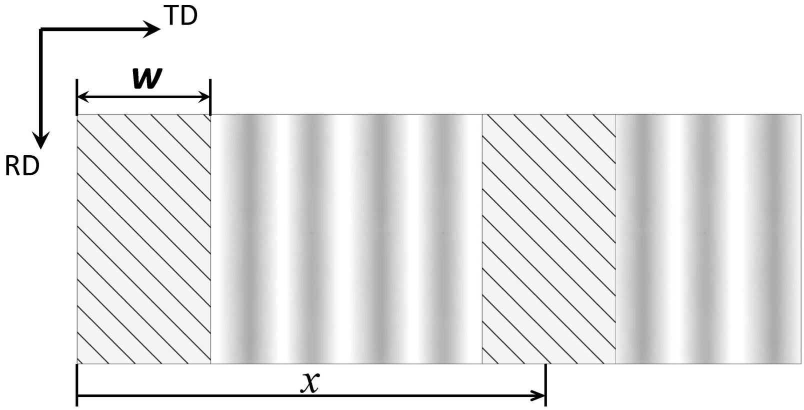

Fig. 5.2: Schematic illustration of the MW method: a window represented by the hatched rectangle (to the left) is placed on top of an EBSD orientation map, whose spatial distribution of orientations shows band-like feature along RD. This window, which moves along TD at a certain step size to a new position x, extends over the entire RD length of the EBSD map. Its width is w in TD.

on both artificial and experimental EBSD maps [99]. Herein, these roping profiles are described in terms of surface height, h, as a function of x (see, e.g. Fig. 5.1 (c)).

It is generally accepted that roping is caused by inhomogeneity of texture and its associated plastic anisotropy [9, 10, 23–25, 45, 46, 48, 54, 70, 72, 73, 89, 96, 140], when segregation of secondary phase particles were precluded [22]. In the first instance, it is natural to examine the association between v_g with h. This would provide information on how v_g correlates with h. Statistically, h and v_g can be considered as two random variables [126]. For each position x along TD of the sample surface (see, e.g. Fig. 5.2) on which the MW is positioned, there is a pair of values of h and v_g. g is merely an 'index': if n texture components g are considered, then there are n different random variables v_g. Their correlation coefficient [126] can be defined by:

$$\rho_{hv_g} = \frac{cov(h, v_g)}{S_h S_{v_g}} \tag{5.1}$$

where ρ_{hv_g} is the correlation coefficient, cov the covariance, and S_h and S_{v_g} the sample standard deviation of h and v_g, respectively. ρ_{hv_g} is a measure of the linear interdependence of h and v_g in the sense that its value is a measure of accuracy with which h can be approximated by a linear function of v_g [125, 126]. The value of ρ_{hv_g} always lies between -1 and 1. If $\rho_{hv_g} = 0$, there is no linear association between h and v_g. $\rho_{hv_g} = 1$ indicates h and v_g are positively perfectly correlated, whereas $\rho_{hv_g} = -1$ indicates they are negatively perfectly correlated. The greater $|\rho_{hv_g}|$ is, the stronger the association between h and v_g is [127].

An important feature of the correlation coefficient is that it is dimensionless and independent of the origin, i.e. for any constants a_1, a_2, b_1 and b_2 with $a_1 > 0$ and $a_2 > 0$, $r(a_1X + b_1, a_2Y + b_2) = r(X, Y)$, if X, Y are two random variables [125]. This feature makes ρ_{hv_g} insensitive to the amplitude of the fluctuation of v_g. However, it is reasonable to assume that a higher fluctuation of v_g leads to higher roping propensity. This fluctuation is characterized by the standard deviation, S_{v_g}. For a specific g, assume the sample size of v_g, i.e. the number of the considered MW positions, is n; then its standard deviation, according to Ref. [125, 126], writes:

$$S_{v_g} = \sqrt{\frac{\sum\limits_{1=1}^{n} (v_{g_i} - \bar{v_g})^2}{n-1}}. \tag{5.2}$$

In this, v_{g_i} is the ith observation of the value of the random variable v_g, when the MW scans through the entire sample. It is a measure of dispersion of v_{g_i} about its sample mean, $\bar{v_g}$, over the entire sample. It is the length scale of the entire sample that is accessed by letting i run from 1 to n. Therefore, a greater S_{v_g} indicates a higher fluctuation of v_g, presumably leading to a greater contribution to a roping profile, h.

In addition to texture inhomogeneity, plastic anisotropy should also be considered. Let δ_g be:

$$\delta_g = |e_g - \bar{e}|, \tag{5.3}$$

where, e_g and $\bar{e}$ are the engineering plastic strain in ND of an imaginary compact volume consisting solely of the grains with the orientation g and of all grains of the sample on which EBSD is measured, respectively. They are simulated by iteratively seeking the minimal plastic power dissipation per unit volume using the FC Taylor model [107] for a uniaxial plastic deformation of 0.15 along TD, (i.e. $\epsilon_{\mathrm{TD}} = 0.15$), which is the most commonly used deformation mode to test roping for Al alloys [49]. δ_g characterizes how differently g would deform in ND as compared to the average Al sheet, if neighbouring grains interaction is not considered. Plastically, a greater $\delta(g)$ leads to higher surface roughening propensity.

Finally, taking all aforementioned factors (viz. Eqs. (5.1)-(5.3)) into account, the contribution factor of an orientation, or a texture component, g, to a roping profile, h, can be defined as:

$$\eta_g = \rho_{hv_g} S_{v_g} \delta_g. \tag{5.4}$$

5.3 Results and Discussions

5.3.1 Ideal orientation anisotropy analysis

The simulated r-values for ideal texture components in three different directions in the surface plane are shown in Table 5.1. All the ideal texture components show different r-values in different loading directions. It means that all the ideal texture components

Table 5.1: Volume fractions of the typical texture components in cold rolled and recrystallized AA6016-T4 aluminum alloys for the roping and non-roping samples and simulated r-values for each texture components in three directions.

Texture component	Index notation	Volume fraction (%)		Simulated r-value		
	$\{hkl\}\langle uvw\rangle$	Roping	Non-roping	r_{RD}	r_{45}	r_{TD}
cube	$\{001\}\langle 100\rangle$	17.9	12.2	1.00	0.00	1.00
Goss	$\{011\}\langle 100\rangle$	5.1	1.9	1.00	0.40	$+\infty$
S	$\{123\}\langle 634\rangle$	16.4	16.2	0.67	5.80	0.49
CG	$\{021\}\langle 100\rangle$	16.1	8.9	1.00	0.14	6.89
CH	$\{001\}\langle 120\rangle$	11.5	14.3	0.15	0.36	0.15
Dillamore	$\{4\,4\,11\}\langle 11\,11\,8\rangle$	7.5	10.1	0.30	3.26	0.05
Brass	$\{011\}\langle 211\rangle$	6.9	5.2	0.27	7.93	1.00
Copper	$\{112\}\langle 111\rangle$	7.1	8.3	1.00	5.99	0.11
H	$\{001\}\langle 110\rangle$	2.8	4.3	0.00	1.00	0.00
P	$\{011\}\langle 122\rangle$	5.0	7.7	8.26	1.06	0.31
R	$\{124\}\langle 211\rangle$	17.7	21.2	0.41	2.21	0.35
X	$\{112\}\langle 110\rangle$	4.2	2.9	0.11	6.00	1.00
Q	$\{013\}\langle 231\rangle$	13.4	20.5	0.18	1.01	0.11
Random				1.00	1.00	1.00

are plastically anisotropic with respect to the loading directions considered, whereas the cube component is plastically isotropic when loading in the RD or TD. Under such circumstances, the cube component is equivalent to the random texture in terms of r-value.

The texture components, such as Goss and H, show significantly different r-values in different loading directions (see Table 5.1). The Goss orientation is extremely resistant to strain thinning in UT-TD with $r_{\mathrm{TD}} = +\infty$, while its r-value is 1.0 and 0.4 in UT-RD and UT-45, respectively. In contrast, the H orientation is extremely susceptible to strain thinning in both UT-TD and UT-RD with $r_{\mathrm{TD}} = r_{\mathrm{RD}} = 0$, whereas $r_{45} = 1$. Therefore, an orientation can be resistant to thinning when loading in one direction but susceptible to it in another direction.

For UT-TD, Goss and CG are the thinning resistant texture components, whereas all others except cube and X are susceptible to thinning, as shown in Table 5.1. However, P is the only orientation with an r-value higher than that of the random texture in UT-RD. The r-value difference between the most thinning resistant texture component and the most thinning susceptible for UT-TD is larger than that for UT-RD. Additionally, the probability of the PSN related P component occurring is rather low in the T4 state, as shown in Table 5.1. Therefore, UT-TD has a higher probability of producing surface roughness compared to UT-RD.

5.3.2 Contribution factor analysis

The method is first demonstrated on numerically generated virtual EBSD orientation maps with alternating equal bands of R/cube, cube/Goss, CG/Q and Q/CH. Beside the major texture components, the others of extremely low volume fraction are embedded sparsely in these maps. The band width of these artificial EBSD maps is $504\mu m$, leading to a wavelength of $1008\mu m$ for surface roping. When discretizing the ideal orientation into Euler angles for these EBSD maps, a de la Vallée Poussin function with a half width of 1° is used as kernel in MTEX[116].

Fig. 5.3a shows ρ_{hv_g} for the typical texture components in cold rolled and recrystallized Al alloys. It can be seen that v_{R} has perfectly negative correlation with h, whereas v_{cube} is positively correlated with h. This is because peaks of h correspond to valleys of v_{R}, but to peaks of v_{cube}. It can further be observed in Fig. 5.3a that other texture components also have high $|\rho_{hv_g}|$ values, even though they exhibit only slight fluctuation in v_g (see, e.g. v_{Q} in Fig. 5.3 (b)). This is due to the fact that the correlation coefficient is dimensionless and independent of the origin (see, e.g. Section 5.2). It is this feature of the correlation coefficient that necessitates the additional consideration of the standard deviation of Eq. (5.2), to characterize the texture inhomogeneity.

It can be seen in Fig. 5.3b that $S_{v_{\mathrm{R}}}$ and $S_{v_{\mathrm{cube}}}$ are much higher than those of other components since v_{R} and v_{cube} feature much higher fluctuations. Then, δ_g is calculated by assuming $\epsilon_{\mathrm{TD}} = 0.15$ to characterize the plastic response. It can be clearly seen in Fig. 5.3c that the Goss orientation exhibits the highest propensity for surface roughening, whereas the R and cube orientations exhibit a rather low propensity. Consequently, the normalized η_g is shown in Fig. 5.3d, which identifies the two predominant texture components, viz. the R and cube orientations, governing roping. With a negative η, the R component contributes most to the valleys of the roping profile. In contrast, the cube component contributes most to the roping peaks. It is not surprising that the Goss component, with the highest roughening tendency, features a very low contribution to the roping profile. This indicates that not only δ_g but also S_{v_g} plays an important role for the present case. Besides, η_g determined for the other artificial EBSD maps can quantify the contribution of g to their corresponding roping profiles, as expected. Therefore, the "contribution factor" defined by Eq. (5.4) is a meaningful quantity combining spatial texture fluctuation and plastic anisotropy. All three aspects, viz. ρ_{hv_g}, S_{v_g} and δ_g, which are not independent, should merge in a combined quantity to characterize the contribution of texture components to roping.

Then, η_g is sought for an EBSD map measured on a subsurface layer, which is $80\mu m$ beneath the top surface of an AA6016 T4 state sheet sample suffering from severe roping. Fig. 5.1a shows this EBSD map with only the cube and CG grains. A visual observation based on such a figure cannot quantify the contribution of an orientation to surface roping. Using Eq. (5.4), a normalized η_g is computed for the typical texture components in cold rolled and recrystallized AA6016 T4 state sheets and is shown in Fig. 5.4. This suggests that CG, Q, CH and Goss are the major texture components contributing to roping for the studied sample. Among them, CG and Goss correlate to the roping peaks and CH and Q to the valleys. On the contrary, the spatial

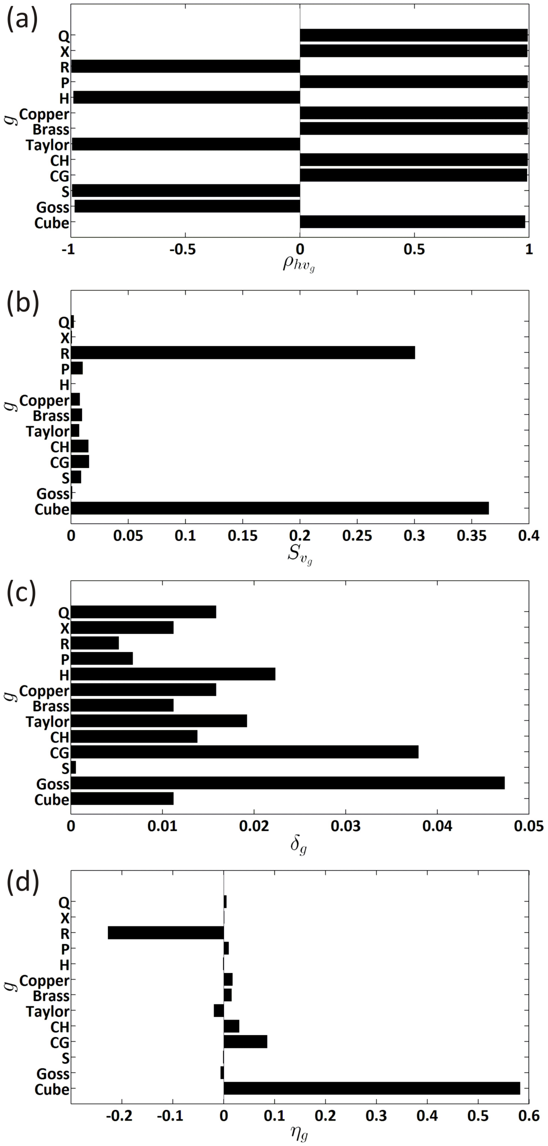

Fig. 5.3: Contribution factor calculation procedure for an artificial R/cube EBSD map: (a) correlation coefficient ρ_{hv_g} between h and v_g; (b) standard deviation S_{v_g}; (c) ND plastic strain difference δ_g (see e.g. Eq. 5.3); (d) contribution factor η_g of each g normalized by $\sum |\eta_g|$. Note that the index notation of copper and Dillamore component is $\{112\}\langle 111\rangle$ and $\{4\ 4\ 11\}\langle 11\ 11\ 8\rangle$, respectively.

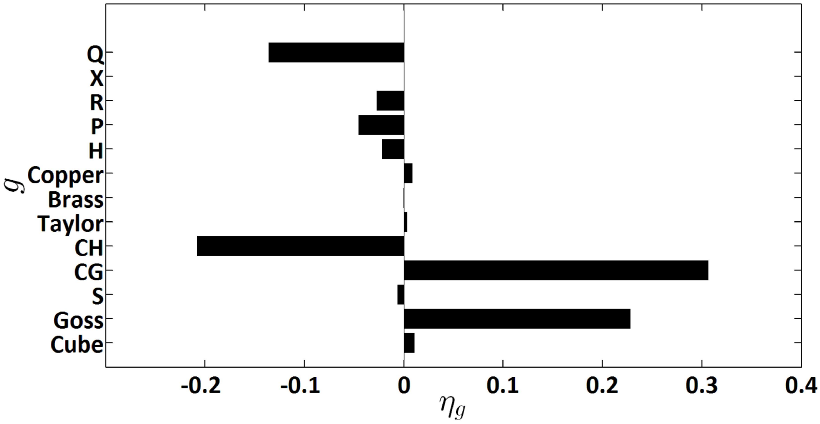

Fig. 5.4: Contribution factor η_g of each g normalized by $\sum |\eta_g|$.

distribution of texture components such as cube, brass-$\{011\}\langle 211\rangle$, S-$\{123\}\langle 634\rangle$ and X does not contribute to h significantly in Fig. 5.1c, even through they can exhibit high $\bar{v_g}$, and S_{v_g} (see, e.g. v_{cube} in Fig. 5.1 (b)). This finding supports an earlier result that a pronounced cube recrystallization texture does not necessarily imply that the material will suffer from roping [9].

5.4 Conclusions

The r-value is used to quantify the strain thinning resistance of a given texture. The analysis of r-value indicates that all the ideal components in Table 5.1 are plastically anisotropic under the UT modes considered. For AA6xxx-T4 sheets with the typical cold rolling and recrystallization texture, UT-TD has higher probability of inducing roping than UT-RD, because the r-value difference between the most thinning resistant and the most thinning susceptible component under UT-TD is larger than that under UT-RD.

The proposed contribution factor, η_g, can quantify the contribution of a specific orientation, g, to the surface roping profile. $\eta_g > 0$ indicates that g contributes to roping peaks, whereas $\eta_g < 0$ denotes g corresponding to valleys. If $\eta_g = 0$, g does not contribute to roping. A greater absolute value of η_g indicates more significant contribution of g to roping. It has been demonstrated using artificial EBSD maps that the contribution of a texture component can be quantitatively analysed by the proposed method (see Eq. (5.4)). This can be very helpful to guide industrial practice to reduce roping. For the studied Al sheet, the predominate roping contributors among the texture components are CG, Goss, CH and Q, with CG and Goss correlating to the roping peaks and CH and Q to the valleys, respectively. It is stressed that, strictly speaking, η_g given by Eq. (5.4) depends on the overall texture of the material. In principle it should be calculated again for each new sample. It is expected that η_g would nevertheless be a good indication of the sensitivity of the roping tendency to a particular texture component for a given family of textures. In other words, this η_g quantifies the importance of a specific texture component, g, with respect to the roping propensity. This is expected to be valid for a given family of materials, e.g. certain roping susceptible aluminum alloys with similar textures due to similar thermomechanical histories.

Chapter 6

General Conclusions and future work

"Every great and deep difficulty bears in itself its own solution.
It forces us to change our thinking in order to find it."
Nils Bohr

6.1 Summary

In this thesis, roping or ridging in AA6xxx alloys has been investigated. As a meso-scale banded roughening phenomenon, roping is aesthetically undesirable for outer panel applications in the automotive industry. It is widely accepted that roping is a result of spatial texture variation under a certain deformation mode.

In Chapters 2 and 3, the MW method is proposed to bridge the length scale gap between the grain scale of the individual orientations and the macro-scale of roping. Based on this method, the meso-scale roping crystal plasticity model has been developed and validated. Basically, this roping model is based on the r-value prediction by the FC Taylor model. Local texture information of the statistically significant EBSD maps is selected by the MW, and then fed into the model to simulate roping. This MW tries to capture the plastically contrasting grain colonies, i.e. "ghost grains", hypothetically originating from invisible mother grains at an earlier stage so that the influence of the thermomechanical history can be considered to interpret roping based on EBSD maps. Two different versions of the mesoscopic MW roping model are proposed, depending on the input EBSD data, viz. surface and through-thickness microtextures. Both versions turn out to be capable in roping analysis.

In order to guide industry to fine tune the upper stream thermomechanical processes, A ‘contribution factor’ has been proposed in Chapter 5 to assess the ‘sensitivity’ of roping tendency to the strength of a particular texture component. The calculation of this ‘contribution factor’ relies on the MW method too. This is expected to be valid for a given family of Al alloys.

The general findings of this thesis can be summarized below:

The application of the mesoscopic MW roping model to the experimental EBSD maps proves the capability of the model in the roping analysis. The model is able to predict both the wavelength and the amplitude on the basis of an EBSD scan.

For the investigated samples, it is found that the predicted roping wavelength is insensitive to the choice of the size of the window. However, the predicted roping amplitude approximately reaches the maximum, when the window width satisfies Eq. 2.7: $w = \left(n + \frac{1}{2}\right)\lambda, \quad n = 0, 1, 2 \cdots$.

It is demonstrated by the MW model that roping can be interpreted as a result of the existence of volumes with contrasting textures at the meso-scale with respect to a certain deformation mode. Therefore, the MW model can also be used to investigate the spatial texture distribution.

Intrinsically, the spatial texture distribution of the roping sample results in higher roughening propensity than that of the non-roping through layer-wise analysis. The spatial texture distribution at the free surface does not penetrate into the bulk. Instead, it changes gradually through the thickness direction. Throughout the entire half thickness of the samples, no spatial texture distribution of a single layer extends to another layer.

A single layer of grains is not sufficient to promote the experimentally observed surface roughness. Therefore, the collective plastic behavior of a number of layers of grains from the free surface is important in roughness formation. It is found by the mesoscopic MW roping model that the first 8 layers of grains responsible significantly for the roughening formation. It might be further suggested that the grains deeper than those 8 layers would be more constrained by their surrounding matrix.

The experimentally observed irregular roping type has been successfully simulated by analyzing the upper and lower surfaces separately.

The MW roping model can be used to try to predict the roping tendency based on statistically relevant surface EBSD maps, so that objective roping evaluation can be achieved for practical purposes. However, one has to validate this model with more samples of the same materials to make sure its results are reproducible.

The proposed contribution factor, η_g, can quantify the contribution of a specific orientation, g, to the surface roping profile. $\eta_g > 0$ indicates that g contributes to roping peaks, whereas $\eta_g < 0$ denotes g corresponding to valleys. If $\eta_g = 0$, g does not contribute to roping. A greater absolute value of η_g indicates more significant contribution of g to roping.

For the studied AA6xxx roping sheet, the predominate roping contributors among the texture components are CG, Goss, CH and Q, with CG and Goss correlating to the roping peaks and CH and Q to the valleys, respectively. This η_g quantifies the importance of a specific texture component, g, with respect to the roping propensity.

The moving window method has been successfully used to identify an unrecognized hidden mesoscopic length scale, i.e. the roping wavelength in AA6016 sheets. This method may be applied to similar phenomena, where a certain length scale exists but is invisible.

6.2 General conclusions

The general conclusions of this thesis can be summarized below:

Roping is a result of existence of mesoscopic volumes with contrasting textures due to the fact that the roping wavelength is much larger than the grain size and is independent of the window size which is a parameter used in the so-called MW roping model. It is more appropriate to interpret roping based on the meso-scale of texture banding rather than on the micro-scale of orientation banding.

Good agreement in both wavelength and amplitude has been reached between experimental surface profiles and those simulated by the MW roping model.

It is very useful to quantitatively analyze texture by a quantity, which is a function of its ODF, such as r-value, instead of graphical representation of its ODF in order to reveal the texture difference between the mesoscopic volumes.

6.3 Future work

It is well known that precipitation is the most important hardening mechanism in Al alloys. In order to satisfy the mechanical requirements for industrial applications, delicate thermomechanical processes are designed to control the microstructure evolution. Among all, the precipitation and particle size and its distribution serve as useful medium to modify the recrystallization texture. Therefore, the chemical segregation, especially the micrometer-scale second phase particles, should be investigated thoroughly. The distribution of these particles can influence the spatial distribution of local texture during the recrystallization process and alter the plastic behavior of surrounding matrix. It is possible that the spatial alignment of those indissoluble and hard particles is one of the sources of roping or ridging.

Detailed large-scale 3D EBSD is crucial to understand the roping or ridging origin in terms of the collective plastic deformation of mesoscopic representative volume element of grains. In order to gain insight into surface roughening, the through-thickness grain interactions should be further studied by more advanced plasticity models, i.e. crystal plasticity finite element method and visco-plastic fast Fourier transform.

Since both R_a and λ are of statistical character for periodic surface characterization, more advanced statistical analyses should be done to investigate roping or ridging.

The MW roping model developed based on mesoscopic representative volume elements with contrasting textures for AA6xxx sheets can be expected to be adapted to simulate ridging in FSS sheets. Thus, a MW ridging model can be developed with emphasis on out of plane shear components.

Appendix A

Tensile properties

The mechanical properties of the room temperature aged roping and non-roping sample were tested and summarized herein. The standard dog-bone shaped tensile test samples were machined and tested according to the ASTM standards [50–52].

Fig. A.1 shows the true stress-strain curves for both samples. Multiple tests were done for all three directions, viz. RD, 45 and TD. Then the σ-ϵ curves along all these directions are compared in Fig A.2. It can be seen that the roping sample exhibits very similar tensile properties along all the three directions, while the non-roping sample shows different plastic tensile properties in these directions, among which the non-roping sample features the lowest yielding strength and σ-ϵ curve in TD. This can be attributed to the difference in their global texture as shown in Figs. 2.7 and 2.8.

The strain ratio, r-value, is an important parameter in sheet metal forming processes [147, 148]. It depends on the crystallographic anisotropy of a sheet metal [107, 108, 131, 136, 147–153]. Table A.1 summarizes the drawing properties of both sheet samples. In this table, ϵ^p is plastic true strain. r_{RD}, r_{45} and r_{TD} are r-values measured along RD, 45° to RD and TD, respectively. They are obtained from Fig. A.3 at $\epsilon^p = 0.15$. Note that each r-value at $\epsilon^p = 0.15$ is averaged for all tests in each direction of either sample.

Table A.1: Summary of r-values of both samples at $\epsilon^p = 0.15$.

sample	$r_{\mathbf{RD}}$	r_{45}	$r_{\mathbf{TD}}$	r_m	Δr
Roping	0.64	0.53	0.84	0.63	0.21
Non-roping	0.70	0.43	0.64	0.56	0.22

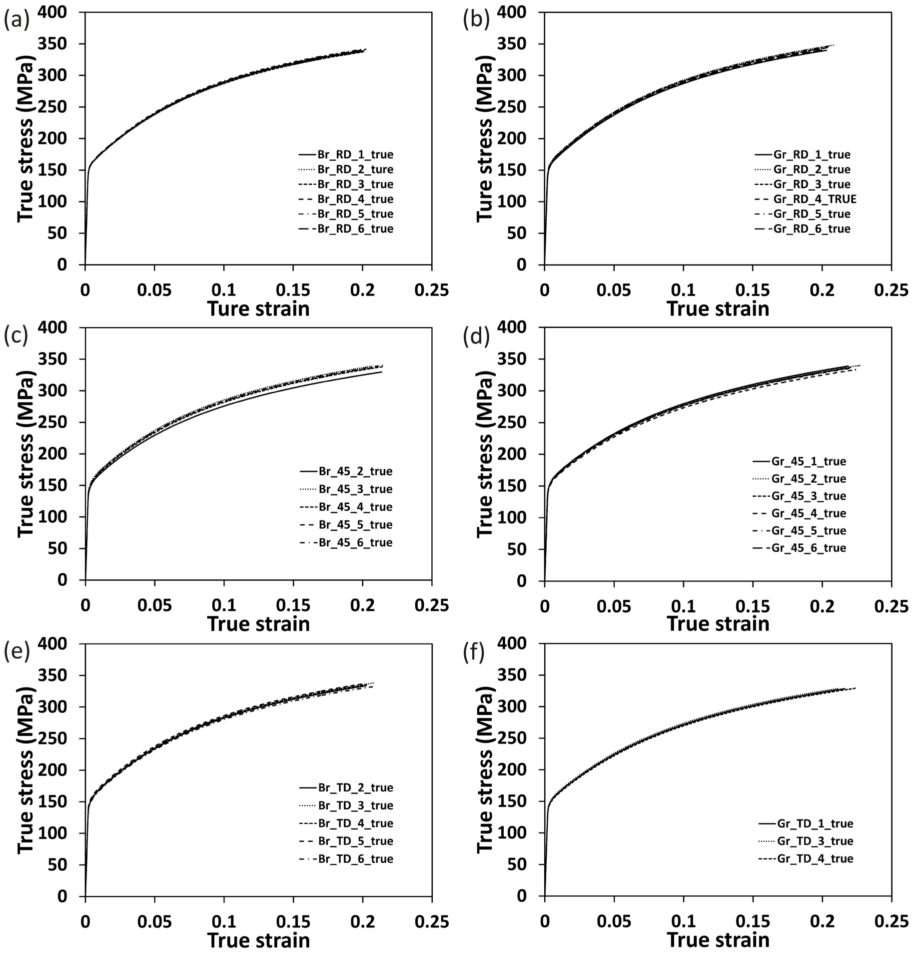

Fig. A.1: The σ-ϵ curves for the roping sample measured by UT along (a) RD, (c) 45° to RD as well as (e) TD and for the non-roping sample along (b) RD, (d) 45° to RD as well as (f) TD. Note that at least three tests have been done for each sample along each direction.

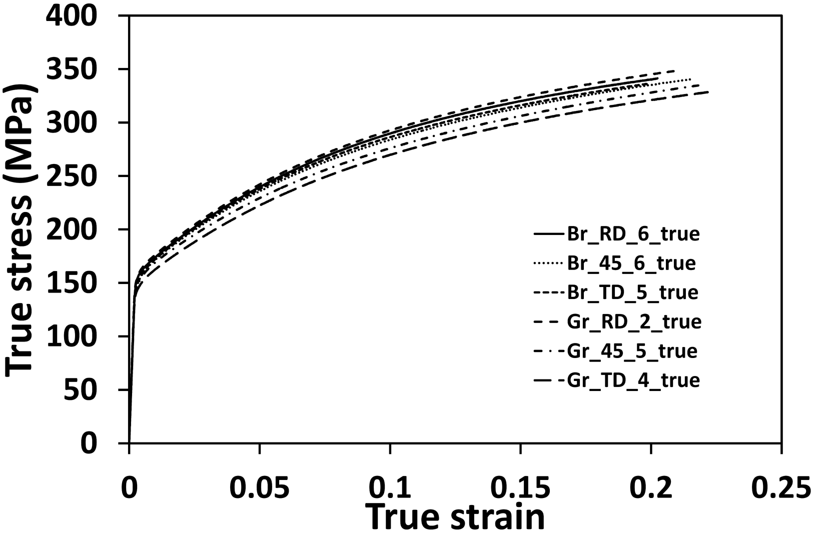

Fig. A.2: The σ-ϵ curve for both roping and non-roping samples measured by the UT along three direction directions.

r_m denotes the normal plastic anisotropy and is defined in Eq. A.1. For good deep drawing properties, it should be large, thus leading to a small thickness reduction.

$$r_m = \frac{r_{RD} + 2r_{45} + r_{TD}}{4} \tag{A.1}$$

Δr represents planar anisotropy and is defined in Eq. A.2. It is a measure of the amount of ears, that will develop on the edges of deep-drawn cylindrical cups or similar parts. For most applications, values of Δr near 0 are preferred to minimize the earing formation [154].

$$\Delta r = \frac{r_{RD} - 2r_{45} + r_{TD}}{2} \tag{A.2}$$

It can be seen from Table A.1 that both sample are of very similar formability. It is worth noting that the texture is believed to be unchanged though both samples experienced natural aging. It is reported by Prillhofer *et al.* [57] that the roping behavior was not influenced by storage periods, i.e. natural aging at room temperature. Therefore, the texture at this state, in which the microtexture and surface topography were measured, should be the same as that in the T4 state.

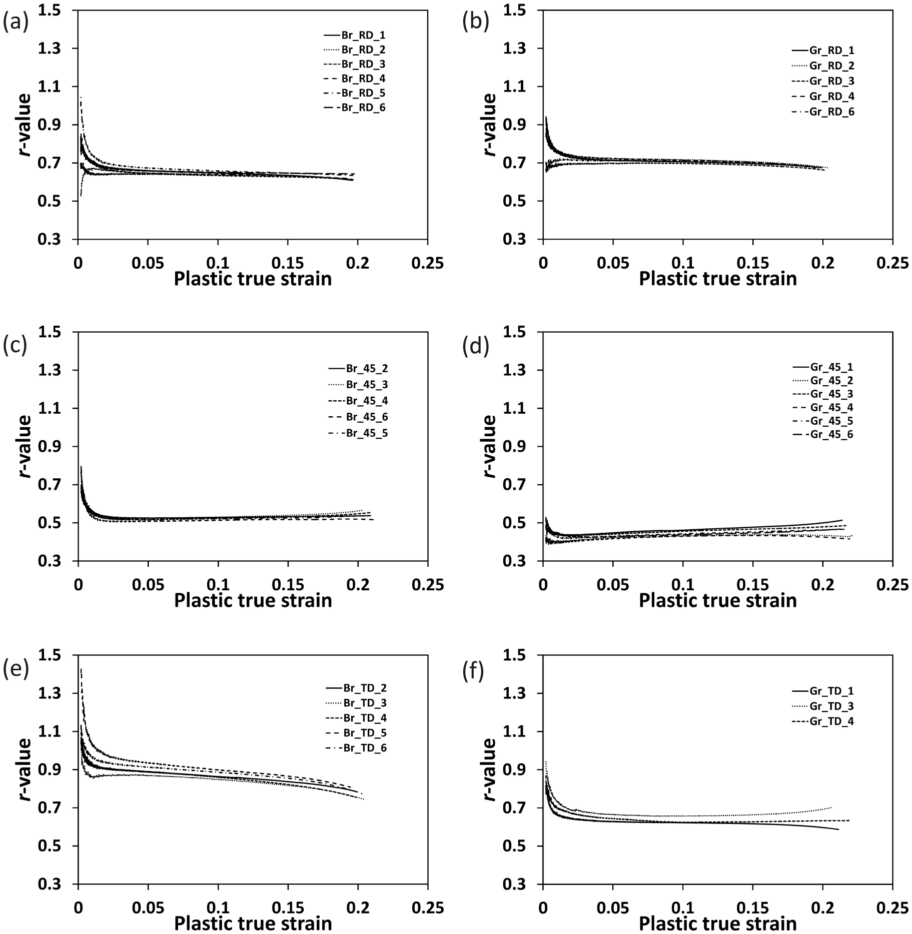

Fig. A.3: The $r$value-ϵ curve for the roping sample measured by UT along (a) RD, (c) 45° to RD as well as (e) TD and for the non-roping sample along (b) RD, (d) 45° to RD as well as (f) TD. Note that at least three tests have been done for each sample along each direction.

Appendix B

ODF analysis on spatial texture heterogeneity

Discrete EBSD data selected by a MW were transformed by the MTM-FHM software system [102] into continuous ODFs. Specifically, a Gaussian distribution was applied around each orientation (in the convention proposed by Bunge [104]) of the EBSD data to produce an ODF and afterwards all these ODFs for the single orientations were added together to form a final ODF for the whole EBSD data. During the ODF calculation process, a Gaussian spread Φ_0 of 7° was used together with orthorhombic sample symmetry and a harmonic series expansion rank, l_{max}, up to 22. Note that the orthorhombic sample symmetry is commonly assumed for industrial rolled sheet metals [155, 156]. Thus, the orthorhombic sample symmetry was imposed in order to reduce the Euler space to $0 < \varphi_1 < \pi/2$, $0 < \Phi < \pi/2$, and $0 < \varphi_2 < \pi/2$ using the convention formulated by Bunge [104] for the Euler angles to facilitate visual inspection and direct comparison with ODFs in literature [9, 25, 44, 63, 120]. In addition, the texture index (TI) was calculated for each ODF according to Bunge[104] by the MTM-FHM software system.

$\varphi_2 = 0°$, $\varphi_2 = 35°$ and $\varphi_2 = 45°$ sections are used to demonstrate an ODF since they contain the positions corresponding to the highest densities of typical texture components in the Euler space, which are schematically illustrated by Fig. B.1c. For each ODF, the highest density $f(\mathrm{g})_m$ and its corresponding crystal orientation $\mathrm{g}_m = (\varphi_1, \Phi, \varphi_2)$ are given together with the TI to the right of the ODF sections as shown in Fig. B.1.

Texture inhomogeneity on the surface and in the through-thickness direction will be analyzed in terms of ODF in Sections B.1 and B.2, respectively.

B.1 Surface texture heterogeneity

The MW method can be readily used to analyze the spatial texture heterogeneity. Specifically, an ODF can be obtained for a set of discrete orientation data selected by a MW on top of an EBSD map. The ODF sections can be visually analyzed to investigate the spatial texture inhomogeneity. This visual analysis is qualitative. The studied EBSD maps of the roping and non-roping samples are shown in Fig. 2.5.

Before analyzing the spatial texture heterogeneity, global textures for both samples are examined. Fig. B.1a and b shows the ODF sections of the global textures for the roping and non-roping sample, respectively. It should be reminded that these ODFs are essentially the same as those shown in Fig. 2.7 except that the orthorhombic sample symmetry is imposed and l_{max} is reduced to 22 for the ODFs in Fig. B.1.

It can be seen in Fig. B.1a that the prominent texture components of the roping sample are cube with the highest density of 19.41 times random, S, Goss, CH and CG. It can then be seen in Fig. B.1b the non-roping sample has major components of cube with $f(\mathrm{g})_m = 9.06$ times random, CH and Q. No Goss and a weak S component is observed in the non-roping sample. Moreover, the non-roping sample features a less sharp texture than the roping one since the TI of the former is lower than that of the latter.

A window size of $500\mu m$ in TD and of $2.6mm$ in RD was used to select M-RVEs of discrete orientation data. It is worth noting that the size of the EBSD maps measured on the sheet surface is $7.8mm$ in TD and $2.6mm$ in RD. So, the window used extends over the entire dimension in RD of the EBSD maps. For each selected M-RVE with a specific texture, an ODF was computed. Meanwhile, a r-value can be simulated by the FC Taylor model based on the same texture for UT in TD. (see, e.g. Chapter 4 for more details).

Fig. B.2 shows simulated r_{TD} vs. its corresponding window centroid position in TD from the left side of the EBSD maps for both roping and non-roping samples as well as their randomized derivatives (see e.g. Section 2.3.3). Note that the randomized roping sample was numerically generated based on the EBSD data of the roping sample. Therefore, the global textures of these two sample are the same, whereas the spatial texture heterogeneity is removed in the randomized sample. The same applies to the randomized non-roping sample. It can be seen in Fig. B.2 that the r_{TD} profiles of the randomized samples are of little variation. This indicates that these randomized samples have averaged homogeneous strain thinning properties. For both roping and non-roping sample, textures corresponding to three peaks, three valleys and three mean points are chosen. Their positions are illustrated in Fig. B.2 and listed in Table B.1.

The intersection points between the randomized samples and their corresponding originals are of particular interest. Fig. B.3 shows the ODF sections for the roping sample at three mean points. It can be seen that all three textures feature a strong cube component as indicated by their $f(\mathrm{g})_m$ and g_m. However, m2 texture obviously

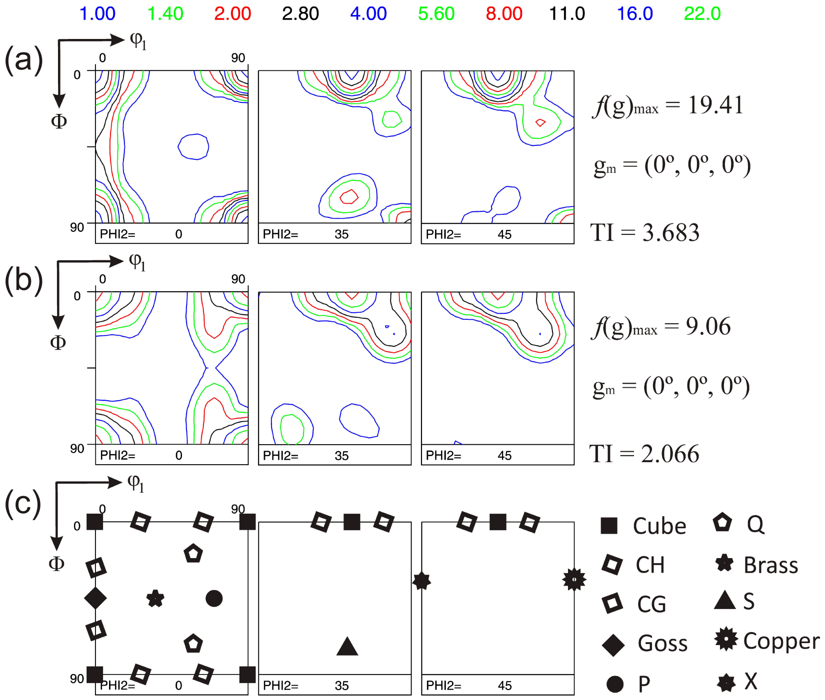

Fig. B.1: The ODF sections for global texture of the (a) roping and (b) non-roping sample calculated based on the EBSD data. The global texture is obtained by making the window size as large as the entire EBSD map. Positions of ideal texture components corresponding to the highest density are schematically illustrated in (c).

Table B.1: Window centroid position from the left side of EBSD maps for both samples (in μm).

Sample	p1	p2	p3	m1	m2	m3	v1	v2	v3
Roping	1796	3604	6212	2252	3036	5764	2380	4276	5436
Non-roping	2700	3980	7372	1172	4452	6212	3428	5332	6860

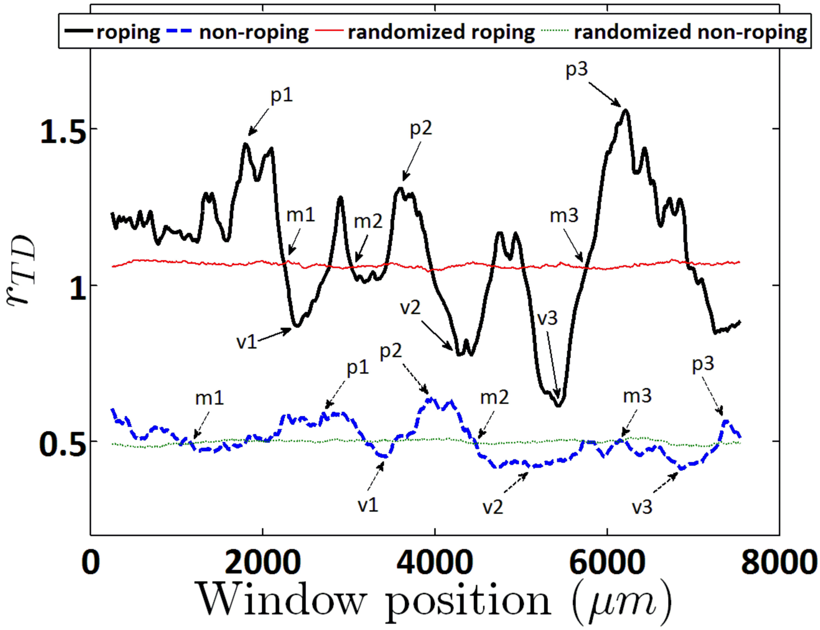

Fig. B.2: The simulated r_{TD} profiles for both samples together with their corresponding randomized samples. The positions of interest are marked out by arrows.

has stronger Goss and weaker cube component than m1 and m3. Then the rest of features of these three ODFs look quit similar, with CG, CH, S and P being identified. Furthermore, the major features of these ODFs look very similar to those of the global texture of the roping sample as shown in Fig. B.1a. It seems that slight modification of texture will not result in r_{TD}-value variation. However, this does not mean that r-values in other direction will not vary. Nevertheless, different ODFs can yield the same thinning property, r_{TD}-value.

Fig. B.4 shows the ODF sections for the roping sample at three peak positions. It can be seen that, despite appearance of Goss component with moderate densities, the highest densities, $f(\mathrm{g})_m$, are still located at the cube position, i.e. $(0°, 0°, 0°)$. Besides, these three textures all feature a high TI. It is interesting to see that the texture with the strongest Goss component (see, Fig. B.4a) does not correspond to the highest r_{TD} peak (see, Fig. B.2), whereas the texture with the strongest CG component (see, Fig. B.4c) correlates to the highest r_{TD} peak. This finding, therefore, suggests that the rotated cube component such as CG should play an important role in inducing roping peaks besides the Goss component. Compared with global texture of the roping sample as shown in Fig. B.1a, no major difference in Fig. B.4 can be observed visually.

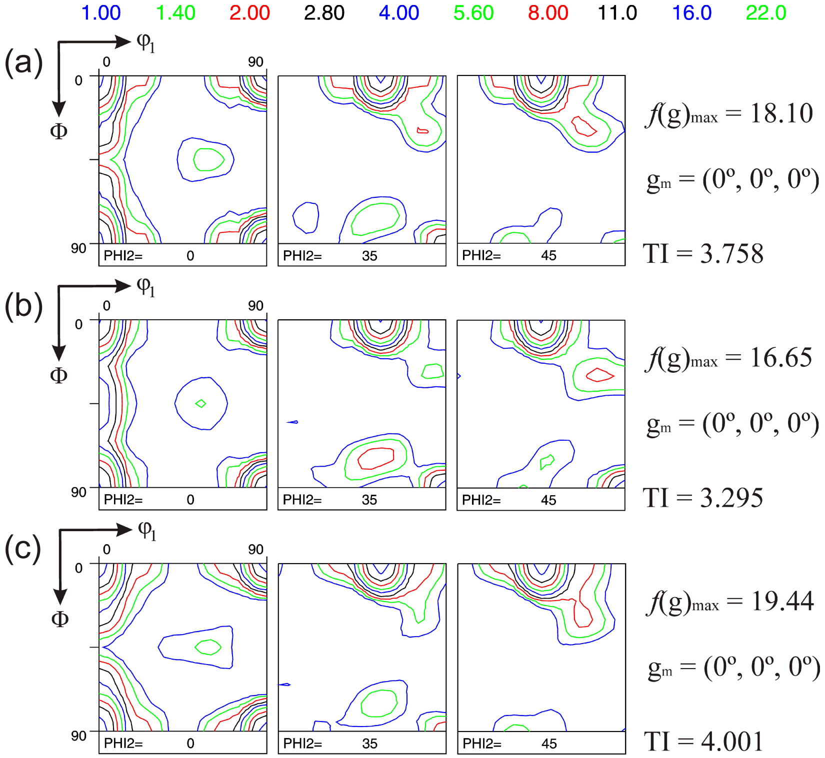

Fig. B.3: The ODF sections for the roping sample at (a) m1, (b) m2 and (c) m3.

The ODF sections for the roping sample at three valleys are shown in Fig. B.5. It can be seen that the major texture components are cube, CH, CG, S and P, whereas, the Goss component disappears. It can further be seen that the density of the CG component decreases from Fig. B.5a to Fig. B.5c, whereas the depth of valleys increases from v1 to v3 as shown in Fig. B.2. These observations imply that lack of Goss and CG components could be responsible for formation of valleys.

Comparing the textures at valleys in Fig. B.5 with the global texture in Fig. B.1a, one can see that the lack of Goss component is the most prominent difference. However, the ODF of m3 in Fig. B.3c looks very similar to that of v1 in Fig. B.5a. Therefore, lack of Goss component does not necessarily correspond to a roping valley, since the texture of m3 is also lack of Goss component. Additionally, it is interesting to see how such small ODF difference leads to obvious r_{TD}-value variation.

For the roping sample, lack of major difference between the global texture (see, Fig. B.1a) and those at peak positions (see, Fig. B.4) causes confusion in roping

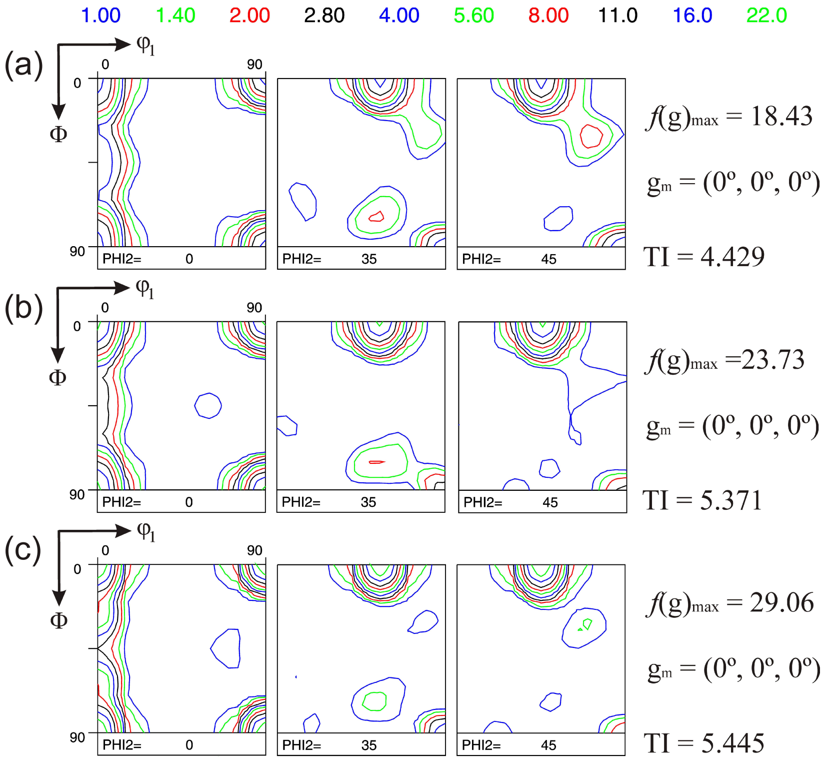

Fig. B.4: The ODF sections for the roping sample at (a) p1, (b) p2 and (3) p3.

analysis based solely on visual ODF examination. Moreover, it can be observed that the ODF of a mean position (see, Fig. B.3c) looks very similar to that of a valley (see, Fig. B.5a). This leads to more confusion because the r_{TD}-value difference between m3 and v1 cannot be distinguished based on the visual ODF assessment. Then, moderate differences can be observed between the ODFs at the mean positions as shown in Fig. B.3. However, they all result in the same r_{TD}-value. This adds further confusion to the visual ODF assessment for mechanical behavior prediction. Together with the contradicting findings, viz. some slight modification of texture not causing r_{TD}-value variation and some small difference between textures leading to obvious r_{TD}-value variation, all these confusions, therefore, suggest that quantitative texture analysis should be done to better predict mechanical behavior of polycrystalline materials.

For the non-roping sample, the spatial texture variation is expected to be lower than that in the roping sample, since its r_{TD}-value variation is lower. Fig. B.6 shows the ODF sections for the non-roping sample at mean positions. It can be seen that all textures but m3 have a cube component with the highest intensity. $f(\mathrm{g})_m$ of m3 texture locates at $\mathrm{g}_m = (20°, 75°, 20°)$, which is very close to the R component. This

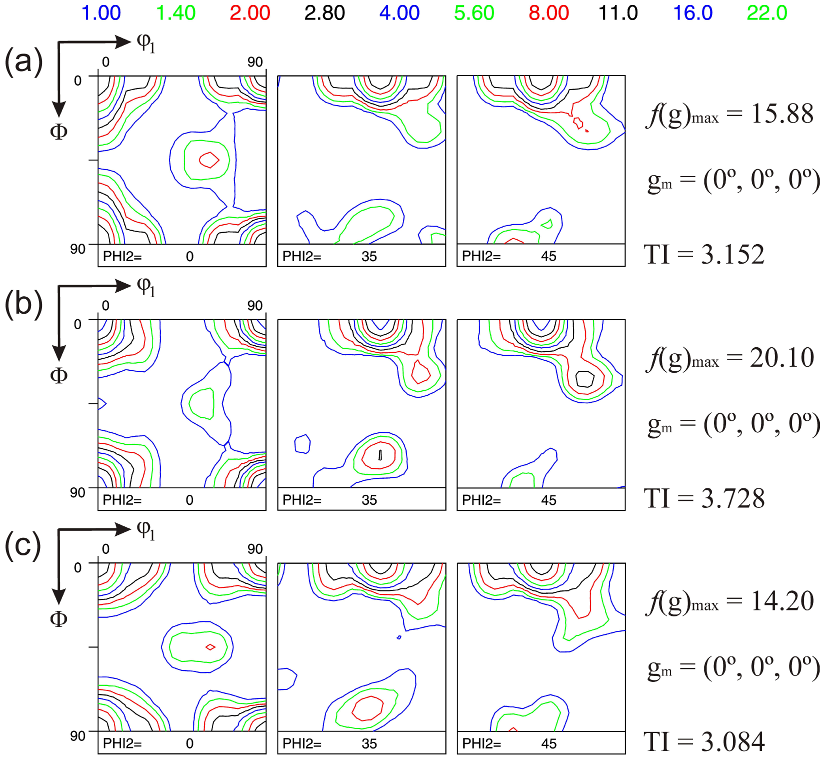

Fig. B.5: The ODF sections for the roping sample at (a) v1, (b) v2 and (c) v3.

makes the m3 texture distinct from the other two. Note that the R component is not illustrated in Fig. B.1c because it is only 7.8° from S component with respect to Cubic-Orthorhombic symmetry. Even though different textures are observed in Fig. B.6, they yield the same r_{TD}-value.

Fig. B.7 shows the ODF sections for the non-roping sample at three peak positions. It can be seen that the major components of them are cube, with the highest intensities, CH and Q. Since the non-roping sample features lower roughening property, as reflected by lower r_{TD}-value variation, all these texture at peaks look similar to the global one in Fig. B.1b.

Fig. B.8 shows the ODF sections for the non-roping sample at three valley positions. The observed major texture components are cube, with the highest intensities, CH and Q. It can be seen in Fig. B.8 that $f(\mathrm{g})_m$ of all three valley textures is as low as that of mean position textures. Another major feature is that cube rotates towards CH to a large extent, especially for v1.

Although spatial texture inhomogeneity in the non-roping sample is not as obvious

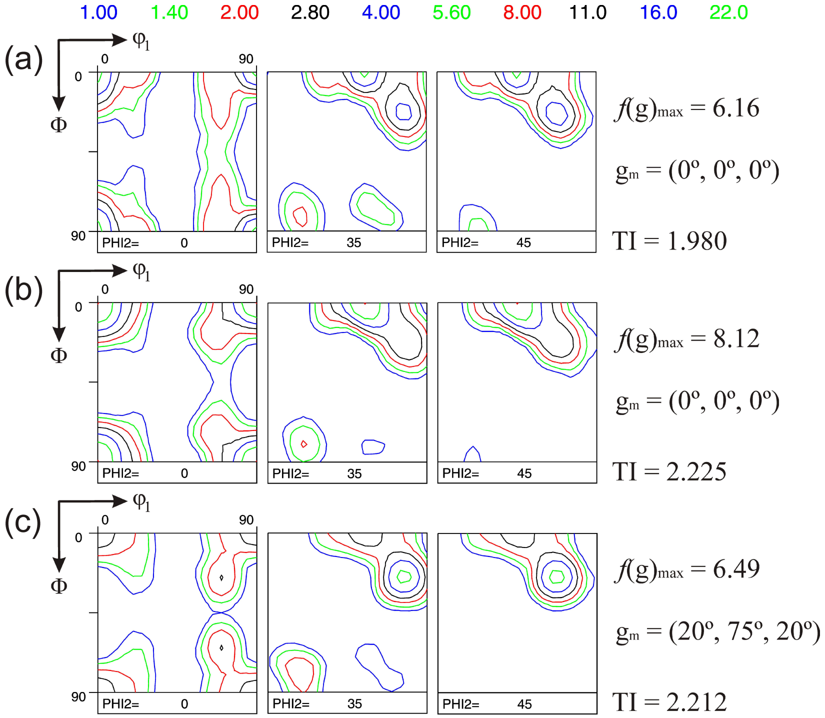

Fig. B.6: The ODF sections for the non-roping sample at (a) m1, (b) m2 and (c) m3.

as that in the roping sample, r_{TD}-value difference between p2 and v2 is 0.22, which is believed to be able to cause differential strain thinning. However, this difference cannot be understood by comparing their ODFs intensity quantitatively because the p2 ODF sections (see, Fig. B.7b) looks similar to those of v2 (see, Fig. B.8b), expect some minor difference in the intensities of cube, i.e. $f(\mathrm{g})_m = 11.43$ for p2 as well as $f(\mathrm{g})_m = 8.64$ for v2, and Q.

It has been demonstrated for the non-roping sample that the ODFs at the mean positions with moderate differences as shown in Fig. B.6 result in the same r_{TD}-value. Besides, visually similar ODF sections, e.g. Fig. B.7b of p2 and Fig. B.8b of v2, lead to r_{TD}-value variation. Therefore, these two findings recommend that quantitative texture analysis should be done for precise plastic behavior prediction.

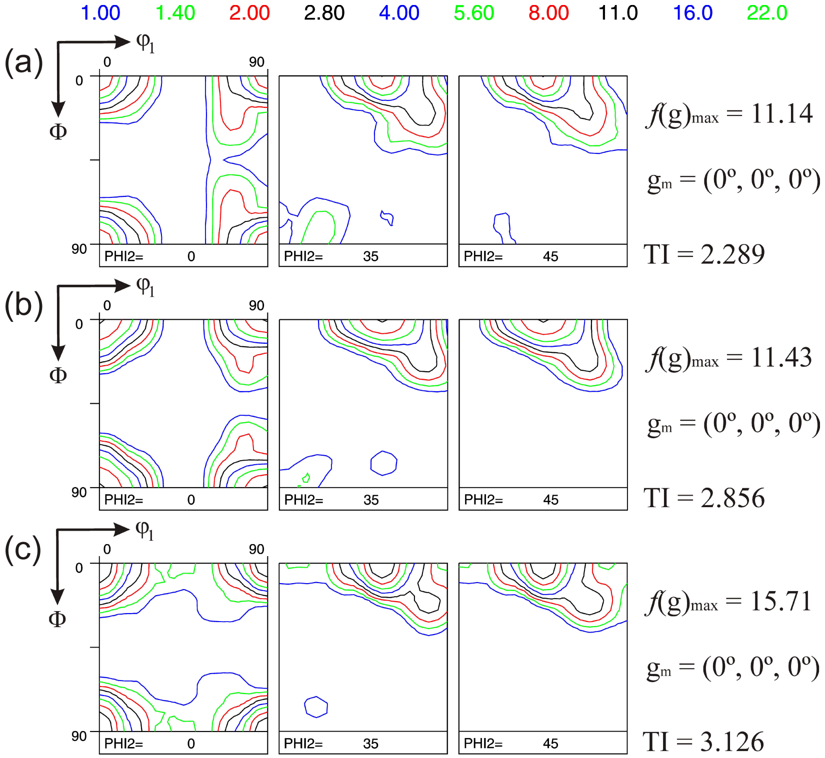

Fig. B.7: The ODF sections for the non-roping sample at (a) p1, (b) p2 and (3) p3.

B.2 Through-thickness texture heterogeneity

As pointed out by Engler *et al.* [157], most Al alloys develop pronounced through-thickness texture gradients during thermomechanical processes, such as rolling. The through-thickness texture gradients have been studied extensively [158–162]. Chapters 2 and 3 have demonstrated that textures in the subsurface will contribute to surface roughening. It can be interesting to investigate the texture gradient by the MW method based on EBSD maps. This MW method can be readily used to automate analysis of spatial texture gradient. In this case, large-scale through-thickness EBSD maps of the roping and non-roping samples as shown in Fig. 3.5 are studied.

Similar to the surface texture heterogeneity analysis in Section B.1, qualitative visual ODF examination can be done with the help of the MW method, which selects a set of discrete orientation data from an EBSD map. The selected set of orientation data needs to be transformed to an ODF before visual analysis.

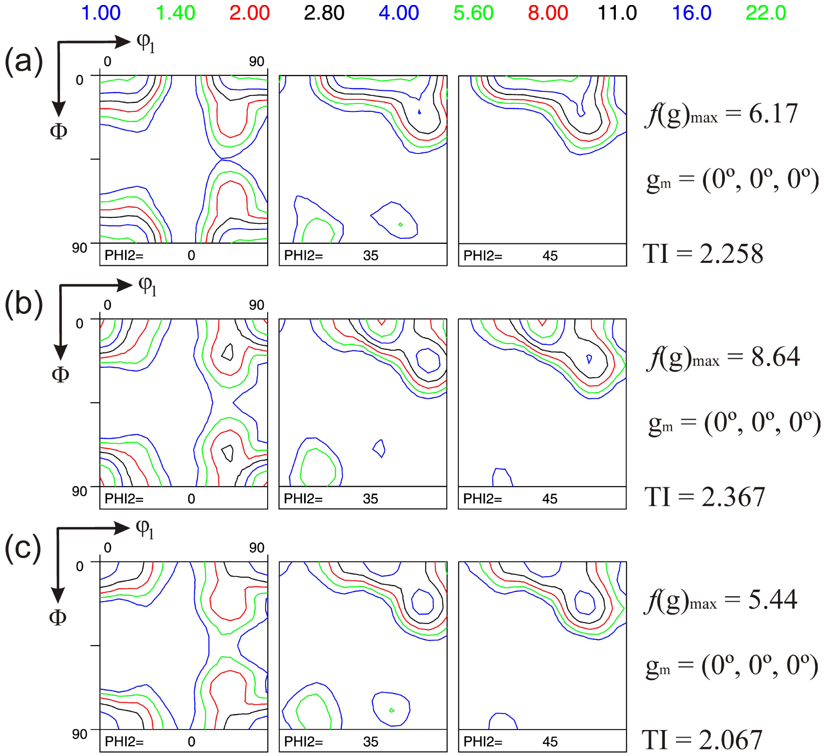

Fig. B.8: The ODF sections for the non-roping sample at (a) v1, (b) v2 and (c) v3.

Prior to analyzing the through-thickness texture heterogeneity, global through-thickness textures for both samples have been examined. Fig. B.9 shows the ODF sections of the global through-thickness textures for both samples. It should be reminded that these ODFs are obtained by making the window size as large as the entire EBSD map so that all orientation data are used for ODF computation.

It can be seen in Fig. B.9a that the prominent texture components of the roping sample are cube with the highest density of 11.06 times random, Goss, S, CH, CG and P. It can then be seen in Fig. B.9b the non-roping sample has major components of cube with $f(\mathrm{g})_m = 10.39$ times random, CH and P. Weak Goss and S component can also be found in the non-roping sample. Unlike the surface textures, the non-roping sample features sharper texture than the roping one since the TI of the non-roping is higher than that of the roping.

A window size of $32\mu m$ in ND was used. Its size in TD extends over the entire dimension of EBSD maps. Note that the average grain size measured by intercept

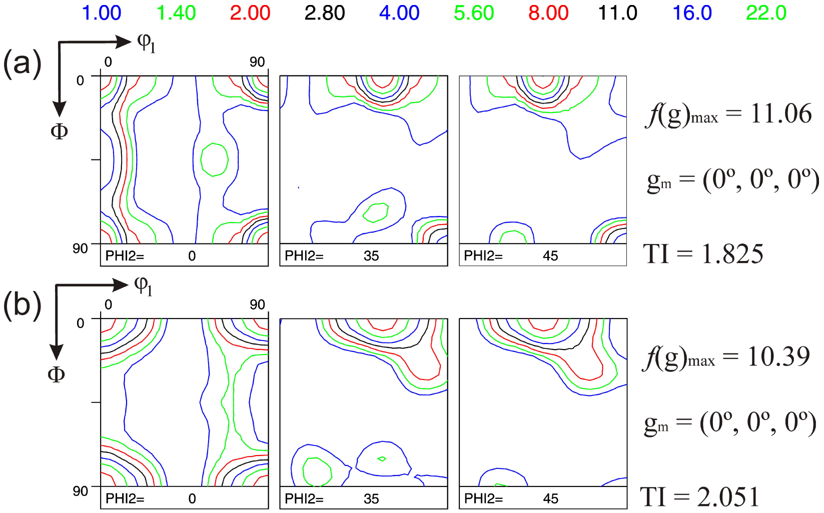

Fig. B.9: The ODF sections for the (a) roping and (b) non-roping sample calculated based on the through-thickness EBSD data. The global through-thickness texture is obtained by making the window size as large as the entire EBSD map.

method is 13 and 16μm, for the roping and non-roping sample, respectively (see Table 3.1). Therefore, the window used select a set of discrete orientation data from approximately two layers of grains. For each selected set of orientation data, an ODF was computed. Meanwhile, a r-value was simulated by the FC Taylor model based on the same texture under the assumption that these selected orientations constitute a tensile sample subject to UT in TD. (see e.g. Chapter 4 for more details).

Fig. B.10 shows simulated r_{TD} vs. its corresponding window centroid position in ND from the upper side of the EBSD maps for both roping and non-roping samples. Note that the middle position in ND of EBSD maps of both samples is set to be the origin of the horizontal axis (see Fig. B.10), whose positive direction goes from the upper side of EBSD maps to the lower (see Fig. 3.5). For both roping and non-roping samples, textures corresponding to five layer positions are chosen. These positions are illustrated in Fig. B.10 and listed in Table B.2. Specifically, l1 and l5 corresponds to the upper and lower surface layers, respectively, whereas l2 and l4 to the intermediate subsurface layers between the surface and the middle, i.e. l3. It can be seen in Fig. B.10 that the non-roping sample exhibits a shallow r_{TD}-value increase from about 0.5 at l1 and l5 to about 0.8 at l3. However, r_{TD}-value of the roping sample decreases from about 1 at l1 and l5 to about 0.7 at l2 and l4 before climbing up to 2.4 at l3. By comparing the two samples, it can be seen in Fig. B.10 that the variation of the r_{TD} profile of the non-roping samples is much lower than that of the roping. This indicates that the non-roping sample exhibits weaker texture gradient in ND than the roping.

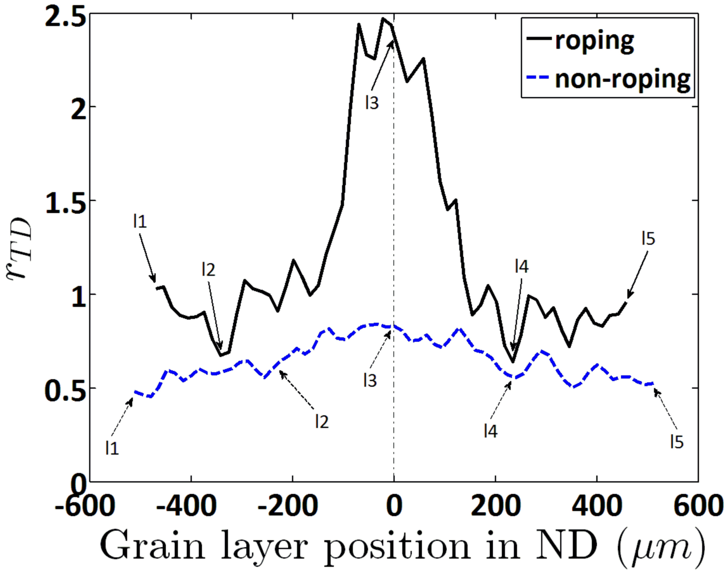

Fig. B.10: The simulated r_{TD} in the trough thickness direction for both samples.

Table B.2: Window centroid position with respect to the mid line of EBSD maps for both samples (in μm).

Sample	l1	l2	l3	l4	l5
Roping	-470	-342	0	234	458
Non-roping	-512	-240	0	240	512

Fig. B.11 shows the ODF sections for the roping sample at five different layer position through the thickness direction. It can be seen that the highest intensity appears at the cube position, i.e. $\mathrm{g}_m = (0°, 0°, 0°)$ for all these five layers except l3. The common major texture components for all layers as shown in Fig. B.11 are cube, Goss, CG and CH. At the surface, the textures are sharpest with TI being 2.36 and 3.89 for l1 and l5, respectively. It can be seen in Fig. B.11a and e that the ODF sections look very similar to those from the surface EBSD map of the roping sample (see, Fig. B.1a). This is expected. At intermediate subsurface layers, i.e. l2 and l4, the texture sharpness is reduced, with especially the cube and Goss components being weakened. Meanwhile, P component appears with intensity higher than 2. In the middle of the sample, Goss becomes the most prominent texture component as $\mathrm{g}_m = (0°, 40°, 0°)$, whereas CH and S disappear. It can also be seen in Fig. B.11c that $\langle 100 \rangle$ // RD fiber appears.

Fig. B.12 shows the ODF sections for the non-roping sample at five different layer position in ND. It can be seen that the most prominent texture component is cube as

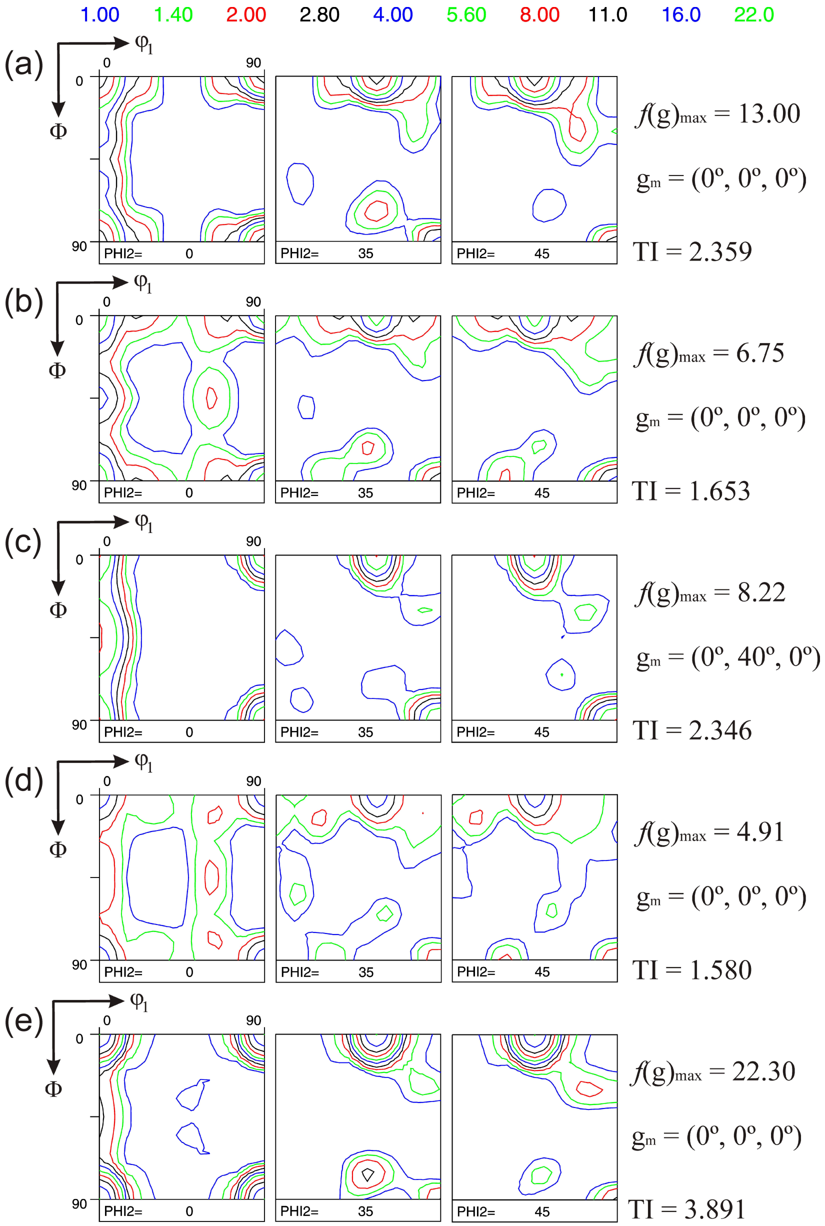

Fig. B.11: The ODF sections for the roping sample at (a) l1, (b) l2, (c) l3, (d) l4 and (e) l5.

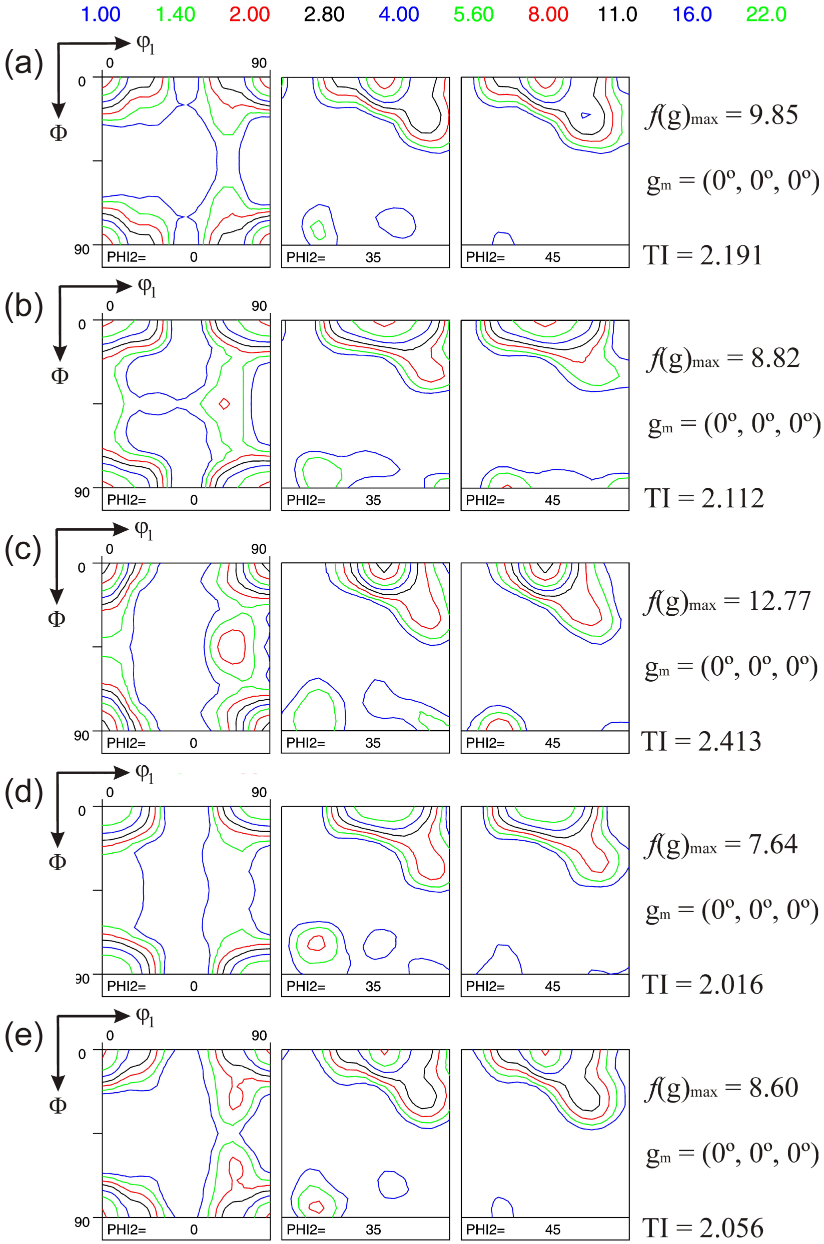

Fig. B.12: The ODF sections for the non-roping sample at (a) l1, (b) l2, (c) l3, (d) l4 and (e) l5.

$g_m = (0°, 0°, 0°)$ for all these five layers. Besides, CH, CG and Q can be identified to be the common major texture components for all layers as shown in Fig. B.12. Weak Goss can be observed in all but the surface layers. The texture is sharpest in the middle with TI of l3 being 2.41 and $f(g)_m$ of cube being 12.77 times random, compared with others. It can be seen in Fig. B.12c that P can be identified as a moderate component with intensity higher than 2 times random in addition to the common major components for all layers. At l2 and l4, which are intermediate subsurface layers, the ODFs look very similar to those at the surface, except that the textures at l1 and l5 feature higher volume of Q than those at l2 and l4. This difference can be of minor importance since r_{TD}-value difference between surface and intermediate layers is only approximately 0.1.

In view of plastic properties of the roping sample, the r_{TD}-value difference between l3 and l1 or l5 is significant as shown in Fig. B.10. However, the visual ODF difference between them is less significant (see Fig. B.11). Without the knowledge beforehand that a single crystal with a Goss orientation has an infinitely high r_{TD}-value, an intensity increase of about 5 times random from l1 (see Fig. B.11a) or l5 (see Fig. B.11e) to l3 (see Fig. B.11c) will not be expected to cause an r_{TD}-value increase by 1.4. It is thus suggested that one should analyze texture quantitatively to predict the plastic behavior more precisely.

Similar to the texture heterogeneity analysis in Section B.1, the visual ODF inspection is confusing in the sense that the though-thickness texture gradient is not quantitatively reflected on the basis of ODF sections. A numeric parameter dependent of texture, e.g. r-value, is able to disclose the texture gradient quantitatively.

B.3 Conclusions

The texture heterogeneity in both TD and ND has been analyzed by visual inspection on the basis of ODF sections. It is found that different ODFs can result in the same plastic thinning property. It is also found that visually similar ODFs can lead to significant different in plastic behavior. Therefore, the visual ODF evaluation with focus on major texture components is insufficient to reveal the plastic behavior without considering the contribution of the other components.

This visual ODF inspection is qualitative in the sense that one basically focuses on the major texture components with high orientation density while omitting the rest. A qualitative ODF analysis is sufficient in some cases, whereas it is insufficient in this case, where texture heterogeneity and its influence on plastic behavior need to be assessed. As a result, the quantitative ODF analysis using a numeric parameter such as r-value is appreciated under the pertained circumstance.

Bibliography

[1] Y Muraoka and H Miyaoka. Development of an all-aluminum automotive body. *J Mater Proc Technol*, 38:655–674, 1993. pages 1

[2] G S Cole and A M Sherman. Light weight materials for automotive applications. *Materials Characterization*, 35:3–9, 1995. pages

[3] G B Burger, A K Gupta, P W Jeffrey, and D J Lloyd. Microstructural control of aluminum sheet used in automotive applications. *Mater Characterization*, 35:23–39, 1995. pages

[4] W S Miller, L Zhuang, J Bottema, A J Wittebrood, P De Smet, A Haszler, and A Vieregge. Recent development in aluminium alloys for the automotive industry. *Mater Sci Eng A*, 280:37–49, 2000. pages 1

[5] J Hirsch. Aluminium alloys for automotive application. *Mater Sci Forum*, 242:33–50, 1997. pages 1, 2, 10

[6] J Hirsch. Aluminium in innovative light-weight car design. *Materials Transactions*, 52:818–824, 2011. pages

[7] J Hirsch. Automotive trends in aluminium - the european perspective. *Mater Forum*, 28:15–23, 2004. pages

[8] S Toros, F Ozturk, and I Kacar. Review of warm forming of aluminum–magnesium alloys. *J Mater Processing Technol*, 207:1 – 12, 2008. pages 1

[9] O Engler, C Schäfer, and H-J Brinkman. Crystal-plasticity simulation of the correlation of microtexture and roping in AA 6xxx Al-Mg-Si sheet alloys for automotive applications. *Acta Mater*, 60:5217–5232, 2012. pages 1, 5, 6, 8, 9, 10, 11, 12, 22, 24, 30, 42, 46, 47, 61, 70, 79, 84, 87, 92, 103

[10] D Raabe, M Sachtleber, H Weiland, G Scheele, and Z Zhao. Grain-scale micromechanics of polycrystal surfaces during plastic straining. *Acta Mater*, 51:1539–1560, 2003. pages 1, 8, 13, 61, 84, 87

[11] P S Lee, H R Piehler, B L Adams, G Jarvis, H Hampel, and A D Rollett. Influence of surface texture on orange peel in aluminum. *J Mater Proc Technol*, 80-81:315–319, 1998. pages

[12] W Tong, L G J Hector, H Weiland, and L F Wieserman. In-situ surface characterization of a binary aluminum alloy during tensile deformation. *Scripta Mater*, 36:1339 – 1344, 1997. pages 2

[13] J E Hatch. *Aluminum: Properties and Physical Metallurgy*. ASM International, 1984. pages 2, 10

[14] M Abbadi, P Hähner, and A Zeghloul. On the characteristics of Portevin-Le chatelier bands in aluminum alloy 5182 under stress-controlled and strain-controlled tensile testing. *Mater Sci Eng A*, 337:194–201, 2002. pages 2

[15] P D Wu, D J Lloyd, M Jain, K W Neale, and Y Huang. Effects of spatial grain orientation distribution and initial surface topography on sheet metal necking. *Int J Plasticity*, 23:1084 – 1104, 2007. pages 2

[16] W Tong. Strain characterization of propagative deformation bands. *J Mech Phys Solids*, 46:2087 – 2102, 1998. pages

[17] M Jain, D J Lloyd, and S R MacEwen. Hardening laws, surface roughness and biaxial tensile limit strains of sheet aluminium alloys. *Int J Mech Sci*, 38:219 – 232, 1996. pages 2

[18] R N. Wright. Anisotropic plastic flow in ferritic stainless steels and the “roping” phenomenon. *Metall Trans*, 3:83–91, 1972. pages 2, 3, 46

[19] H-J Shin, J-K An, S H Park, and D N Lee. The effect of texture on ridging of ferritic stainless steel. *Acta Mater*, 51:4693–4706, 2003. pages 2, 3, 46

[20] A K Tadros and P B Mellor. An experimental study of the in-plane stretching of sheet metal. *Int J Mech Sci*, 20:121–133, 1978. pages 2, 8

[21] D V Wilson, W T Roberts, and P M B Rodrigues. Effect of grain anisotropy on limit strains in biaxial stretching: part i. influence of sheet thickness and grain size in weakly textured sheets. *Metall Trans A*, 12:1595–1602, 1981. pages 2, 44

[22] D V Wilson, W T Roberts, and P M B Rodrigues. Effects of grain anisotropy on limit strains in biaxial stretching: part ii. sheets of cubic metals and alloys with well-developed preferred orientations. *Metall Trans A*, 12:1603–1611, 1981. pages 2, 3, 8, 87

[23] G Lefebvre, C W Sinclair, R A Lebensohn, and J-D Mithieux. Accounting for local interactions in the prediction of roping of ferritic stainless steel sheets. *Model Simul Mater Sci Eng*, 20:024008, 2012. pages 2, 3, 4, 5, 11, 12, 17, 44, 47, 84, 87

[24] P D Wu, H Jin, Y Shi, and D J Lloyd. Analysis of ridging in ferritic stainless steel sheet. *Mater Sci Eng A*, 423:300 – 305, 2006. pages 2, 5, 8, 46, 84

[25] G J Baczynski, R Guzzo, M D Ball, and D J Lloyd. Development of roping in an aluminum automotive alloy aa6111. *Acta Mater*, 48:3361–3376, 2000. pages 3, 5, 6, 7, 8, 22, 25, 26, 30, 42, 46, 51, 52, 66, 70, 79, 84, 85, 87, 103

[26] H C Chao. *Trans Am Soc Met*, 60:37, 1967. pages 2, 3

[27] H Takechi, H Kato, T Sunami, and T Nakayama. The mechanism of ridging formation in 17%-chromium stainless steel sheets. *Trans JIM*, 8:233, 1967. pages 3, 46

[28] K Bethke, M Hölscher, and K Lücke. Local orientation investigation on the ridging phenomenon in fe 17% cr steel. *Mater Sci Forum*, 157-162:1137–1144, 1994. pages

[29] M Brochu, T Yokota, and S Satoh. Analysis of grain colonies in type 430 ferritic stainless steels by electron back scattering diffraction (EBSD). *ISIJ International*, 37:872–877, 1997. pages 46

[30] O Engler, M-Y Huh, and C N Tomé. Crystal-plasticity analysis of ridging in ferritic stainless steel sheets. *Metall Mater Trans A*, 36:3127–3139, 2005. pages 2, 3, 5, 11, 22, 24, 46

[31] H C Chao. Mechanism of anisotropic lamellar fractures. *Metall Trans A*, 9:509–514, 1978. pages 3

[32] J Jiang, A Godfrey, W Liu, and Q Liu. Microtexture evolution via deformation twinning and slip during compression of magnesium alloy AZ31. *Mater Sci Eng A*, 483–484:576 – 579, 2008. pages 5

[33] O Engler and V Randle. *Introduction to Texture Analysis: Macrotexture, Microtexture, and Orientation Mapping.* CRC PressINC, 2nd edition, 2010. pages 5, 85

[34] R A Lebensohn and C N Tomé. A self-consistent anisotropic approach for the simulation of plastic deformation and texture development of polycrystals: Application to zirconium alloys. *Acta Metall Mater*, 41:2611 – 2624, 1993. pages 5

[35] C N Tomé and R A Lebensohn. *VPSC Version 7c.* Los Alamos National Laboratory, USA, 2011. pages 5

[36] C W Sinclair. Embedded grain rotation and roping of stainless steel. *Metall Mater Trans A*, 38:2435–2441, 2007. pages 5

[37] M-Y Huh and O Engler. Effect of intermediate annealing on texture, formability and ridging of 17 *Mater Sci Eng A*, 308:74 – 87, 2001. pages 5

[38] I Jung, J Mola, D Chae, and B C De Cooman. Influence of the cold rolling and annealing sequence on the ridging behaviour of ti-stabilized 18 *steel research int*, 81:1089–1096, 2010. pages

[39] J H Waxweiler. Process of diminishing of ridging in 17-chrome stainless steel, 9 1958. US Patent 2,851,384. pages 5

[40] T Tsuchiyama, R Hirota, K Fukunaga, and S Takaki. Ridging-free ferritic stainless steel produced through recrystallization of lath martensite. *ISIJ Int*, 45:923–929, 2005. pages 5

[41] S Patra and L Singhal. Influence of hot band annealing and cold rolling on texture and ridging of 430 stainless steel containing aluminum. *Mater Sci Appl*, 4:70–76, 2013. pages 5

[42] B K Jha, P Jha, and C D Singh. Process technology for the continuous hot band annealing of 17ferritic stainless steel. *J Mater Eng Performance*, 11:180–186, 2002. pages

[43] J Mola, I Jung, J Park, D Chae, and B C de Cooman. Ridging control in transformable ferritic stainless steels. *Metall Mater Trans A*, 43:228–244, 2012. pages 5

[44] O Engler and E Brünger. On the correlation of texture and ridging in AA 6016 automotive alloys. *Mater Sci Forum*, 396-402:345–350, 2002. pages 5, 6, 8, 26, 30, 46, 84, 85, 103

[45] T A Bennett, R H Petrov, and L A I Kestens. Texture-induced surface roping in an automotive aluminium sheet. *Scripta Mater*, 61:733–736, 2009. pages 5, 8, 22, 84, 85, 87

[46] N J Wittridge and R D Knutsen. A microtexture based analysis of the surface roughening behaviour of an aluminium alloy during tensile deformation. *Mater Sci Eng A*, 269:205–216, 1999. pages 5, 6, 7, 8, 10, 22, 26, 46, 70, 84, 85, 87

[47] Z Zhao, R Radovitzky, and A Cuitiño. A study of surface roughening in fcc metals using direct numerical simulation. *Acta Mater*, 52:5791 – 5804, 2004. pages 11

[48] P D Wu and D J Lloyd. Correlation of roping and texture in AA6111 automotive sheet. *Model Simul Mater Sci Eng*, 13:981–991, 2005. pages 5, 6, 8, 46, 87

[49] P D Wu, D J Lloyd, and S R MacEwen. A simple model describing roping in Al sheet. *Scripta Mater*, 48:1243 – 1248, 2003. pages 5, 11, 17, 24, 84, 88

[50] ASTM E517-00(2010). Standard Test Method for Plastic Strain Ratio r for Sheet Metal. *ASTM International, West Conshohocken, PA*, 2010. pages 5, 99

[51] ASTM E8 / E8M-13a. Standard Test Methods for Tension Testing of Metallic Materials. *ASTM International, West Conshohocken, PA*, 2013. pages

[52] ASTM B557M-14. Standard Test Methods for Tension Testing Wrought and Cast Aluminum- and Magnesium-Alloy Products (Metric). *ASTM International, West Conshohocken, PA*, 2014. pages 5, 99

[53] C Schäfer, H-J Brinkman, O Engler, and G Nitzsche. Quantification of roping in aluminium sheet alloys for car body applications by combining 3D surface measurements with Fourier analysis. *Int J of Mater Res*, 105:1 – 10, 2014. pages 6, 7, 70

[54] A Guillotin, G Guiglionda, C Maurice, and J H Driver. Correlation of Surface Roping with Through-Thickness Microtextures in an AA6xxx Sheet. *Metall Mater Trans A*, 42:1919–1924, 2011. pages 6, 7, 8, 9, 12, 26, 47, 54, 84, 85, 87

[55] C Schäfer, H-J Brinkman, O Engler, G Nitzsche, and S Keller. Methodology for Quantification of the Roping Phenomena in 6xxx Automotive Car Body Sheet Alloys. *Mater Sci Forum*, 794 - 796:45 – 50, 2014. pages 7

[56] Y S Choi, H R Piehler, and A D Rollett. Introduction and application of modified surface roughness parameters based on the topographical distributions of peaks and valleys. *Mater Characterization*, 58:901 – 908, 2007. pages 7

[57] R Prillhofer, G Rank, J Berneder, H Antrekowitsch, P J Uggowitzer, and S Pogatscher. Property criteria for automotive al-mg-si sheet alloys. *Materials*, 7:5047 – 5068, 2014. pages 7, 8, 101

[58] B Nowicki. Multiparameter representation of surface roughness. *Wear*, 102:161 – 176, 1985. pages 7

[59] M R Stoudt and J B Hubbard. Analysis of deformation-induced surface morphologies in steel sheet. *Acta Mater*, 53:4293 – 4304, 2005. pages 7

[60] Y S Choi, A D Rollett, and H R Piehler. Application of two-point orientation auto-correlation function (TP-OACF). *Mater Trans*, 47:1313–1316, 2006. pages 7

[61] A Guillotin, G Guiglionda, C Maurice, and J H Driver. Quantification of roping intensity on aluminium sheets by areal power spectral density analysis. *Mater Characterization*, 61:1119 – 1125, 2010. pages 7

[62] S Kusters, M Seefeldt, and P Van Houtte. A fourier image analysis technique to quantify the banding behavior of surface texture components in AA6xxx aluminum sheet. *Mater Sci Eng A*, 527:6239 – 6243, 2010. pages 7, 39

[63] O Engler and J Hirsch. Texture control by thermomechanical processing of AA6xxx Al-Mg-Si sheet alloys for automotive applications - a review. *Mater Sci Eng A*, 336:249 – 262, 2002. pages 8, 10, 28, 30, 84, 103

[64] P Mukhopadhyay. Alloy Designation, Processing, and Use of AA6XXX Series Aluminium Alloys. *ISRN Metall*, 2012, 2012. pages 8

[65] A K Gupta, D J Lloyd, and S A Court. Precipitation hardening in Al–Mg–Si alloys with and without excess Si. *Mater Sci Eng A*, 316:11 – 17, 2001. pages 8

[66] X Wang, J D Embury, W J Poole, S Esmaeili, and D J Lloyd. Precipitation strengthening of the aluminum alloy AA6111. *Metall Mater Trans A*, 34:2913–2924, 2003. pages

[67] C Schäfer, O R Myhr, Z Liang, H-J Brinkman, O Engler, J Hirsch, C Chang, and J Banhart. Modelling the effect of room temperature storage and deformation on the age-hardening behavior of al-mg-si alloys. In H Weiland, A D Rollett, and W A Cassada, editors, *ICAA13: 13th International Conference on Aluminum Alloys*, pages 325–330. John Wiley & Sons, Inc., 2012. pages 8

[68] T A Bennett, R H Petrov, L A I Kestens, L Z Zhuang, and P de Smet. The effect of particle-stimulated nucleation on texture banding in an aluminium alloy. *Scripta Mater*, 63:461 – 464, 2010. pages 8, 10

[69] J J Sidor, R H Petrov, and L A I Kestens. Modeling the crystallographic texture changes in aluminum alloys during recrystallization. *Acta Mater*, 59:5735 – 5748, 2011. pages 8

[70] H Jin, P D Wu, M D Ball, and D J Lloyd. Three-dimensional texture determination of 6111 aluminium alloy sheet by precise serial sectioning and EBSD measurement. *Mater Sci and Technol*, 21:419–428, 2005. pages 8, 9, 11, 15, 23, 26, 84, 85, 87

[71] P S Bate. Texture inhomogeneity and limit strains in aluminium sheet. *Scripta Metall Mater*, 27:515–520, 1992. pages 8, 10, 22

[72] P D Wu, D J Lloyd, A Bosland, H Jin, and S R MacEwen. Analysis of roping in AA6111 automotive sheet. *Acta Mater*, 51:1945 – 1957, 2003. pages 8, 11, 15, 26, 70, 84, 85, 87

[73] P D Wu and D J Lloyd. Analysis of surface roughening in AA6111 automotive sheet. *Acta Mater*, 52:1785 – 1798, 2004. pages 11, 15, 44, 61, 84, 87

[74] R Becker. Effects of strain localization on surface roughening during sheet forming. *Acta Mater*, 46:1385 – 1401, 1998. pages 8, 11, 26

[75] V Randle. Electron backscatter diffraction: Strategies for reliable data acquisition and processing. *Mater Characterization*, 60:913 – 922, 2009. pages 8, 50

[76] A J Wilkinson and T B Britton. Strains, planes, and EBSD in materials science. *Mater Today*, 15:366 – 376, 2012. pages 8, 11, 50

[77] F J Humphreys. Review grain and subgrain characterisation by electron backscatter diffraction. *J Mater Sci*, 36:3833–3854, 2001. pages

[78] D J Dingley. Progressive steps in the development of electron backscatter diffraction and orientation imaging microscopy. *J Microsc*, 213:214–224, 2004. pages

[79] D J Dingley and V Randle. Microtexture determination by electron back-scatter diffraction. *J Mater Sci*, 27:4545–4566, 1992. pages

[80] R A Schwarzer. Automated crystal lattice orientation mapping using a computer-controlled SEM. *Micron*, 28:249 – 265, 1997. pages

[81] S Zaefferer. On the formation mechanisms, spatial resolution and intensity of backscatter kikuchi patterns. *Ultramicroscopy*, 107:254 – 266, 2007. pages

[82] A J Wilkinson and P B Hirsch. Electron diffraction based techniques in scanning electron microscopy of bulk materials. *Micron*, 28:279 – 308, 1997. pages

[83] R A Schwarzer. Advances in crystal orientation mapping with the SEM and TEM. *Ultramicroscopy*, 67:19 – 24, 1997. pages

[84] B L Adams, S I W, and K Kunze. Orientation imaging: The emergence of a new microscopy. *Metall Trans A*, 24:819–831, 1993. pages

[85] S I Wright. A review of automated orientation imaging microscopy(oim). *J Comput Assist Microsc (USA)*, 5:207–221, 1993. pages

[86] J R Michael and R P Goehner. Crystallographic phase identification in the scanning electron microscope: Backscattered electron Kikuchi patterns. In *Presented at the Annual Meeting of the Electron Microscopy Society of America, Cincinnati, OH, 1-6 Aug. 1993*, pages 1–6, 1993. pages

[87] M N Alam, M Blackman, and D W Pashley. High-angle kikuchi patterns. *Proc R Soc Lond A: Math Phys Eng Sci*, 221:224–242, 1954. pages 8

[88] T A. Bennett, J Sidor, R H. Petrov, and L A I Kestens. Roping Phenomena in Aluminium Alloy 6016: A Microtextural Investigation. *Mater Sci Forum*, 638-642:396–400, 2010. pages 8, 10, 26, 30, 85

[89] A W F Smith, S A Court, and F J Humphreys. Recrystallization and texture of aluminium-magnesium-silicon-(copper) alloys. In G Gottstein and D A Molodov, editors, *Proc First Joint Int Conf Recrystallization and Grain Growth*, pages 1323–1328. Springer, 2001. pages 8, 26, 84, 85, 87

[90] A C Lewis, J F Bingert, D J Rowenhorst, A Gupta, A B Geltmacher, and G Spanos. Two- and three-dimensional microstructural characterization of a super-austenitic stainless steel. *Mater Sci Eng A*, 418:11 – 18, 2006. pages 8

[91] M Uchic, M Groeber, M Shah, A Shiveley, and J Spowart. A novel multi-modal 3d characterization system to quantify grain-level microstructural features in macro-scale volumes. *Microsc Microanal*, 17:988–989, 2011. pages 50

[92] H Pirgazi, S Ghodrat, and L A I Kestens. Three-dimensional EBSD characterization of thermo-mechanical fatigue crack morphology in compacted graphite iron. *Mater Characterization*, 90:13 – 20, 2014. pages 11, 15, 50

[93] S Zaefferer, S I Wright, and D Raabe. Three-dimensional orientation microscopy in a focused ion beam-scanning electron microscope: A new dimension of microstructure characterization. *Metall Mater Trans A: Phys Metall and Mater Sci*, 39:374–389, 2008. pages

[94] N Zaafarani, D Raabe, R N Singh, F Roters, and S Zaefferer. Three-dimensional investigation of the texture and microstructure below a nanoindent in a cu single crystal using 3D EBSD and crystal plasticity finite element simulations. *Acta Mater*, 54:1863–1876, 2006. pages

[95] M A Groeber, B K Haley, M D Uchic, D M Dimiduk, and S Ghosh. 3d reconstruction and characterization of polycrystalline microstructures using a FIB–SEM system. *Mater Characterization*, 57:259 – 273, 2006. pages 8, 11

[96] A J Beaudoin, J D Bryant, and D A Korzekwa. Analysis of ridging in aluminum auto body sheet metal. *Metall Mater Trans A*, 29:2323–2332, 1998. pages 9, 11, 84, 87

[97] J Sidor, R H Petrov, and L Kestens. 3.17 - texture control in aluminum sheets by conventional and asymmetric rolling. In B Yilbas, S Hashmi, G F Batalha, and C J Van Tyne, editors, *Comprehensive Materials Processing*, pages 447 – 498. Elsevier, Oxford, 2014. pages 10

[98] V A Romanova, R R Balokhonov, and S Schmauder. Numerical study of mesoscale surface roughening in aluminum polycrystals under tension. *Mater Sci Eng A*, 564:255 – 263, 2013. pages 11

[99] L Qin, M Seefeldt, and P Van Houtte. Analysis of roping of aluminum sheet materials based on the meso-scale moving window approach. *Acta Mater*, 84:215 – 228, 2015. pages 12, 47, 51, 84, 85, 87

[100] W Xu, M Ferry, N Mateescu, J M Cairney, and F J Humphreys. Techniques for generating 3-d EBSD microstructures by FIB tomography. *Mater Characterization*, 58:961 – 967, 2007. pages 15

[101] B J Inkson, M Mulvihill, and G Möbus. 3d determination of grain shape in a feal-based nanocomposite by 3d FIB tomography. *Scripta Mater*, 45:753 – 758, 2001. pages 15

[102] P Van Houtte. *The "MTM-FHM" software system.* MTM, KU Leuven, 2004. pages 19, 85, 103

[103] S I Wright and B L Adams. An Evaluation of the Single Orientation Method for Texture Determination in Materials of Moderate Texture Strength. *Textures and Microstructures*, 12:65–76, 1990. pages 19, 31

[104] H J Bunge. *Texture analysis in materials science: mathematical methods, PR Morris Trans.* Butterworths London, 1982. pages 20, 85, 103

[105] P Van Houtte. A method for the generation of various ghost correction algorithms - the example of the positivity method and the exponential method. *Texture, Stress, and Microstructure*, 13:199–212, 1990. pages 20

[106] C Lamb and M Zecchino. *WYKO surface profiler technical reference manual*, 1999. pages 21, 32

[107] H J Bunge. Some applications of the Taylor theory of polycrystal plasticity. *Kristall und Technik*, 5:145–175, 1970. pages 21, 22, 88, 99

[108] W F Hosford and W A Backofen. Strength and plasticity of textured metals. In W A Backofen, editor, *Fundamentals of Deformation Processing*, pages 259–292, Syracuse, NY, USA, 1964. Syracuse University Press. pages 21, 22, 99

[109] Q Xie, P Eyckens, H Vegter, J Moerman, A Van Bael, and P Van Houtte. Polycrystal plasticity models based on crystallographic and morphologic texture: Evaluation of predictions of plastic anisotropy and deformation texture. *Mater Sci Eng A*, 581:66–72, 2013. pages 22, 78

[110] L Qin, M Seefeldt, T A. Bennett, R H. Petrov, and P Van Houtte. Mesoscopic ebsd analysis and mesomechanical behavior of ridging or roping in aa6xxx alloys. *Mater Sci Forum*, 702-703:955–958, 2011. pages 22, 85

[111] P Jepson and R Bailey. A new method for quantification of texture uniformity of plate. In A D Rollett, editor, *Applications of Texture Analysis*, pages 135–146. John Wiley & Sons, Inc., 2008. pages 22

[112] P S Lee, H R Piehler, A D Rollett, and B L Adams. Texture clustering and long-range disorientation representation methods: application to 6022 aluminum sheet. *Metall Mater Trans A*, 33:3709–3718, 2002. pages

[113] B L Adams, P S Lee, and A D Rollett. Meso-scale modelling on ridging or roping of aluminium alloys. In J. Szpunar, editor, *Proceedings of the 12th International Conference on Textures of Materials (ICOTOM12)*, pages 724–729, Ottawa, Canada, 1999. NRC Research Press. pages 22

[114] L Qin, M Seefeldt, and P Van Houtte. Meso-scale modelling on ridging or roping of aluminium alloys. In M Isac, F Chiesa, and R Guthrie, editors, *Materials Science and Technology 2013*, pages 1247–1283, Montreal, Quebec, Canada, 2013. pages 22

[115] D J Whitehouse. *Surfaces and their Measurement*. Butterworth-Heinemann, 2002. pages 24, 54

[116] F Bachmann, R Hielscher, and H Schaeben. Texture analysis with mtex–free and open source software toolbox. In H Klein and R A Schwarzer, editors, *Texture and Anisotropy of Polycrystals III*, volume 160, pages 63 – 68. Trans Tech Publ, 2010. pages 26, 90

[117] W Mao. Influence of rolling reductions on recrystallization texture in commercially pure al. *J. Mater Sci Technol*, 6:257 – 262, 1990. pages 28

[118] R D Doherty. Recrystallization and texture. *Prog Mater Sci*, 42:39 – 58, 1997. pages 28

[119] O Engler. On the influence of orientation pinning on growth selection of recrystallisation. *Acta Mater*, 46:1555 – 1568, 1998. pages 28

[120] T A Bennett, J Sidor, R H Petrov, and L A I Kestens. The effect of intermediate annealing on texture banding in aluminum alloy 6016. *Adv Eng Mater*, 12:1018–1023, 2010. pages 30, 83, 103

[121] F Wagner, S Matthies, and O Van Landuyt. Processing Individual Orientation Data to Calculate ODFs. *Mater Sci Forum*, 273-275:89–98, 1998. pages 31

[122] P Stoica and R L Moses. *Spectral analysis of signals, first ed.* Pearson Prentice Hall, 2005. pages 32

[123] A V Oppenheim, R W Schafer, and J R Buck. *Discrete-time Signal Processing, second ed.* Prentice Hall, Inc., Upper Saddle River, NJ, USA, 1999. pages 32, 44

[124] S W Smith. *The Scientist and Engineer's Guide to Digital Signal Processing, first ed.* California Technical Publishing, San Diego, CA, USA, 1997. pages 44

[125] T T Soong. *Fundamentals of Probability and Statistics for Engineers.* Wiley, 2004. pages 55, 87, 88

[126] R E Walpole, R H Myers, S L Myers, and K Ye. *Probability & statistics for engineers and scientists.* Prentice Hall, 9th edition, 2011. pages 55, 87, 88

[127] M-T Puth, M Neuhäuser, and G D Ruxton. Effective use of pearson's product–moment correlation coefficient. *Animal Behaviour*, 93:183 – 189, 2014. pages 55, 87

[128] H Inoue, T Yamasaki, P Van Houtte G Gottstein, and T Takasugi. Recrystallization texture and r-value of rolled and t4-treated al-mg-si alloy sheets. *Mater Sci Forum*, 495 - 497:573 – 578, 2005. pages 78

[129] C-G Oertel, I Huensche, W Skrotzki, W Knabl, A Lorich, and J Resch. Plastic anisotropy of straight and cross rolled molybdenum sheets. *Mater Sci Eng A*, 483–484:79 – 83, 2008. pages

[130] C Klinkenberg, H Klein, and J Gerlach. Texture development during mechanical r-value determination. *Mater Sci Forum*, 495 - 497:1493 – 1498, 2005. pages

[131] J-J Park. Predictions of texture and plastic anisotropy developed by mechanical deformation in aluminum sheet. *J Mater Proc Technol*, 87:146 – 153, 1999. pages 78, 99

[132] H J Shin and D N Lee. Plastic strain ratios of fe and ni electrodeposits. *Mater Sci Forum*, 408 - 412:1115 – 1120, 2002. pages 78

[133] O Engler. Control of texture and earing in aluminium alloy AA3105 sheet for packaging applications. *Mater Sci Eng A*, 538:69 – 80, 2012. pages 83

[134] H Inoue and T Takasugi. Texture control for improving deep drawability in rolled and annealed aluminum alloy sheets. *Mater Trans*, 48:2014–2022, 2007. pages 83

[135] H-R Wenk and P Van Houtte. Texture and anisotropy. *Reports on Progress in Physics*, 67:1367, 2004. pages 84

[136] H Utsunomiya, T Ueno, and T Sakai. Improvement in the r-value of aluminum sheets by differential-friction rolling. *Scripta Mater*, 57:1109 – 1112, 2007. pages 84, 99

[137] O Engler and J Hirsch. Recrystallization textures and plastic anisotropy in Al-Mg-Si sheet alloys. *Mater Sci Forum*, 217 - 222:479 – 486, 1996. pages 84

[138] J Sidor, R H Petrov, and L A I Kestens. Deformation, recrystallization and plastic anisotropy of asymmetrically rolled aluminum sheets. *Mater Sci Eng A*, 528:413 – 424, 2010. pages 84

[139] J Sidor, A Miroux, R Petrov, and L Kestens. Microstructural and crystallographic aspects of conventional and asymmetric rolling processes. *Acta Mater*, 56:2495 – 2507, 2008. pages 84

[140] H Jin and D J Lloyd. Roping in 6111 aluminum alloys with various iron contents. *Mater Sci and Eng A*, 403:112 – 119, 2005. pages 84, 87

[141] H Jin and A K Gupta. The Effect of through-Thickness Texture Inhomogeneity on Roping Behavior in AA6111 Al-Si-Mg Alloy. *Mater Sci Forum*, 702 - 703:273 – 278, 2012. pages 84

[142] W C Liu, C-S Man, and J G Morris. Lattice rotation of the cube orientation to the β fiber during cold rolling of AA5052 aluminum alloy. *Scripta Mater*, 45:807 – 814, 2001. pages 85

[143] J Hirsch and K Lücke. Overview no. 76: Mechanism of deformation and development of rolling textures in polycrystalline f.c.c. metals—ii. simulation and interpretation of experiments on the basis of taylor-type theories. *Acta Metall*, 36:2883 – 2904, 1988. pages

[144] D Juul Jensen, N Hansen, and F J Humphreys. Texture development during recrystallization of aluminium containing large particles. *Acta Metall*, 33:2155 – 2162, 1985. pages

[145] J Hirsch, E Nes, and K Lücke. Rolling and recrystallization textures in directionally solidified aluminium. *Acta Metall*, 35:427 – 438, 1987. pages 85

[146] R Davies and V Randle. Secondary processing of electron backscatter data from an aluminum alloy. *Mater Characterization*, 37:131–141, 1996. pages 85

[147] R Pearce. *Sheet Metal Forming*. Adam Hilger series on new manufacturing processes and materials. Springer Science & Business Media, 1991. pages 99

[148] F Barlat. Crystallographic texture, anisotropic yield surfaces and forming limits of sheet metals. *Mater Sci Eng*, 91:55 – 72, 1987. pages 99

[149] P Van Houtte. Treatment of elastic and plastic anisotropy of polycrystalline materials with texture. *Mater Sci Forum*, 273 - 275:67 – 76, 1998. pages

[150] Y C Liu and L K Johnson. Hill's plastic strain ratio of sheet metals. *Metall Trans A*, 16:1531–1535, 1985. pages

[151] C-S Man. On the r-value of textured sheet metals. *Int J Plasticity*, 18:1683 – 1706, 2002. pages

[152] S-H Choi, J-K Choi, H-W Kim, and S-B Kang. Effect of reduction ratio on annealing texture and r-value directionality for a cold-rolled al–5%mg alloy. *Mater Sci Eng A*, 519:77 – 87, 2009. pages

[153] W Hammami, L Delannay, A Habraken, and L Duchêne. Crystal plasticity prediction of lankford coefficients using the multisite model: influence of the critical resolved shear stresses. *Int J Mater Form*, 2:65–68, 2009. pages 99

[154] W G Granzow. Sheet formability of steels, properties and selection: Irons, steels, and high-performance alloys. In *ASM Handbook online*, volume 1, pages 573 – 580, 1990. pages 101

[155] P Van Houtte. On the representation of texture functions of cubic metals in euler space. *Textures and Microstructures*, 7:187 – 205, 1987. pages 103

[156] S Matthies, H-R Wenk, and G W Vinel. Some basic concepts of texture analysis and comparison of three methods to calculate orientation distributions from pole figures. *J Appl Cryst*, 21:285 – 304, 1988. pages 103

[157] O Engler, C N Tomé, and M-Y Huh. A study of through-thickness texture gradients in rolled sheets. *Metall Mater Trans A*, 31:2299 – 2315, 2000. pages 111

[158] J Liu, S W Banovic, F S Biancaniello, and R D Jiggetts. Through-thickness texture gradient in an annealed al-mg alloy sheet. *Metall Mater Trans A*, 36:869 – 874, 2005. pages 111

[159] K Decroos, J Sidor, and M Seefeldt. A new analytical approach for the velocity field in rolling processes and its application in through-thickness texture prediction. *Metall Mater Trans A*, 45:948 – 961, 2014. pages

[160] F Barlat, J C Brem, and J Liu. On crystallographic texture gradient and its mechanical consequence in rolled aluminum-lithium sheet. *Scripta Metall Mater*, 27:1121 – 1126, 1992. pages

[161] M Ghosh, A Miroux, and L A I Kestens. Correlating r-value and through thickness texture in al–mg–si alloy sheets. *J Alloys Compd*, 619:585 – 591, 2015. pages

[162] M T Pérez-Prado, M C Cristina, M Torralba, O A Ruano, and G Gónzalez-Doncel. Texture gradient evolution in al-5deformation at high superplastic strain rate. *Scripta Mater*, 35:1455 – 1460, 1996. pages 111

Curriculum vitae

Name	Ling Qin
Date of birth	July 26, 1984
Place of birth	Baotou, Neimongol, China

Education

2010 – 2015	PhD in Engineering Science Dept. Materials Engineering KU Leuven, Belgium
2007 – 2009	Master in Advanced Engineering Materials Dept. Materials and Manufacturing Technology Chalmers University of Technology, Sweden
2003 – 2007	Bachelor in Metallic Materials Engineering Dept. Power and Mechanical Engineering Wuhan University, China

Work Experience

2009	R&D researcher in Materials center AB Sandvik Materials Technology SE-811 81 Sandviken, Sweden

List of Publications

Peer reviewed journals

Qin, L., Seefeldt, M., Van Houtte, P. (2015). Analysis of roping of aluminum sheet materials based on the meso-scale moving window approach. Acta Materialia, 84, 215-228.

Gong, X., Marmy, P., Qin, L., Verlinden, B., Wevers, M., Seefeldt, M. (2014). Effect of liquid metal embrittlement on low cycle fatigue properties and fatigue crack propagation behavior of a modified 9Cr-1Mo ferritic-martensitic steel in an oxygen-controlled lead-bismuth eutectic environment at 350°C. Materials Science and Engineering A, Structural Materials: Properties, Microstructure and Processing, 618, 406-415.

Peer reviewed conference proceedings

Qin, L., Van Houtte, P., Seefeldt, M. (2015), On the correlation of meso-scale local texture and roping profile in AA6xxx sheet alloys, IOP Conf. Ser.: Mater. Sci. Eng. 82 012094. ICOTOM 17, International Conference on Textures of Materials. Dresden, Germany, 24-29 August 2014. IOPscience.

Qin, L., Van Houtte, P., Seefeldt, M. (2013). Meso-scale modelling on ridging or roping of aluminium alloys. In Isac, M. (Ed.), Chiesa, F. (Ed.), Guthrie, R. (Ed.), Laroche, F. (Ed.), Gallienne, D. (Ed.), Bouchard, D. (Ed.), Marin, G. (Ed.), Fafard, M. (Ed.), Sediako, D. (Ed.), Ravindran, R. (Ed.), Pekguleryuz, M. (Ed.), Chen, X. (Ed.), Sumanth, S. (Ed.), Materials Science and Technology (MS&T) 2013. Montreal, Quebec, Canada, 27-31 October 2013 (pp. 1274-1283).

Qin, L., Seefeldt, M., Bennet, T., Petrov, R., Van Houtte, P. (2012). Mesoscopic EBSD analysis and mesomechanical behavior of ridging or roping in AA6XXX alloys. Materials Science Forum: Vol. 702-703. ICOTOM 16, International Conference on Textures of Materials. Mumbai, India, 12-17 December 2011 (pp. 955-958). Switzerland: Trans Tech Publications.

FACULTY OF ENGINEERING SCIENCE
DEPARTMENT OF MATERIALS ENGINEERING
STRUCTURAL COMPOSITES AND ALLOYS, INTEGRITY AND NONDESTRUCTIVE TESTING
Kasteelpark Arenberg 44 bus 2450
B-3001 Heverlee
ling.qin@mtm.kuleuven.be
http://www.mtm.kuleuven.be/English/